

Review

# Recent Advances on the Rational Design of Non-Precious Metal Oxide Catalysts Exemplified by $\text{CuO}_x/\text{CeO}_2$ Binary System: Implications of Size, Shape and Electronic Effects on Intrinsic Reactivity and Metal-Support Interactions

Michalis Konsolakis \*  and Maria Lykaki

Industrial, Energy and Environmental Systems Lab (IEESL), School of Production Engineering and Management, Technical University of Crete, GR-73100 Chania, Greece; mlykaki@isc.tuc.gr

\* Correspondence: mkonsol@pem.tuc.gr; Tel.: +30-28210-37682

Received: 11 December 2019; Accepted: 22 January 2020; Published: 1 February 2020



**Abstract:** Catalysis is an indispensable part of our society, massively involved in numerous energy and environmental applications. Although, noble metals (NMs)-based catalysts are routinely employed in catalysis, their limited resources and high cost hinder the widespread practical application. In this regard, the development of NMs-free metal oxides (MOs) with improved catalytic activity, selectivity and durability is currently one of the main research pillars in the area of heterogeneous catalysis. The present review, involving our recent efforts in the field, aims to provide the latest advances—mainly in the last 10 years—on the rational design of MOs, i.e., the general optimization framework followed to fine-tune non-precious metal oxide sites and their surrounding environment by means of appropriate synthetic and promotional/modification routes, exemplified by  $\text{CuO}_x/\text{CeO}_2$  binary system. The fine-tuning of size, shape and electronic/chemical state (e.g., through advanced synthetic routes, special pretreatment protocols, alkali promotion, chemical/structural modification by reduced graphene oxide (rGO)) can exert a profound influence not only to the reactivity of metal sites in its own right, but also to metal-support interfacial activity, offering highly active and stable materials for real-life energy and environmental applications. The main implications of size-, shape- and electronic/chemical-adjustment on the catalytic performance of  $\text{CuO}_x/\text{CeO}_2$  binary system during some of the most relevant applications in heterogeneous catalysis, such as CO oxidation,  $\text{N}_2\text{O}$  decomposition, preferential oxidation of CO (CO-PROX), water gas shift reaction (WGSR), and  $\text{CO}_2$  hydrogenation to value-added products, are thoroughly discussed. It is clearly revealed that the rational design and tailoring of NMs-free metal oxides can lead to extremely active composites, with comparable or even superior reactivity than that of NMs-based catalysts. The obtained conclusions could provide rationales and design principles towards the development of cost-effective, highly active NMs-free MOs, paving also the way for the decrease of noble metals content in NMs-based catalysts.

**Keywords:** copper-ceria; rational design; size; shape; electronic/chemical functionalization; CO oxidation;  $\text{N}_2\text{O}$  decomposition; preferential oxidation of CO (CO-PROX); water gas shift reaction (WGSR);  $\text{CO}_2$  hydrogenation

## 1. Introduction

The fast growth rate of population in the last decades has led to an unprecedented increase in energy demands. However, the main energy sources fulfilling global demands originate from fossil fuels, rising significant concerns in relation to sources availability and environmental degradation. To this

end, the development of emerging energy technologies towards the production of environmentally friendly fuels besides the establishment of cost-effective environmental technologies for climate change mitigation has become a main priority in the scientific and industrial community. Clean and reliable energy supply in conjunction with environmental protection by means of highly- and cost-effective technologies is one of the most significant concerns of the 21st century [1–4].

In view of the above aspects, heterogeneous catalysis is expected to have a key role in the near future towards sustainable development. Heterogeneous catalysis has received considerable attention from both the scientific and industrial community, as it is a field of diverse applications, including the petrochemical industry with the production of high quality chemicals and fuels, the fields of energy conversion and storage, as well as the remediation of the environment through the abatement of hazardous substances, signifying its pivotal role in the world economy [1,3,5–7].

Several types of catalysts have been employed for energy and environmental applications, which can be generally classified into: Noble metal (NMs)-based catalysts and NMs-free metal oxides (MOs), such as bare oxides, mixed metal oxides (MMOs), perovskites, zeolites, hexaaluminates, hydrotalcites, spinels, among others. Among these, NMs-based catalysts have been traditionally used in numerous processes, such as CO oxidation [8–11], nitrous oxide (N<sub>2</sub>O) decomposition [12–17], water-gas shift reaction [18–20], carbon dioxide (CO<sub>2</sub>) hydrogenation [21–25], etc., exhibiting high activity and selectivity. However, their scarcity and extremely high cost render mandatory the development of highly active, stable and selective catalysts that will be of low cost, nonetheless [26,27].

On the other hand, metal oxides (MOs) prepared from earth-abundant, and inexpensive transition metals have attracted considerable attention as alternatives to rare and expensive NMs, due to their particular features, such as enhanced redox properties, thermal stability and catalytic performance in conjunction to their lower cost [2,3,5,28–43]. The latter is clearly manifested in Figure 1, which schematically depicts the cost of noble metals in comparison with copper (a typical transition metal massively involved in MOs) for the past five-year period. It is evident that the price of noble metals is larger than that of copper by about four orders of magnitude.

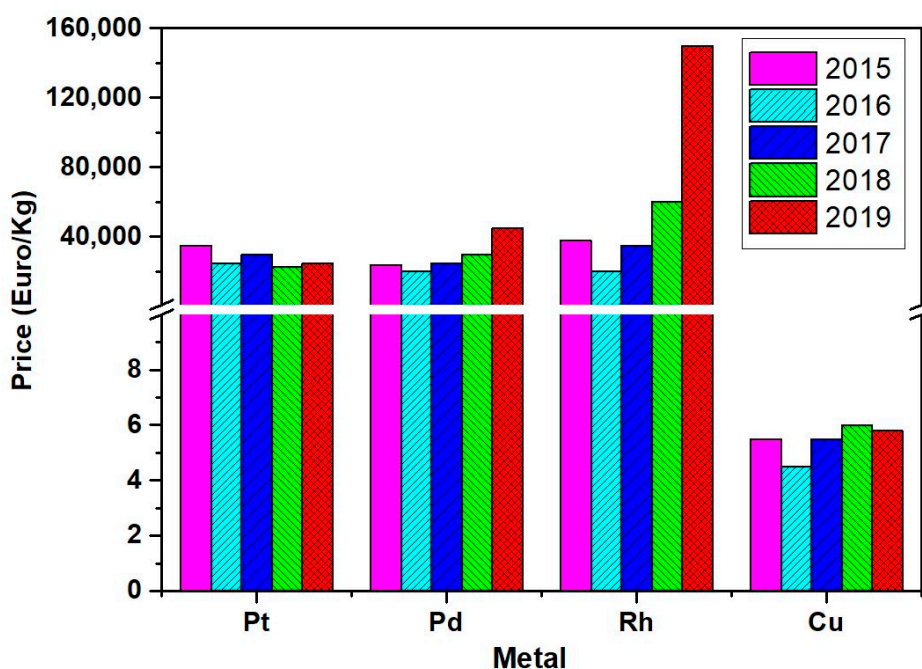


**Figure 1.** Relative comparison of noble metal and copper metal prices over the past five-year period. Data taken from <https://www.infomine.com>.

Mixed metal oxides (MMOs) appropriately prepared by admixing two or more single metal oxides in a specific proportion, have lately gained particular attention, since they exhibit unique

structural and surface properties, which are completely different from that of parent oxides. Amongst the numerous MOs, transition metal-based oxides have attracted particular attention, due to their peculiar chemisorption capacity, linked to partially filled d-shells [44,45]. For instance, Cu-based oxides can catalyze a variety of reactions following a redox-type mechanism (e.g., photocatalysis), due to the wide range of Cu oxidation states (mainly Cu<sup>0</sup>, Cu<sup>I</sup>, Cu<sup>II</sup>), which enables reactivity in multi-electron pathways. On the other hand, reducible oxides, such as ceria, not only provide the basis of active phase dispersion, but could have a profound influence on the intrinsic catalytic activity, through metal-support interactions, as will be further discussed in the sequence. In particular, ceria or cerium oxide (CeO<sub>2</sub>) has attracted considerable attention, due to its unique properties, including enhanced thermal stability, high oxygen storage capacity (OSC) and oxygen mobility, as well as superior reducibility driven by the formation of surface/structural defects (e.g., oxygen vacancies) through the rapid interplay between the two oxidation states of cerium (Ce<sup>3+</sup>/Ce<sup>4+</sup>) [2,6,38,46–48]. Besides bare ceria's exceptional properties, its combination with transition metals leads to improved catalytic performance, due to the synergy between the metal phase and the support, related to electronic, geometric and bifunctional interactions [40,49–54]. In this regard, the combination of CuO<sub>x</sub> and CeO<sub>2</sub> oxides towards the formation of CuO<sub>x</sub>/CeO<sub>2</sub> binary oxides, offers catalytic activities comparable or even better to NMs-based catalysts in various applications, such as CO oxidation, N<sub>2</sub>O decomposition, preferential oxidation of CO (CO-PROX), as lately reviewed [40].

The peculiar reactivity of CuO<sub>x</sub>/CeO<sub>2</sub> system arises not only from the distinct characteristics of individual CuO<sub>x</sub> and CeO<sub>2</sub> phases, but mainly from their synergistic interactions. More specifically, the synergistic effects between the different counterparts of MOs can offer unique characteristics (e.g., improved reducibility, abundant structural defects, etc.), reflected then on the catalytic activity [40,55–60]. Various interrelated factors are usually considered under the term “synergy”, involving among others:

- (i) The superior interfacial reactivity as compared to the reactivity of individual particles;
- (ii) The presence of defects (e.g., oxygen vacancies);
- (iii) The enhanced reducibility of MOs as compared to single ones;
- (iv) The interplay between interfacial redox pairs (e.g., Cu<sup>2+</sup>/Cu<sup>+</sup> and Ce<sup>3+</sup>/Ce<sup>4+</sup>).

In view of the above, very recently, the modulation of metal-support interactions as a tool to enhance the catalytic performance was thoroughly reviewed, disclosing that up to fifteen-fold productivity enhancement can be achieved in reactions related to C1 chemistry by controlling metal-support interactions [61]. However, it is well established today—thanks to the rapid development of sophisticated characterization techniques—that various interrelated factors, such as the composition, the size, the shape, and the electronic state of MOs different counterparts can exert a profound influence on the local surface chemistry and metal-support interactions, and in turn, on the catalytic activity of these multifunctional materials [6,48,51,52,62–74]. In view of this fact, the fine-tuning of MOs towards the development of catalytic materials with the desired cost, activity, selectivity and stability could be considered the “Holy Grail” in the field of catalyst manufacturing. Size, shape, porous, redox and electronic adjustment by means of appropriate synthetic and promotional/modification routes can provide the vehicle to substantially modify not only the reactivity of metal sites in its own right, but also the interfacial activity, offering highly active and stable materials for real-life energy and environmental applications (Figure 2).

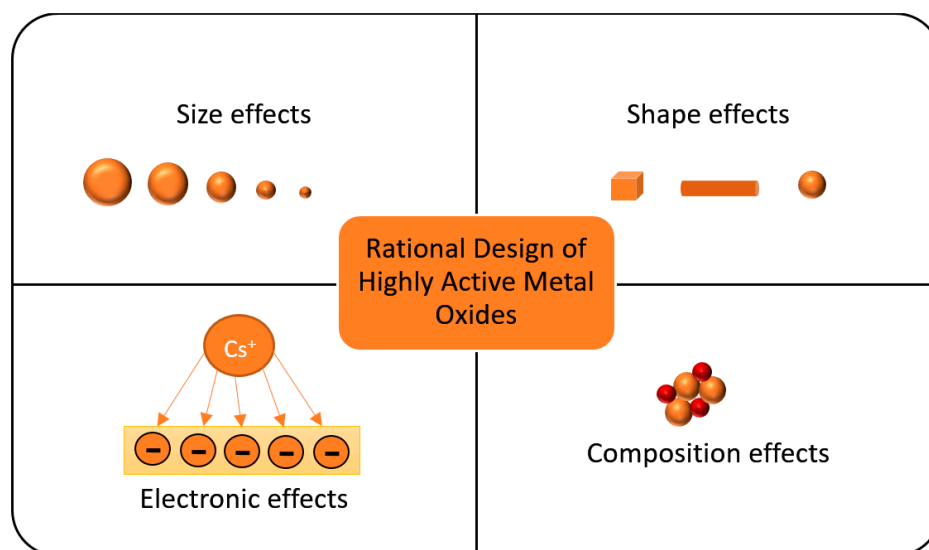


**Figure 2.** Schematic illustration of metal oxides (MOs) fine-tuning by adjusting their size, shape, composition and electronic/chemical state.

In light of the aforementioned issues, the present review article aims to gain insight into the particular effect of each adjusted parameter on MOs physicochemical characteristics and in turn, on their catalytic performance, towards revealing rigorous structure-property relationships. The basic principles of MOs fine-tuning by modulating the size, shape and electronic/chemical state by means of appropriate synthetic/modification routes will be initially presented. The implications of size, shape and electronic/chemical effects in catalysis will be next exemplified on the basis of state-of-the-art catalytic applications of  $\text{CuO}_x/\text{CeO}_2$  binary oxide, involving CO oxidation,  $\text{N}_2\text{O}$  decomposition, preferential oxidation of CO (CO-PROX), water gas shift reaction (WGSR), and  $\text{CO}_2$  hydrogenation to value-added chemicals/fuels. It should be noted here that the scope of the present article is not to provide a complete survey in relation to the fundamental understanding and practical applications of  $\text{CuO}_x/\text{CeO}_2$  system, which can be found in various comprehensive reviews [40,49,75–77]. Herein, the  $\text{CuO}_x/\text{CeO}_2$  system is used as an excellent benchmark to reveal how we can adjust the local surface chemistry and in turn, the catalytic activity of MOs. The obtained conclusions can provide rationales and design principles towards the development of cost-effective, highly active NMs-free MOs of various compositions, paving also the way for the decrease of noble metals content in NMs-based catalysts. The term “ $\text{CuO}_x$ ” instead of CuO is used throughout the text to denote the differentiation of Cu oxidation state depending on synthesis procedure and reaction environment, as discussed in the sequence.

## 2. Fine-Tuning of Metal Oxides (MOs)

Heterogeneous catalysis traditionally refers to a chemical reaction on the surface of a solid catalyst, involving adsorption and activation of reactant(s) on specific active sites, chemical transformation of adsorbed species and products desorption. Thanks to the rapid development of both in situ and ex situ characterization techniques, it is well acknowledged that the elementary reaction steps are strongly dependent on several parameters involving the size, the shape, the electronic state of individual particles, as well as on their interfacial interactions. Hence, the macroscopic catalytic behavior can be considered as the outcome of interactions between reactants, intermediates and products with the micro(nano)scopic coordination environment of surface atoms, involving geometric arrangements, electronic confinement, and interfacial effects, among others. In view of this fact, the modulation of the above-mentioned parameters can profoundly affect the local surface structure and chemistry with great implications in catalysis. It should be mentioned, however, that due to the interplay between structural and chemical factors, it is quite challenging to disclose the fundamental origin of catalytic performance.

Thus, it is of vital importance to establish reliable structure-property relationships, unveiling the particular role of each factor. The latter could lead to rational design instead of trial-and-error methods by utilizing the fundamental knowledge at the nanoscale.

Moreover, taking into account that the majority of MOs consists of at least two different counterparts, this triggers unique opportunities towards designing various MOs of the same composition, but of different reactivity by adjusting the above-mentioned parameters either in one or both counterparts. For instance, by modulating the size, morphology and electronic/chemical state of ceria carrier in  $\text{CuO}_x/\text{CeO}_2$  composites, a different extent of metal-support interactions can be attained with implications in catalysis. In a similar manner, the co-adjustment of the shape of both  $\text{CuO}_x$  and  $\text{CeO}_2$  could lead to different synergistic interactions, providing  $\text{CuO}_x/\text{CeO}_2$  systems of peculiar reactivity. The proposed adjusting approach on the way to fine-tune MOs is schematically illustrated in Figure 3, clearly revealing the unique opportunities in the field of materials synthesis and engineering towards the development of low-cost and highly-effective composites.

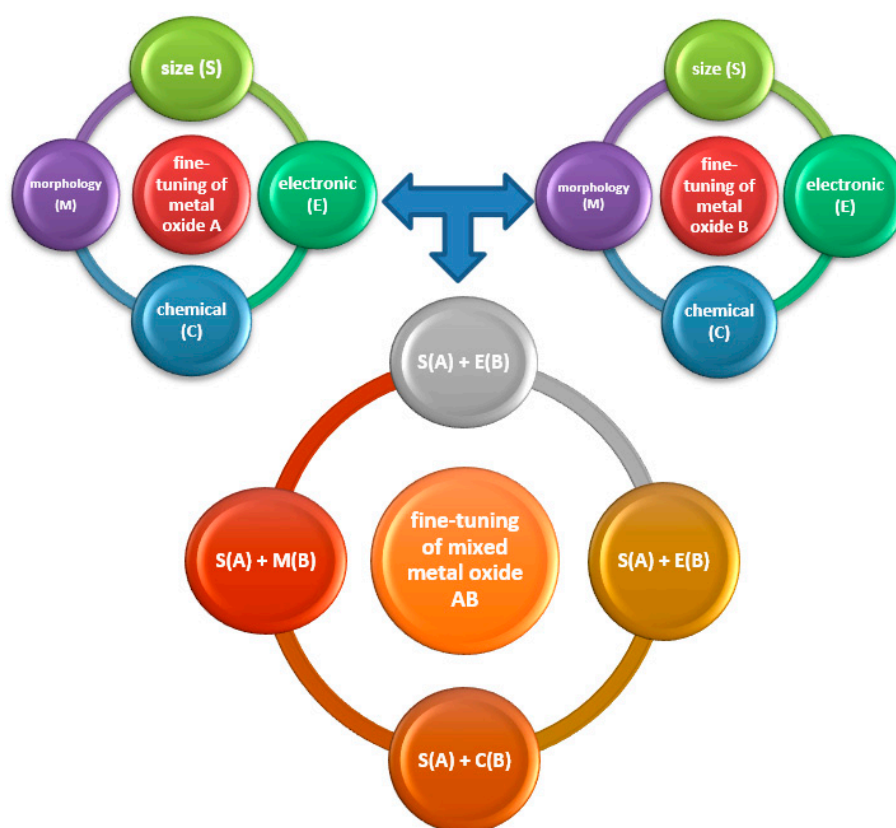


**Figure 3.** Indicative pathways towards the fine-tuning of a binary metal oxide of the general formula AB by adjusting the size (S), morphology (M), electronic (E) and chemical (C) state of one or both of the individual counterparts A and B. For instance,  $\text{CuO}_x$  (A)/ $\text{CeO}_2$  (B) binary oxides of different reactivity can be obtained by combining the morphology engineering of  $\text{CeO}_2$  {denoted as M (B)} with the size engineering of  $\text{CuO}_x$  {denoted as S (A)} or by combining both the size and morphology engineering of both counterparts {S(A) + M(A) + S(B) + M (B)}. The scheme is just indicative of the different approaches that can be followed to adjust the local surface chemistry of MOs, without exhausting the margins of all possible combinations.

In the following, the basic principles of size, shape, and electronic/chemical effects are provided in separate sections. It should be stressed, however, that this distinct presentation does not also mean a distinct effect of each factor in catalysis. Almost all parameters are interrelated; thus, the discrete role of each one in the catalytic activity of MOs cannot be easily disclosed, as further discussed below.

## 2.1. Size Effects

The rapid development of nanotechnology in the last years enables the fabrication of MOs with tunable size and shape at the nanometer scale. Nowadays, it has been both experimentally and theoretically revealed that the surface, structural and electronic properties of nanoparticles (NPs) differ essentially from the corresponding bulk properties. In general, by decreasing the particle size of metal oxide particles down to few nanometers (e.g., <10 nm), a dramatic increase in activity can be generally obtained, attributed to “size effects”. This size-dependent reactivity can be ascribed to different contributions, namely: (i) Quantum size effects, (ii) presence of low coordinated atoms into NPs surface, (iii) electronic state of the surface, (iv) strong interparticle interactions. Hereinafter, the particular effect of every contribution is shortly presented for the sake of following discussions in relation to the fine-tuning of MOs. For additional reading, several comprehensive articles in this topical area are recommended [40,52,62,66,70,71,74,78].

In particular, by decreasing the size of a material down to nanometer scale, the surface-to-volume ratio is largely increased, resulting in an increased population of surface sites, being the active sites in catalysis. Besides the modulation of the fraction of atoms on the topmost surface layer, the number of atoms at corners and edges, being considered more active than those at planes, is considerably increased by decreasing the size. More specifically, size decrease leads to a high density of under-coordinated atoms with exceptional adsorption and catalytic properties [52,62,70,79–83]. Typically, surface sites with low coordination number (CN) demonstrate stronger adsorption ability as compared to those of high CN [66,70,84]; linear relationships between the adsorption energy of various adsorbates and the coordination number have been found for several transition metals, including among others non-precious metals, such as Cu, Ni, and Co [85,86]. Thus, from the geometrical point of view, size decrease has a direct effect on both the number and type of active surface sites reflected then on catalytic activity.

Aside from the “geometric size effects”, the electronic state of surface atoms can undergo substantial modifications upon decreasing the particle size down to nanometer scale. In particular, when a bulk material with a continuous electron band is subjected to size decrease down to the nanoscale, the so-called quantum effect or confinement effect is taking place, arising from the presence of discrete electronic states as in the case of molecules [62,70,74,78,87]. For instance, it has been reported that a higher electron density, with a d band close to the Fermi level, can be obtained for Au NPs smaller than ca. 2 nm as compared to bigger ones, with great implications in CO oxidation [88–91].

Recently, thanks to the introduction of new generation sophisticated characterization techniques (e.g., high-angle annular dark-field scanning transmission electron microscopy (HAADF-STEM), extended X-ray absorption fine structure (EXAFS)) and computational methods (e.g., DFT calculations), an indirect size effect linked to the metal-support interactions is clearly revealed. More specifically, even small perturbations between metal nanoparticles and oxide carriers, due to charge transfer between particles, local electric fields, morphological changes, “ligand” effect, etc., can induce a substantial modification in catalytic activity [40,50,55,92–95]. To more accurately describe these phenomena, the term Electronic Metal Support Interactions (EMSI) has recently been proposed by Campbell [96] in contrast to classical Strong Metal Support Interactions (SMSI). In view of this concept, tiny metal clusters composed of a few or even single atoms could play a dominant role in catalysis, despite the fact that they do not account for more than a few percent of the total metal content [40,50]. In view of this fact, it has been shown that by controlling metal (Ni, Pd, Pt) nanocrystal size, the length of metal-ceria interface is appropriately adjusted with significant implications in CO oxidation; normalized reaction rates were dramatically increased with decreasing the size, due to the increased boundary length (Figure 4).

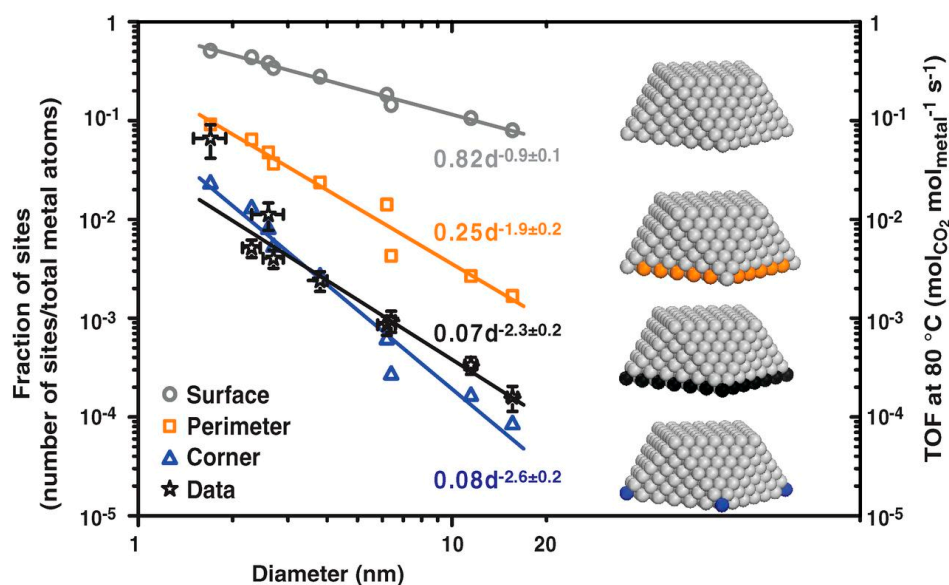


**Figure 4.** The calculated number of sites with a particular geometry (surface and perimeter or corner atoms in contact with the support) as a function of diameter and the turnover frequency (TOF) at 80 °C for ceria-based metals (Ni, Pd, Pt). Reproduced with permission from Reference [52]. Copyright© 2013, American Association for the Advancement of Science (AAAS).

As an additional implication of size-dependent behavior, the significant effect of particle size on structural defects of reducible carriers (such as ceria) should be mentioned. In fact, a close relationship between the crystal size of ceria and the concentration of oxygen vacancies has been revealed; the large surface-to-volume ratio in conjunction to the exposure of under-coordinated sites can facilitate the formation of oxygen vacancies and the  $\text{Ce}^{3+}$  fraction in non-stoichiometric  $\text{CeO}_{2-\delta}$  NPs [71,97–103]. Moreover, an inverse correlation between the lattice parameters of  $\text{CeO}_2$  NPs and particle sizes has been established (Figure 5a), attributed to the increase of  $\text{Ce}^{3+}$  and oxygen vacancies concentration [71]. A similar trend was recorded between the surface-to-bulk oxygen ratio and particle size (Figure 5b).

Closing this part concerning the size effects, it should be noted, that although particle size decrease has, in general, a positive catalytic effect, there is a variation in relation to size-activity relationships depending on catalyst type and reaction environment. For instance, a positive size effect could be obtained if the rate determining step (rds) involves the bond cleavage of a reactant molecule on surface atoms with low coordination number. However, if the same under-coordinated atoms strongly bind dissociated species (e.g., oxygen atoms), this could lead to the poisoning of catalyst surface, and thus, to the negative size effect. In particular, in reactions with no structure sensitivity, the activity remains unaffected by changes in the particle size, while it could decrease with decreasing particle size, referred as negative particle size effect or antipathetic structure sensitivity, or increase as the particle size decreases, referred as positive particle size effect or sympathetic structure sensitivity [79]. Moreover, the activity may reach a maximum when small particles exhibit a negative effect, and larger particles show a positive one [79].

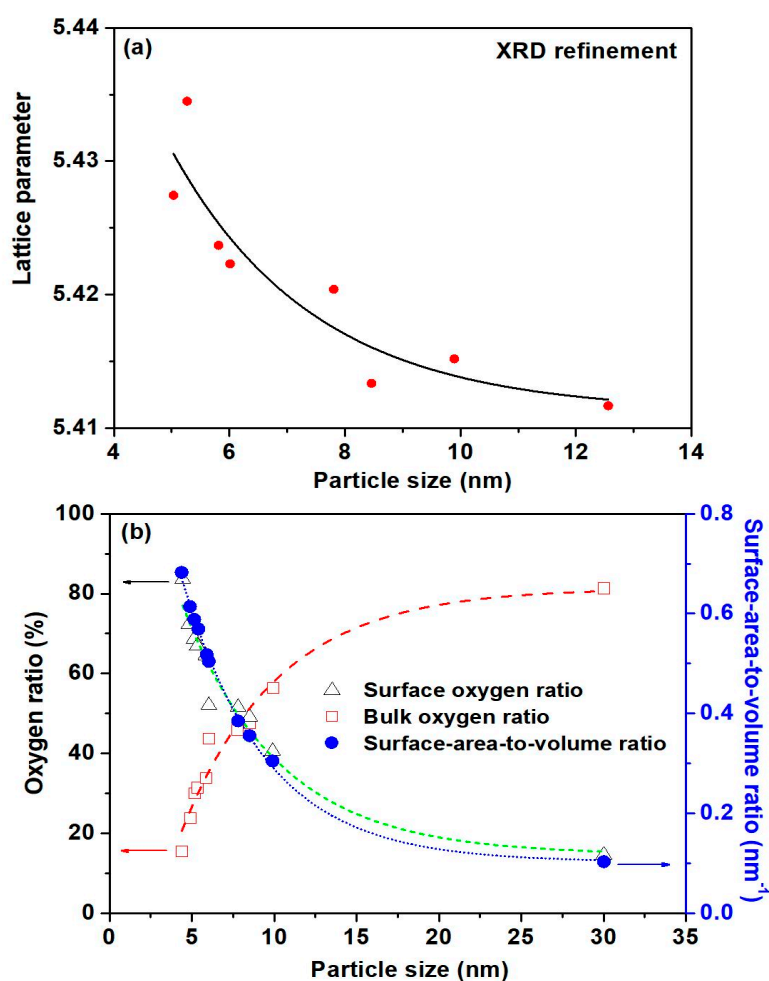


**Figure 5.** (a) Lattice expansion of ceria as a function of size and (b) the inverse relationship of surface oxygen to bulk oxygen (TPR) and the correlation of surface oxygen ratio with the theoretical surface to volume ratio. Adapted from Reference [71]. Copyright© 2010, Royal Society of Chemistry.

## 2.2. Shape Effects

Nanostructured catalysts possess unique properties originating from nanoscale phenomena linked mainly to size effects, commented above, and shape effects. The latter refers to the modification of catalytic activity through the preferential exposure of specific crystallographic facets on the reaction environment, also termed as morphology-dependent nanocatalysis [51,65,66,70,82,104–106]. In particular, the catalytic cycle and hence the reaction efficiency, is determined on reactants adsorption/activation and products desorption processes, being strongly influenced by the surface planes of catalysts particles. In this regard, the simultaneous modulation of size and shape at the nanometer scale can determine the number and the nature of exposed sites, and thus, the catalytic performance. This particular topic is an essential issue within the field of nanocatalysis, aiming to the control of a specific chemical reaction through co-adjusting these parameters at the nanometer scale.

Thanks to the latest advances in materials science, nanostructured catalysts with well-defined crystal facets can be fabricated by precisely controlling nanocrystals nucleation and growth rate [48,63,66,67,78,105]. The obtained crystal morphology is the result of several synthesis parameters, involving temperature, pressure, concentration, and pH, among others. Several reviews have been devoted to the subject [6,38,67,82,97,105,107,108]. Various structures with similar or different dimensions in all directions, such as nanospheres, nanocubes, nanowires, nanorods, nanosheets, etc., could be obtained.

The shape control of ceria and its implications in catalysis is most probably the most extensively investigated system among metal oxides in heterogeneous catalysis [2,6,38,48,51,64,65,73,82,97,104,107,109–112]. The growth rate mechanism of ceria nanocrystals can be affected by various parameters, such as the basicity or polarity of the solvent [113,114], the aging temperature [115,116], the precursor compound [117,118], and the impregnation medium [119]. Regulation of nanocrystals nucleation and growth processes results in specific shapes, such as rods and cubes [48,67]. Moreover, by altering the physicochemical conditions during the synthesis procedure (e.g., by the usage of a capping agent), blocking of certain facets or continuous growth of others may occur.

There are several synthetic approaches for the preparation of ceria nanoparticles, including precipitation [119–121], thermal decomposition [121,122], template or surfactant-assisted method [123–126], microwave-assisted synthesis [127–129], the alcohothermal [124,130] or hydrothermal [121,124,131–135] method, microemulsion [133,136,137], solution combustion [138,139], sol-gel [140–142], sonochemical [143,144], etc. However, not all methods lead to particles of well-ordered size and shape with uniform dispersion on the catalyst surface [145]. Among the different methods, the hydrothermal one has attracted considerable attention, due to the simplicity of the precursor compounds used, the short reaction time, the homogeneity in morphology, as well as the acquisition of various nanostructures, such as rods, polyhedra, cubes, wires [107,117,121,124,131,134,135,146–159]. Ceria nanocrystals have three low-index lattice facets of different activity and stability, namely, {100}, {110}, {111} [48,106], as shown in Figure 6.

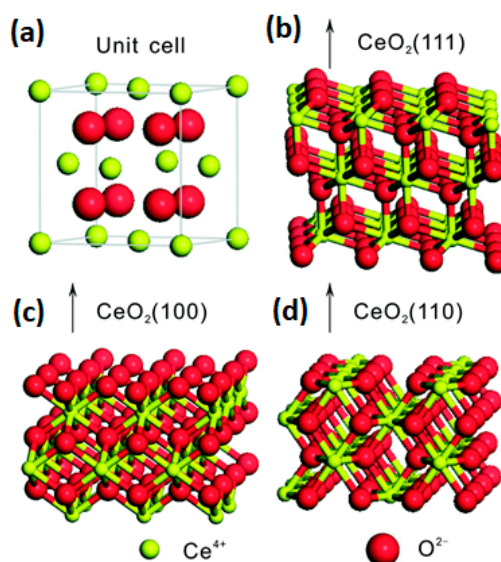


**Figure 6.** Structural models of  $\text{CeO}_2$  (a) unit cell, (b) (111), (c) (100), and (d) (110) surfaces without structural optimizations. Reproduced with permission from Reference [106]. Copyright© 2014, Royal Society of Chemistry.

The selective exposure of ceria reactive facets can strongly affect the redox properties of ceria and in turn, its intrinsic characteristics as an active phase or supporting carrier. Popular ceria shapes, mainly, involve nanorods (NR), nanocubes (NC) and nanopolyhedra (NP). Ceria nanorods, mostly, expose the {110} and {100} facets, whereas, nanocubes and nanopolyhedra preferentially expose the {100} and {111} facets, respectively [48,51,106]. By means of both experimental [82,104,109,146,160,161] and theoretical [112,162–166] studies, it was shown that the energy formation of anionic vacancies is dependent on the exposed facets, following the order: {111} > {100} > {110}. In this regard, the reactivity of ceria NR is, in general, increased upon increasing the fraction of {110} and {100} facets [65].

In view of the above, it has been clearly revealed that the activity and selectivity are strongly affected by the exposed crystal planes. For instance, the formation rate of ammonia on Fe crystals follows the sequence: {111} >> {100} > {110} [167]. Similar morphology-dependent effects have been demonstrated for several noble metal [105,168] and metal oxide [51] catalyzed processes.

Very recently, we showed that among ceria nanoparticles of different morphology (nanocubes, nanorods and nanopolyhedra), as shown in Figure 7a, ceria nanorods with {100} and {110} crystal planes, exhibited the optimum redox properties in terms of loosely bound oxygen species population [115,121]. Figure 7b depicts the H<sub>2</sub> temperature-programmed reduction (H<sub>2</sub>-TPR) profiles of ceria nanocubes, nanopolyhedra and nanorods, where two main peaks at ca. 550 and 800 °C can be identified, ascribed to the reduction of surface (O<sub>s</sub>) and bulk (O<sub>b</sub>) oxygen, respectively. Notably, the surface-to-bulk (O<sub>s</sub>/O<sub>b</sub>) ratio is strongly dependent on ceria morphology following the order: NC (0.71) < NP (0.94) < NR (1.13). It is also worth mentioning that the onset reduction temperature follows the reverse order, i.e.,: NC (589 °C) > NP (555 °C) > NR (545 °C), implying the lower temperature reduction of {110} and {100} surfaces as compared to {111}.

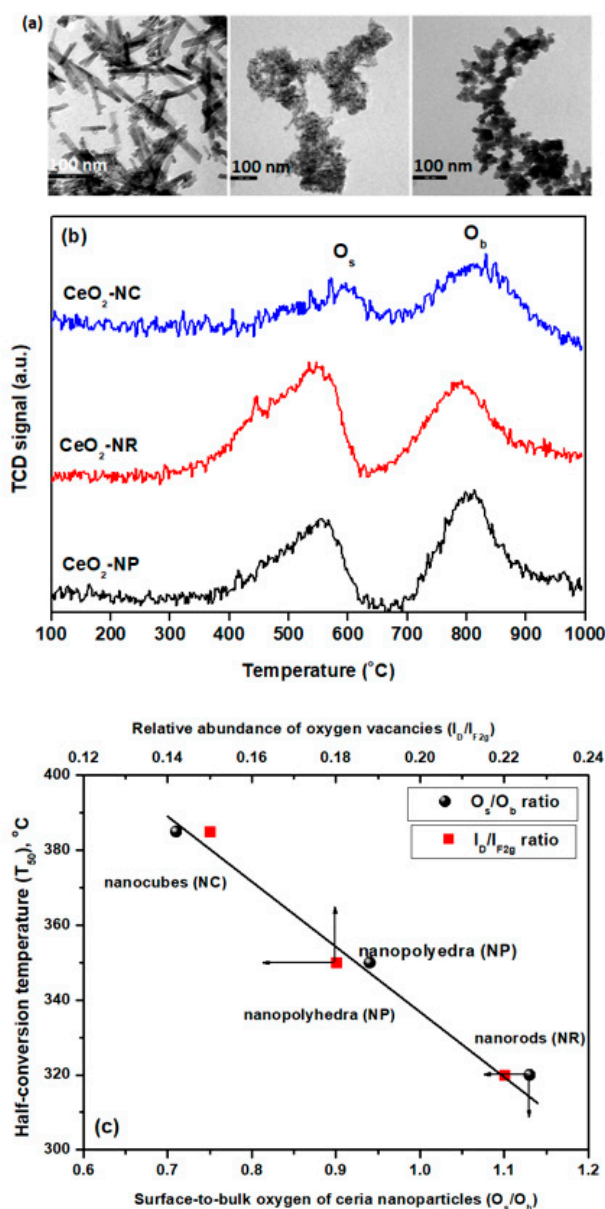


**Figure 7.** (a) TEM images and (b) H<sub>2</sub>-TPR profiles for ceria nanoparticles of different morphology, i.e., nanorods, nanopolyhedra and nanocubes; (c) CO oxidation performance (T<sub>50</sub>) of ceria nanoparticles as a function of ceria redox properties expressed in terms of surface-to-bulk (O<sub>s</sub>/O<sub>b</sub>) TPR ratio and I<sub>D</sub>/I<sub>F2g</sub> Raman ratio [115].

More recently, we explored the impact of ceria exposed facets on structural defects by means of in situ Raman spectroscopy following a novel approach involving sequential spectra acquisition under alternating oxidizing and reducing atmospheres [115]. The in situ Raman measurements perfectly corroborated the aforementioned arguments in relation to the impact of crystal planes on the reducibility; the relative abundance of defects and oxygen vacancies exhibited by the  $I_D/I_{F2g}$  ratio, as well as the relative reducibility expressed by the detachment of O atoms and the partial  $Ce^{4+} \rightarrow Ce^{3+}$  reduction, follow the same trend, i.e., NR > NP > NC.

These results unambiguously indicate that  $CeO_2$ -nanorods exhibit the highest concentration of weakly bound oxygen species, linked to enhanced reducibility and oxygen mobility. Interestingly, an almost linear relationship is revealed between the redox properties, expressed either as  $O_s/O_b$  or  $I_D/I_{F2g}$  ratio, and the CO oxidation performance, in terms of half-conversion temperature ( $T_{50}$ ), of ceria nanoparticles (Figure 7c), clearly demonstrating the implications of shape modulation in catalysis.

### 2.3. Electronic Effects

Besides modulating the local surface structure of MOs by size and shape effects, described above, the fine-tuning of electronic structure by appropriate promoters can be considered as an additional modulating tool. Promoters hold a key role in heterogeneous catalysis towards optimizing the catalytic activity, selectivity and stability by modifying the physicochemical features of MOs, and can be classified into two general categories: Structural promoters and electronic promoters. The first category mainly involves the doping of supporting carrier to enhance its structural characteristics and in turn, the stabilization of active phase (e.g., incorporation of rare earth dopants into three-way catalysts [5]). On the other hand, electronic promoters can modify catalysts surface chemistry either directly or indirectly. The former mainly includes the electrostatic interactions between the reactant molecules and the local electric field of promoters. The latter denotes the promoter-induced modifications on metal Fermi level, which is then reflected on the chemisorptive bond strength of reactants and intermediates with great consequences in catalysis. In particular, “promoter effect” is related to the changes in the work function ( $\Phi$ ) of the catalysts surface upon promoter addition, accompanied by substantial modification of its chemisorption properties. The vast majority of electronic promotion over metal oxide catalysts refers to alkali modifiers. It has been well documented that alkali addition can drastically enhance the activity and selectivity of numerous catalytic systems, involving among others Pt-, Pd-, Rh-, Cu-, Fe-based catalysts, in various energy and environmental related reactions (e.g., [169–174]). Various comprehensive studies have been devoted to the role of promoters in heterogeneous catalysis, to which the reader can refer for further reading [175–177].

Figures 8 and 9 depict the “promoter effect” in the case of alkali-doped  $Co_3O_4$  oxides during the  $N_2O$  decomposition [178,179]. A close relationship between the catalytic performance (in terms of half-conversion temperature,  $T_{50}$ ) and the work function ( $\Phi$ ) was disclosed revealing the electronic nature of alkali promotion; electropositive modifiers (such as alkalis) can decrease the work function of the catalyst surface, thus, activating the adsorption/decomposition of electron-acceptor molecules (such as  $N_2O$ ) [178]. However, at high alkali coverages, depolarization occurs, due to the strengthening of the alkali-alkali bond at the expense of the alkali-surface bond, resulting in a work function increase [180].

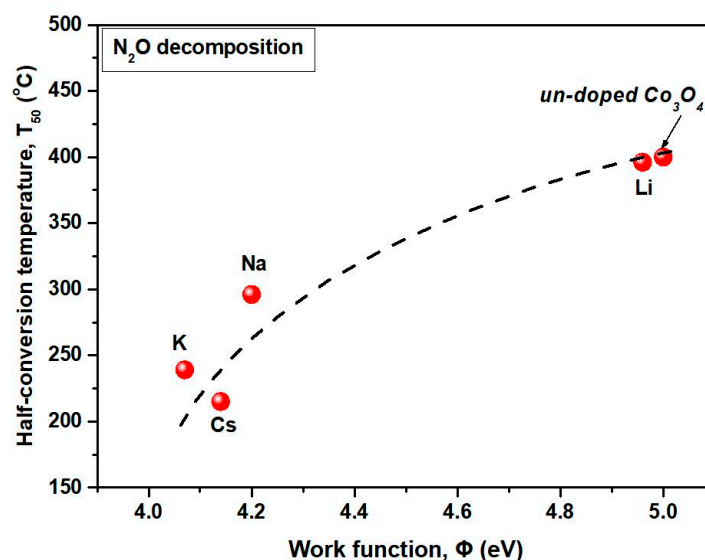


**Figure 8.** Correlation of half-conversion temperature ( $T_{50}$ ) with the work function of alkali promoted  $\text{Co}_3\text{O}_4$ . Reaction conditions: 5.0%  $\text{N}_2\text{O}$ ;  $m_{\text{cat}} = 300$  mg; GHSV =  $7000$   $\text{h}^{-1}$ ; alkali coverage =  $\sim 2$   $\text{at}/\text{nm}^2$ . Adapted from Reference [178]. Copyright© 2009, Elsevier.

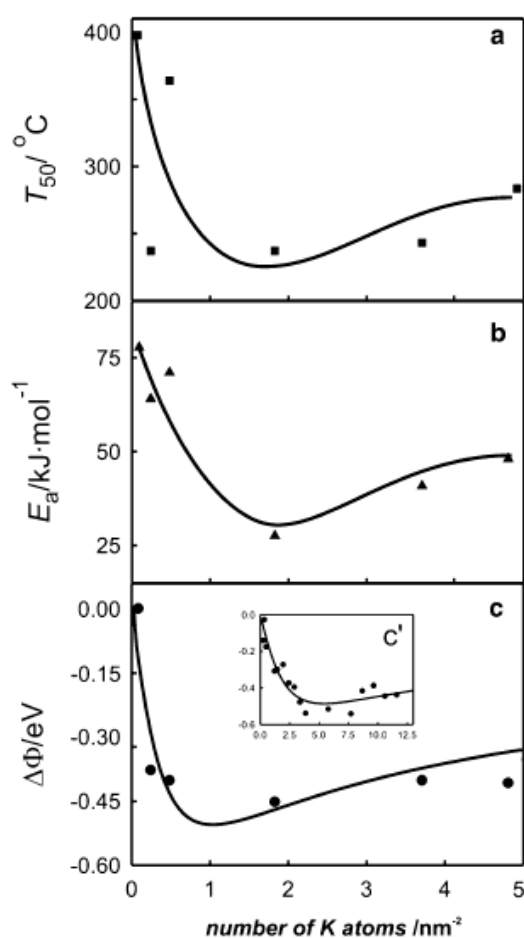


**Figure 9.** (a) The half-conversion temperature of  $\text{N}_2\text{O}$  ( $T_{50}$ ), (b) apparent activation energy ( $E_a$ ) and (c) work function changes ( $\Delta\Phi$ ) as a function of potassium loading ( $\Theta_K$ ) introduced from  $\text{K}_2\text{CO}_3$  and (c insert) KOH precursor. Reproduced with permission from Reference [179]. Copyright© 2008, Springer Nature.

In this point, it should be mentioned that, depending on the support nature and crystal planes, alkali adsorption may lead to surface reconstruction. This surface reconstruction can be explained by taking into account the structural/electronic perturbations induced by the formation of the alkali-surface bond [181]. As mentioned previously, the crystallographic orientation of the support plays an important role in the diffusion rate of the adsorbed species, as well as in their in-between interaction, resulting in different structural stabilization [181]. For instance, potassium promoter was shown to stabilize certain iron facets in K-promoted iron catalysts, by inducing changes in the crystal growth rate, thus, enabling the formation of small particles with abundance in active facets and affecting the activity and selectivity of the overall system [182]. As shown in Figure 10, by increasing the K/Fe surface atomic ratio, the crystal facets become more stable and the surface energy is decreased [182]. This clearly manifests the pivotal role of alkali addition towards co-adjusting the structural and electronic properties of the catalyst surface, and in turn, the catalytic performance.

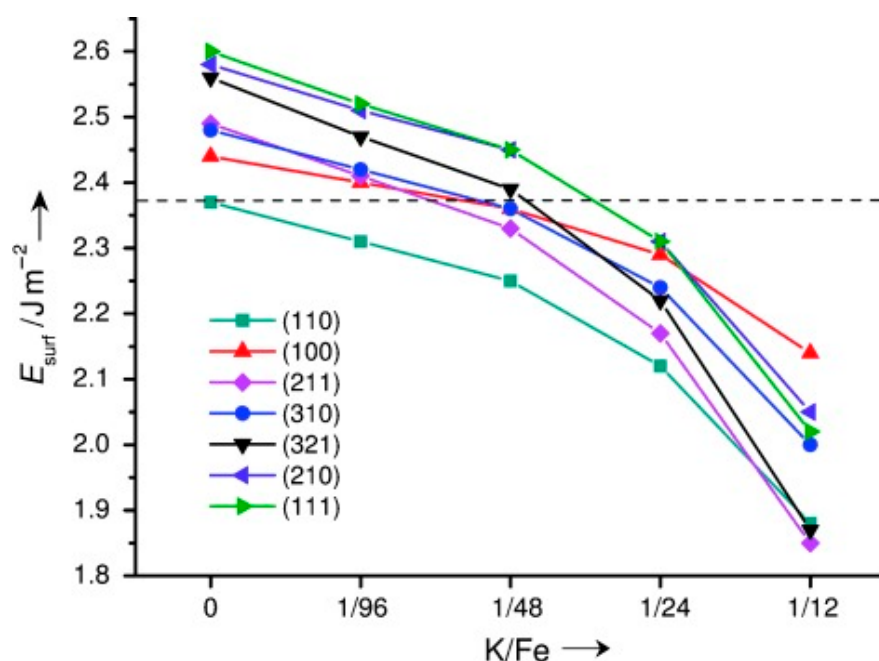


**Figure 10.** Surface energy variation versus the surface atomic ratio of K to Fe. Reproduced with permission from Reference [182]. Copyright© 2011, John Wiley and Sons.

Besides the alkali-induced modifications on the chemisorption properties, significant alterations on the surface oxygen mobility have been demonstrated; alkali addition could facilitate suprafacial recombination of oxygen towards molecular oxygen desorption, thus, liberating active sites [40]. Both the electronic and redox modifications induced by alkali addition can exert remarkable effects on catalytic activity and selectivity, demonstrating the key role of “promoter effect” as an additional adjusting parameter in catalysis.

It should be noted here, as mentioned in the case of size and shape effects, that the promoter effect is not always positive. The latter strongly depends on reactants type (electron donor or electron acceptor adsorbates) and the work function changes (increase or decrease) induced by the promoter (electropositive or electronegative). Thus, besides the structure-sensitivity, commented above, the electronic-sensitivity of a given reaction should always be taken into account, when attempting to co-adjust the size, shape and electronic state. Although, this is not an easy task, it could be an effective approach towards designing cost-effective and highly active composites, as revealed in the sequence.

#### 2.4. Chemical Modifiers

Besides the extensive use of alkalis or alkaline earths as promoters, numerous other chemical substances can be employed to modulate the local surface chemistry/structure and in turn, the activity, selectivity and long-term stability of parent catalyst (e.g., [74]). In this regard, metal alloys (e.g., Au-Ni alloys as reforming catalysts [183], Pt-Sn alloys for ethanol oxidation [184]) are extensively employed in catalysis towards obtaining highly active and cost-effective catalytic formulations. Several mechanisms are considered responsible for the enhanced performance of bimetallic systems, involving mainly structural (strain effects) and electronic (charge-transfer effects) modifications that can be induced by the interaction between the different counterparts. The latter substantially modifies the binding energy of adsorbates and the path of chemical reactions with major consequences in catalysis [50,74].

In a similar manner, chemical substances with unique physico-chemical properties, such as carbon-based materials, have lately received considerable attention as chemical modifiers or supporting carriers [62,185]. Various carbon materials, such as carbon nanotubes (CNTs), reduced graphene oxide (rGO), ordered mesoporous carbon (OMC), carbon nanofibers (CNFs), and graphitic carbon nitride (g-C<sub>3</sub>N<sub>4</sub>), have received particular attention in catalysis after the significant progress in controlled synthesis and the fundamental understanding of their properties. In general, nanocarbons (NCs) possess unique physical (large surface area, specific morphology, appropriate pore structure) and chemical (electronic structure, surface acidity/basicity) properties arising from their nanoscale confined structures [185].

The combination of metal nanoparticles (NPs) with carbon materials by means of various synthetic approaches can exert significant modifications on the structural and electronic surrounding of NPs with subsequent implications in catalysis [62,185]. As for example, confined Fe NPs in CNTs exhibit an almost twice yield to C<sub>5+</sub> hydrocarbons as compared to Fe particles during the syngas conversion to liquid hydrocarbons [186]. The latter was mainly ascribed to the modified structural and redox properties of confined Fe NPs within CNTs [62]. Moreover, the application of graphene in catalysis allows the fabrication of multifunctional materials with distinct heterostructures, which offer quite different properties as compared to individual materials [185,187,188]. In general, carbon materials with exceptional structural and electronic characteristics can be effectively employed either as supporting materials or chemical modifiers, offering unique opportunities towards modulating the intrinsic reactivity of MOs. For instance, it has been found that the homogeneous distribution of copper atoms on the surface of rGO in combination with the outstanding electronic properties of rGO lead to high electrocatalytic activity, due to the synergy between the two components [189].

Metal-organic frameworks (MOFs) are another type of supporting carriers/chemical modifiers consisting of inorganic metal ions or clusters that are bridged with organic ligands in order for one or more dimensional configurations to be formed [190]. These materials exhibit unique properties, such as high surface area and porosity, while their complex network consisting of various channels allows passage in small molecules [191]. The fabrication of MOF-based MOs composites is of great interest, as it results in the development of materials with tunable properties and functionality. Metal nanoparticles regarded as the active centers can be stabilized by MOFs through confinement effects [192]. As for example, Cu, Ni, and Pd nanoparticles encapsulated by MOFs exhibited high catalytic efficiency, ascribed mainly to the synergistic effects of nanoconfinement and electron-donation offered by MOF framework [193–198]. Furthermore, by changing the MOFs functional groups, products distribution may differ, as a consequence of variations induced in the chemical environment of the catalytically active sites [199].

#### 2.5. Pretreatment Effects

Besides the advances that can be induced by adjusting the size, shape and electronic state of MOs, special pretreatment protocols or activation procedures could be applied to further adjust the local surface chemistry of MOs (e.g., [200,201]). In particular, the local surface chemistry of the MOs can be further tailored by appropriate pretreatment protocols, including thermal or chemical

pretreatment. According to the pretreatment protocol followed, different properties get affected, resulting in diversified catalytic behavior. By way of illustration, it has been reported that defect engineering by a low-pressure thermal process instead of atmospheric pressure activation, could notably increase the concentration of oxygen vacancy defects and in turn, the CO oxidation activity of ceria nanoparticles, offering an additional tool towards the fine-tuning of MOs [200]. Moreover, it has been documented that the pretreatment protocol (oxidation or reduction) induces significant effects on the local surface structure of cobalt-ceria oxides affecting the dehydroxylation process in ammonia synthesis [202]. In a similar manner, oxidative pretreatment of cobalt-ceria catalysts resulted in an impoverishment of catalyst surface in cobalt species, due to the preferential existence of cerium species on the outer surface, whereas, cobalt and cerium species are uniformly distributed on the catalyst surface through the reduction pretreatment, which gives rise to the formation of oxygen vacancies [33]. In addition, a strong interaction between gold and ceria has been observed after O<sub>2</sub> pretreatment, due to the electron transfer from Au<sup>0</sup> to ceria, giving rise to oxygen vacancy formation, lattice oxygen migration, as well as to the formation of Au<sup>δ+</sup>-CO and surface bicarbonate species, favoring, thus, the adsorption of CO and the desorption of CO<sub>2</sub> [203]. In terms of T<sub>100</sub>, CO oxidation performance showed the following order: O<sub>2</sub> pretreatment (74 °C) < N<sub>2</sub> pretreatment (142 °C) < 10% CO/Ar pretreatment (169 °C) [203]. In view of the above short discussion, the pretreatment conditions can affect the facilitation with which certain active species are formed on the catalyst surface, the oxygen mobility or the formation of oxygen defects, with great implications in the catalytic performance.

### 3. Implications of MOs Fine-Tuning in Catalysis Exemplified by CuO<sub>x</sub>/CeO<sub>2</sub> Binary System

In this section, the implications of metal oxides fine-tuning by means of the above-described size, shape and electronic/chemical effects are presented, on the basis of the CuO<sub>x</sub>/CeO<sub>2</sub> binary oxide system. This particular catalytic system is selected as representative MOs, taking into account the tremendous fundamental and practical attention lately devoted to the copper-containing cerium oxide materials. More specifically, the abundant availability of copper and ceria and consequently, their lower cost (about four orders of magnitude, Figure 1) render CuO<sub>x</sub>/CeO<sub>2</sub> composites strongly competitive. Moreover, their excellent reactivity—linked to peculiar metal-support interactions—in conjunction to their remarkable resistance to various substances, such as carbon dioxide, water and sulfur is of particular fundamental and practical importance [57,76,204]. Remarkably, copper-containing ceria catalysts appropriately adjusted by the aforementioned routes demonstrated catalytic activity similar or even better than NMs-based catalysts in various applications, such as CO oxidation, the decomposition of N<sub>2</sub>O and the water-gas shift reaction, among others [115,124,159,205–216].

For instance, the inverse CeO<sub>x</sub>/Cu(111) system exhibits superior CO oxidation performance at a relatively low-temperature range (50–100 °C), in which the noble metals do not function well, exhibiting activity values of about one order of magnitude higher than those measured on Pt(100), Pt(111), and Rh(111) [217–219]. The latter has been mainly attributed, on the basis of the most conceptual experimental and theoretical studies, to the existence of Ce<sup>3+</sup> at the metal-oxide interface which binds O atoms weaker as compared to bulk Ce<sup>3+</sup> [217,220].

In light of the above aspects, in this section, the main implications of size, shape and electronic/chemical effects on the catalytic performance of CuO<sub>x</sub>/CeO<sub>2</sub> system during some of the most relevant applications in heterogeneous catalysis will be discussed. It should be stressed that it is not the aim of this section to provide an extended overview of CuO<sub>x</sub>/CeO<sub>2</sub> catalytic applications, which can be found in several comprehensive reviews [3,49,57,75,76,221]. It mainly aims to provide a general optimization framework towards the development of highly active and cost-effective MOs, paving also the way for the decrease of precious metal content in NMs-based catalysts.

#### 3.1. CO Oxidation

CO oxidation is probably the most studied reaction in heterogeneous catalysis, due to its practical and fundamental importance. The catalytic elimination of CO is of great importance in

various applications involving, among others, automotive exhaust emissions control and fuel cell systems. More importantly, CO oxidation can serve as a prototype reaction to gain insight into the structure-property relationships.

Regarding, at first, the CO oxidation activity of individual  $\text{CuO}_x$  phase, it has been clearly revealed that it is strongly dependent on oxidation state, size and morphology. In particular, the following activity order:  $\text{Cu}_2\text{O} > \text{metastable cluster CuO} > \text{CuO}$  has been revealed, closely related to the ability to release lattice oxygen [222,223]. On the other hand, the exposed crystal planes of  $\text{CuO}_x$  phase drastically affect the CO oxidation; truncated octahedral  $\text{Cu}_2\text{O}$  with {332} facets displayed better activity than low index {111} and {100} planes [224]. Similarly, CuO with exposed {011} planes is more active than close-packed {111} planes [225]. In view of this fact, it has been found that the CO oxidation activity of CuO mesoporous nanosheets with high-index facets is about 35 times higher than that of the commercial sample [226]. In general, surface vacancies, originated from coordinately unsaturated surface Cu atoms, can easily activate oxygen species towards their reaction with the reducing agent [3].

In a similar manner, theoretical and experimental studies have shown that the energy of anionic vacancies formation over bare ceria follows the order: {111} > {100} > {110}, as previously analyzed [82,104,109,112,146,160–166]. Moreover, a large increase in oxygen vacancies concentration has been found for ceria crystal size lower than ca. 10 nm [98], revealing the interrelation between size and shape effects. In this regard, we recently showed that ceria nanorods with {100} and {110} exposed facets demonstrated the optimum CO oxidation activity amongst ceria samples of different morphology; a close relationship between crystal planes-oxygen exchange kinetics-CO oxidation activity was disclosed [115].

In view of the above aspects, it could be argued that by adjusting the shape and size of individual counterparts of MOs ( $\text{CuO}_x$  and  $\text{CeO}_x$  in the case of  $\text{CuO}_x/\text{CeO}_2$  mixed oxides), significant modifications in their redox and catalytic properties can be obtained. However, in view of the fact that “the whole is more than the sum of its part”, the majority of catalytic studies in heterogeneous catalysis is based on  $\text{CuO}_x/\text{CeO}_2$  mixed oxide than on individual oxides [52,227,228]. The underlying mechanism of this synergistic effect linked to metal-support interactions is the subject of numerous theoretical and experimental studies in catalysis. The latest advances in the field of  $\text{CuO}_x$ - $\text{CeO}_2$  interactions and their implications in catalysis have been recently reviewed by one of us [40]. In general, the superiority of binary oxides can be ascribed to various interrelated phenomena, involving among others: (i) Electronic perturbations between nanoparticles, (ii) redox interplay between interfacial sites, (iii) facilitation of the formation of structural defects, (iv) improved reducibility and oxygen mobility, (v) unique reactivity of interfacial sites [40]. However, all of these factors are closely related with the intrinsic and extrinsic characteristics of individual oxides, triggering unique opportunities towards the development of highly active MOs by engineering the size and shape of individual oxides and in turn, the interfacial reactivity. Moreover, chemical or electronic effects induced by aliovalent doping can exert a profound influence on the catalytic performance, offering an additional tool towards the rational design of MOs (Figure 2). In the sequence, the optimization of CO oxidation activity of  $\text{CuO}_x/\text{CeO}_2$  catalysts by means of the above-mentioned approaches is presented, as an indicative example of MOs rational design.

Recently, we thoroughly explored the impact of ceria nanoparticles shape effects on the CO oxidation activity of  $\text{CuO}_x/\text{CeO}_2$  catalysts. The results clearly revealed the significant role of morphology in the CO oxidation activity, following the order: Nanorods (NR) > nanopolyhedra (NP) > nanocubes (NC), Figure 11. However, more importantly, CuO incorporation to different ceria carriers boosted the catalytic performance, without affecting the order observed for bare  $\text{CeO}_2$  (Figure 11), demonstrating the crucial role of support.

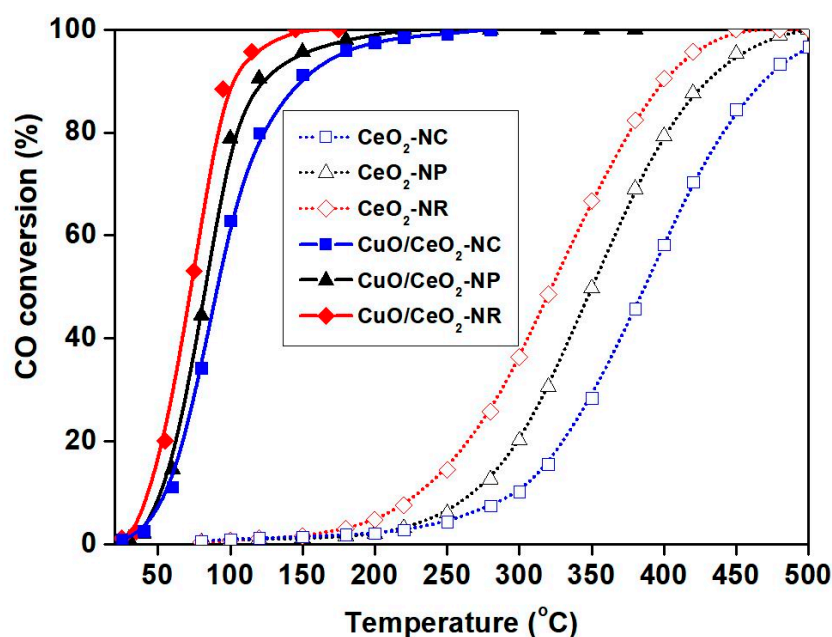


**Figure 11.** CO conversion as a function of temperature for bare CeO<sub>2</sub> and CuO<sub>x</sub>/CeO<sub>2</sub> samples of different morphology (NR, NC and NP, as indicated in each curve). Reaction conditions: 2000 ppm CO, 1 vol.% O<sub>2</sub>, GHSV = 39,000 h<sup>-1</sup> [115].

The CuO<sub>x</sub>/CeO<sub>2</sub>-NR sample exhibited a half-conversion temperature ( $T_{50}$ ) of ca. 70 °C, which is much lower to that required for a typical noble metal oxidation catalyst, such as Pt/Al<sub>2</sub>O<sub>3</sub> ( $T_{50}$  = 230 °C), as shown in Figure 12. Based on a thorough in situ and ex situ characterization study, a perfect relationship between the CO oxidation performance and the following parameters was disclosed: (i) Relative population of Cu<sup>+</sup>/Ce<sup>3+</sup> redox pairs, (ii) abundance of loosely bound oxygen species, expressed in terms of surface-to-bulk oxygen reducibility, (iii) relative concentration of oxygen vacancies, evidenced by the  $I_D/I_{F2g}$  Raman ratio (Figure 7c) [115]. Similar conclusions in relation to the key role of ceria morphology in the CO oxidation activity have been reported by several groups [117,134,154,158,210,212,229–231], most of these revealing the superiority of nanorods.

However, it should be noted that similar or even better catalytic activities can be obtained by different morphologies (e.g., [124,211,212]). In this regard, it was recently shown that sub-nanometer copper oxide clusters (1 wt.% Cu loading) deposited on ceria nanospheres (NS) exhibited superior performance as compared to that deposited on nanorods ( $T_{100}$  = 122 °C vs. 194 °C) [124]. Extensive characterization investigations revealed that the copper species in nanorods samples existed in both Cu-[O<sub>x</sub>]-Ce and CuO<sub>x</sub> clusters, while CuO<sub>x</sub> clusters dominated in nanospheres. Among these species, only CuO<sub>x</sub> clusters could be easily reduced to Cu(I) when they were subjected to interaction with CO, which is considered to be the reason of the enhanced reactivity of CuO<sub>x</sub>/CeO<sub>2</sub>-NS samples [124].

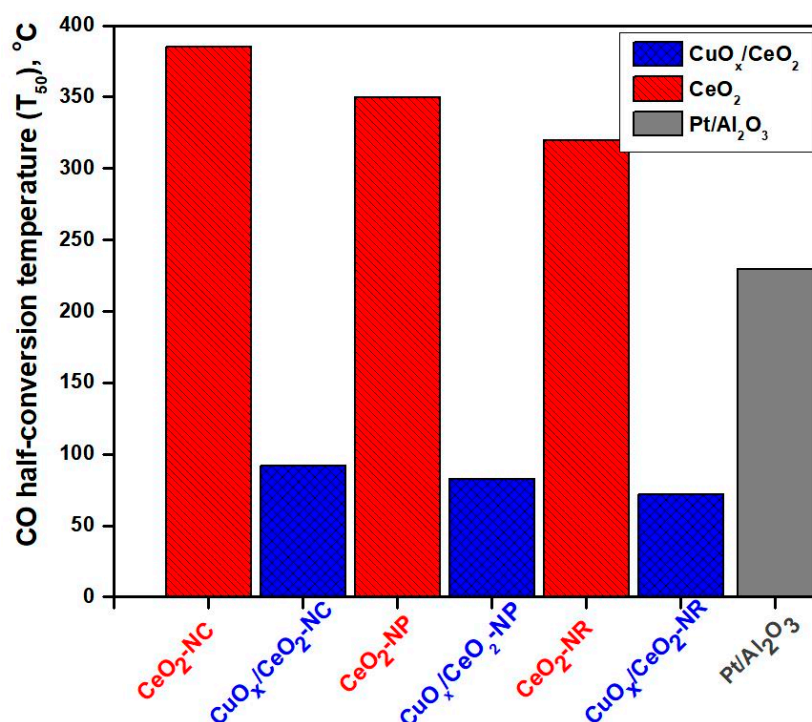


**Figure 12.** A comparison between bare ceria, copper-ceria and a noble metal catalyst, in terms of half-conversion temperature ( $T_{50}$ ) for the oxidation of CO. Reaction conditions: 2000 ppm CO, 1 vol.% O<sub>2</sub>, GHSV = 39,000 h<sup>-1</sup>.

So far, numerous synthesis routes and different precursors have been employed to adjust the structural and morphological characteristics of CuO<sub>x</sub>/CeO<sub>2</sub> composites, mostly summarized by Prasad and Rattan [76]. For instance, it has been found that the use of Ce(III) instead of Ce(IV) precursors can lead to CuO<sub>x</sub>/CeO<sub>2</sub> catalysts with superior reducibility and CO oxidation activity [232]. In particular, it was experimentally shown that Ce(III)-derived samples contained a higher amount of Cu<sup>+</sup> species, through the redox equilibrium  $\text{Cu}^{2+} + \text{Ce}^{3+} \leftrightarrow \text{Cu}^{+} + \text{Ce}^{4+}$ , which are responsible for their enhanced oxidation performance [232]. Moreover, CuO<sub>x</sub>/CeO<sub>2</sub> samples prepared from copper acetate precursor demonstrated better CO oxidation performance as compared to those prepared from nitrate, chloride and sulfate precursors [233]. Avgouropoulos and co-workers [234,235] recently employed a novel hydrothermal method for the synthesis of atomically dispersed CuO<sub>x</sub>/CeO<sub>2</sub> catalysts, offering high CO oxidation performance. By means of various complementary techniques, it was shown that the catalytic activity is mainly related to the nature of highly dispersed copper species rather than the structural/textural characteristics. In a similar manner, Elias et al. [236] reported on the facile synthesis of phase-pure, monodisperse ~3 nm Cu<sub>0.1</sub>Ce<sub>0.9</sub>O<sub>2-x</sub> crystallites via solution-based pyrolysis of heterobimetallic Schiff complexes. An increase of CO oxidation activity by one and three orders of magnitude compared to ceria nanoparticles (3 nm) and microparticles (5 μm), respectively, was attained (Figure 13).

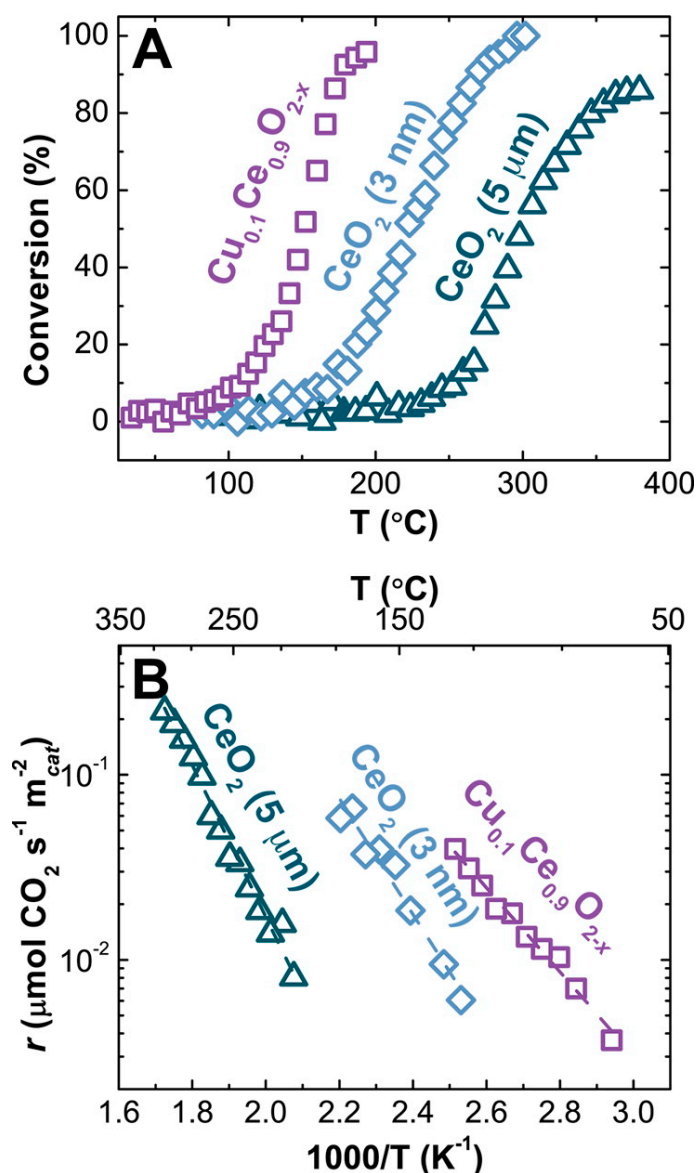


**Figure 13.** CO oxidation on annealed 3 nm Cu<sub>0.1</sub>Ce<sub>0.9</sub>O<sub>2-x</sub>, 3 nm CeO<sub>2</sub> and commercial 5 μm CeO<sub>2</sub> (Sigma-Aldrich). (A) “Light off” curves and (B) area-normalized Arrhenius plots, measured in 1.0% CO, 2.5% O<sub>2</sub> balanced in He at a flow rate of 1300 mL min<sup>-1</sup> g<sub>cat</sub><sup>-1</sup> for 20 mg catalyst loadings. Reproduced with permission from Reference [236]. Copyright© 2014, American Chemical Society.

Besides the engineering of shape and size, porous structure engineering could exert a significant influence on the CO oxidation activity of CuO<sub>x</sub>/CeO<sub>2</sub> catalysts [123,213]. As for example, three-dimensional CuO<sub>x</sub>-doped CeO<sub>2</sub> prepared by a hard template method exhibited complete CO conversion at temperatures as low as 50 °C, due to their improved textural and redox properties [213].

Regarding the influence of CuO<sub>x</sub>/CeO<sub>2</sub> composition on the CO oxidation activity, most of the studies revealed an optimum Cu/(Cu+Ce) atomic ratio in the range of 15–30% [212,231,232,237,238]. Within this specific range, the optimum physicochemical characteristics and interfacial interactions can be achieved, reflected then on catalytic activity.

Apart from the above-described approaches that have been put forward to improve the CO oxidation performance of CuO<sub>x</sub>/CeO<sub>2</sub> oxides, the addition of aliovalent elements as structural/surface promoters should be mentioned. In view of this fact, it has been found that the modification of ceria support by Mn [239] or Sn [240] can drastically modify the dispersion of CuO<sub>x</sub> and the redox

interplay between Cu species and support, thus, enhancing the CO oxidation performance. Very recently, the tuning of the interfacial properties of  $\text{CuO}_x/\text{CeO}_2$  by  $\text{In}_2\text{O}_3$  doping was also explored [241]. It was found that the CO oxidation performance of  $\text{In}_2\text{O}_3\text{-CuO}_x/\text{CeO}_2$  sample greatly exceeds that of parent oxide, offering complete CO conversion at temperatures as low as 100 °C [241]. By means of complementary characterization studies and density functional theory calculations, it was proved that  $\text{In}_2\text{O}_3$  could modify the geometric structure of  $\text{CuO}_x$  particles by reducing their size. The latter results in more metal-support interfacial sites and abundant defects. Moreover, the interaction between In and Cu could modify the electronic state of Cu atoms towards the stabilization of partially reduced Cu sites at the interface [241].

Recently, copper-ceria nanosheets were synthesized by using graphene oxide as a sacrificial template, in an attempt to increase the concentration of active interfacial sites [242]. The copper-ceria interaction was further adjusted by appropriate pretreatment, with the catalyst calcined at 600 °C exhibiting complete CO conversion at 90 °C, due to the high concentration in active copper species and oxygen vacancies [242]. Moreover, a sword-like copper-ceria composite derived by a Ce-based MOF with 5 wt.% Cu loading, exhibited superior CO conversion performance ( $T_{100} = 100$  °C) in comparison to other irregular-shaped catalysts, due to the good interfacial contact, which resulted in the abundance of  $\text{Cu}^+$  active species and oxygen vacancies [191]. Very recently, triple-shelled  $\text{CuO}_x/\text{CeO}_2$  hollow nanospheres were synthesized by MOFs, exhibiting high CO conversion performance ( $T_{100} = 130$  °C) [243]. This was mainly ascribed to the porous structure of the triple-shelled morphology, offering an enhanced synergistic interaction between copper and ceria [243].

Table 1 summarizes, at a glance, indicative attempts followed to adjust the interfacial properties and in turn, the CO oxidation performance of  $\text{CuO}_x/\text{CeO}_2$  binary oxides. It is evident that extremely active composites can be obtained by adjusting the shape, size and electronic/chemical state by means of appropriate synthetic and/or promotional routes. It is of worth pointing out the superiority of finely-tuned  $\text{CuO}_x/\text{CeO}_2$  samples as compared to noble metal-based catalysts, offering unique opportunities towards the rational design of highly active metal oxide catalysts. Moreover, as further guidance, it would be of particular importance to explore the combining effect of different adjusted parameters (e.g.,  $\text{CuO}_x/\text{CeO}_2$  nanorods co-doped with main-group elements) towards further optimization.

**Table 1.** Indicative studies towards adjusting the CO oxidation performance of CuO<sub>x</sub>/CeO<sub>2</sub> oxides.

Reaction Conditions	Adjusted Parameter (Employed Method)	Optimum System	T <sub>50</sub> (°C)	Reference
0.2% CO + 1.0% O <sub>2</sub> ; WHSV = 75,000 mL g <sup>-1</sup> h <sup>-1</sup> ; GHSV = 39,000 h <sup>-1</sup>	shape/size (hydrothermal synthesis)	8.5 wt.% Cu/CeO <sub>2</sub> -nanorods	72	[115]
1.0% CO + 15.0% O <sub>2</sub> ; WHSV = 7200 mL g <sup>-1</sup> h <sup>-1</sup>	shape/size (hydrothermal synthesis)	15 wt.% Cu/CeO <sub>2</sub> -nanorods CeO <sub>2</sub> (15 nm), CuO (6.0 nm)	50	[210]
1.0% CO + 20.0% O <sub>2</sub> ; WHSV = 80,000 mL g <sup>-1</sup> h <sup>-1</sup>	shape/size (alcothermal method)	1.0 wt.% Cu/CeO <sub>2</sub> -nanospheres (~130–150 nm spheres comprised of 2–5 nm nanoparticles)	85	[124]
1.0% CO + 2.5% O <sub>2</sub> ; WHSV = 78,000 mL g <sup>-1</sup> h <sup>-1</sup>	size/structure (solution-based pyrolysis of heterobimetallic Schiff complexes)	Cu <sub>0.1</sub> Ce <sub>0.9</sub> O <sub>2-x</sub> monodisperse nanoparticles (~3.0 nm)	150	[236]
1.0% CO + 10.0% O <sub>2</sub> ; WHSV = 60,000 mL g <sup>-1</sup> h <sup>-1</sup>	size/structure (thermolytic decomposition in the presence of capping agent)	9.0 at.% Cu/CeO <sub>2</sub> CeO <sub>2</sub> (3.3 nm)	85	[211]
1.0% CO, air balance; WHSV = 30,000 mL g <sup>-1</sup> h <sup>-1</sup>	size/structure (hydrothermal treatment)	Cu/CeO <sub>2</sub> -nanospheres (Cu/(Cu+Ce) = 0.33, spherical particles of 300–400 nm diameter composed of nanoparticles of ca. 10 nm)	70	[212]
0.24% CO + 15.0% O <sub>2</sub> ; WHSV = 60,000 mL g <sup>-1</sup> h <sup>-1</sup>	size/structure (hard template method)	10 mol.% Cu/CeO <sub>2</sub> -microspheres	150	[123]
1.0% CO, air balance; WHSV = 10,000 mL g <sup>-1</sup> h <sup>-1</sup>	size/structure (hard template method)	three-dimensional (3D) Cu/CeO <sub>2</sub> ((Cu/Cu+Ce) = 0.2)	34	[213]
1.0% CO + 21.0% O <sub>2</sub> ; WHSV = 60,000 mL g <sup>-1</sup> h <sup>-1</sup>	shape (thermal annealing of CeMOF precursors)	8.0 wt.% Cu/CeO <sub>2</sub> -triple-shelled hollow nanospheres	110	[243]
1.0% CO, air balance; WHSV = 52,000 mL g <sup>-1</sup> h <sup>-1</sup>	electronic/chemical state (doping by urea combustion method)	5.0 wt.% Cu/Ce <sub>0.9</sub> Mn <sub>0.1</sub> O <sub>2</sub>	120	[239]
2.4% CO + 1.2% O <sub>2</sub> ; WHSV = 32,000 mL g <sup>-1</sup> h <sup>-1</sup>	electronic/chemical state (doping by combustion method)	6.0 wt.% Cu/Ce <sub>0.7</sub> Sn <sub>0.3</sub> O <sub>2</sub>	80	[240]
1.0% CO + 20.0% O <sub>2</sub> ; WHSV = 60,000 mL g <sup>-1</sup> h <sup>-1</sup>	electronic/chemical state (doping by wetness co-impregnation method)	In <sub>2</sub> O <sub>3</sub> -CuO <sub>x</sub> /CeO <sub>2</sub> 1.25 wt.% In, 5.0 wt.% Cu	73	[241]
1.0% CO + 1.0% O <sub>2</sub> ; GHSV = 9600 h <sup>-1</sup>	-	1.0 wt.% Pt/CeO <sub>2</sub>	70	[244]
1.0% CO + 20.0% O <sub>2</sub> ; WHSV = 60,000 mL g <sup>-1</sup> h <sup>-1</sup>	-	3.0 wt.% Pd/CeO <sub>2</sub>	120	[241]
0.95% CO + 1.75% O <sub>2</sub> ; WHSV = 12,000 mL g <sup>-1</sup> h <sup>-1</sup>	-	0.2 wt.% Pd/CeO <sub>2</sub>	180	[245]

WHSV: Weight hourly space velocity [=] mL g<sup>-1</sup> h<sup>-1</sup>; GHSV: Gas hourly space velocity [=] h<sup>-1</sup>.

### 3.2. N<sub>2</sub>O Decomposition

Nitrous oxide (N<sub>2</sub>O) has been lately recognized as one of the most potent greenhouse gases and ozone depleting substances [246]. In view of this fact, the catalytic abatement of N<sub>2</sub>O has received particular attention as one of the most promising remediation methods. Although noble metals exhibit satisfactory activity, their high cost and sensitivity to various substances (e.g., O<sub>2</sub>, H<sub>2</sub>O) hinder widespread applications. Hence, as previously stated, noble metal-free composites have gained particular attention as potential candidates. The recent advances in the field of N<sub>2</sub>O decomposition over metal oxides have been recently reviewed by Konsolakis [246]. It was clearly revealed that MOs could be effectively applied for N<sub>2</sub>O decomposition, demonstrating comparable or even better catalytic performance compared to NMs-based catalysts. More interestingly, and in line with the aim and scope of the present article, it was shown that very active and stable MOs could be obtained by adjusting their size, shape and electronic state through appropriate synthesis and promotional routes [246].

Herein, we shortly present the main approaches lately followed to improve the deN<sub>2</sub>O performance of MOs, exemplified by the CuO<sub>x</sub>/CeO<sub>2</sub> system. Table 2 presents indicative studies towards this direction, involving our recent advances in the field [215,247]. It is of worth noticing the comparable or even superior deN<sub>2</sub>O performance of finely-tuned CuO<sub>x</sub>/CeO<sub>2</sub> samples as compared to noble metal-based catalysts (Table 2).

Recently, we explored the impact of synthesis procedure (impregnation, co-precipitation and exotemplating methods) on the deN<sub>2</sub>O performance of CuO<sub>x</sub>/CeO<sub>2</sub> mixed oxides [247]. Co-precipitation method resulted in the optimum performance, offering complete N<sub>2</sub>O conversion at ca. 550 °C. On the basis of characterization results (XPS, TPR, micro-Raman), the superiority of precipitated samples was ascribed to their enhanced reducibility and the facilitation of Ce<sup>4+</sup>/Ce<sup>3+</sup> and Cu<sup>2+</sup>/Cu<sup>+</sup> redox cycles. In an attempt to further improve the deN<sub>2</sub>O performance of CuO<sub>x</sub>/CeO<sub>2</sub> samples, very recently, we explored the potential to further adjust the local surface chemistry and metal-support interactions by means of electronic (alkali) promotion. Notably, the results showed that by co-adjusting the synthesis procedure and the electronic state, highly active deN<sub>2</sub>O catalysts could be obtained; the sample with a Cs content of 1.0 at Cs/nm<sup>2</sup> offers a half-conversion temperature (T<sub>50</sub>) about 200 °C lower as compared to the commercial sample (Figure 14) [215]. The superiority of Cs-doped samples was ascribed to the electronic effect of alkali doping towards stabilizing partially reduced Cu<sup>+</sup>/Ce<sup>3+</sup> pairs, which play a pivotal role in the deN<sub>2</sub>O process [215,246].

**Table 2.** Indicative studies followed to adjust the deN<sub>2</sub>O performance of CuO<sub>x</sub>/CeO<sub>2</sub> oxides.

Reaction Conditions	Adjusted Parameter (Employed Method)	Optimum System	T <sub>50</sub> (°C)	Reference
0.26% N <sub>2</sub> O; GHSV = 19,000 h <sup>-1</sup>	composition (citrate acid method)	67 mol.% Cu/CeO <sub>2</sub>	370	[214]
0.25% N <sub>2</sub> O; GHSV = 45,000 h <sup>-1</sup>	composition (hard template replication)	40 mol.% Cu/CeO <sub>2</sub>	440	[248]
0.1% N <sub>2</sub> O; WHSV = 90,000 mL g <sup>-1</sup> h <sup>-1</sup>	size/structure (various synthesis methods)	20 wt.% Cu/CeO <sub>2</sub> prepared by co-precipitation, CeO <sub>2</sub> (11.8 nm)	465	[247]
0.1% N <sub>2</sub> O; WHSV = 90,000 mL g <sup>-1</sup> h <sup>-1</sup>	size/structure (co-precipitation method) and electronic state (alkali addition)	Cs-doped (1.0 at/nm <sup>2</sup> ) Cu/CeO <sub>2</sub> CeO <sub>2</sub> (13.5 nm)	420	[215]
0.2% N <sub>2</sub> O; WHSV = 60,000 mL g <sup>-1</sup> h <sup>-1</sup>	size/structure (hydrothermal method)	molar ratio Cu/Ce = 1, CeO <sub>2</sub> (7.0 nm), CuO (24 nm)	380	[216]
0.25% N <sub>2</sub> O; WHSV = 120,000 mL g <sup>-1</sup> h <sup>-1</sup>	shape (hydrothermal method)	4.0 wt.% Cu/CeO <sub>2</sub> -nanorods	430	[146]
0.25% N <sub>2</sub> O; WHSV = 60,000 mL g <sup>-1</sup> h <sup>-1</sup>	shape (glycothermal method)	10 wt.% Cu/CeO <sub>2</sub> -nanospheres	380	[205]
0.1% N <sub>2</sub> O; WHSV = 60,000 mL g <sup>-1</sup> h <sup>-1</sup>	-	0.5 wt% Rh/Al <sub>2</sub> O <sub>3</sub>	340	[249]
0.1% N <sub>2</sub> O; WHSV = 60,000 mL g <sup>-1</sup> h <sup>-1</sup>	-	0.5 wt% Pt/Al <sub>2</sub> O <sub>3</sub>	500	[249]
0.1% N <sub>2</sub> O; WHSV = 60,000 mL g <sup>-1</sup> h <sup>-1</sup>	-	0.5 wt% Pd/Al <sub>2</sub> O <sub>3</sub>	>500	[249]

WHSV: Weight hourly space velocity [=] mL g<sup>-1</sup> h<sup>-1</sup>; GHSV: Gas hourly space velocity [=] h<sup>-1</sup>.

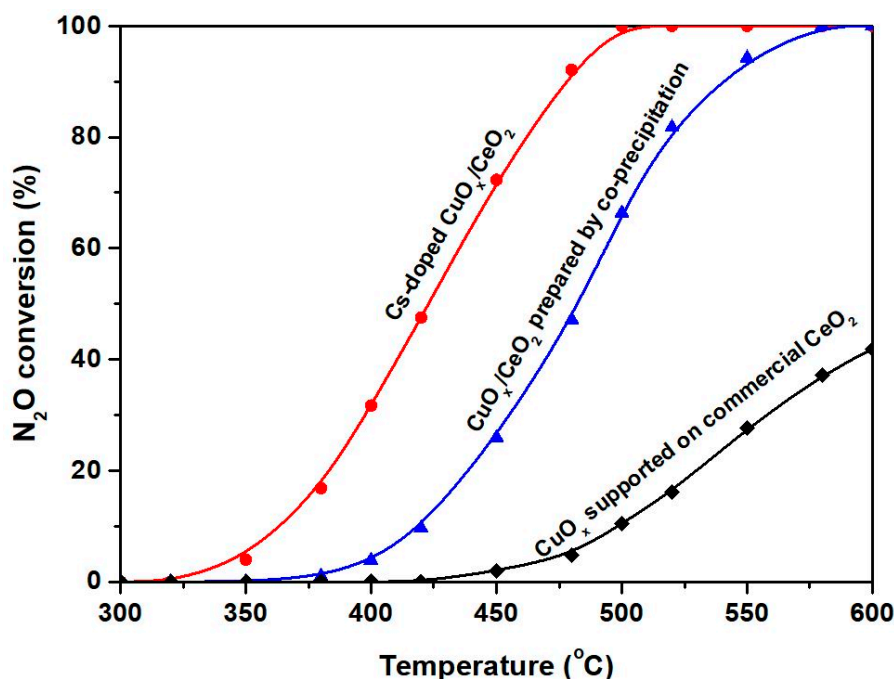


**Figure 14.** Optimization of deN<sub>2</sub>O performance of CuO<sub>x</sub>/CeO<sub>2</sub> mixed oxides by co-adjusting synthesis parameters (co-precipitation method) and electronic state (alkali addition). For comparison, the corresponding performance of CuO<sub>x</sub> supported on commercial ceria is included. Reaction conditions: 0.1% N<sub>2</sub>O balanced with He; WHSV = 90,000 mL g<sup>-1</sup> h<sup>-1</sup> [215].

The effect of ceria morphology (nanorods, nanocubes, nanopolyhedra) on the deN<sub>2</sub>O performance of CuO<sub>x</sub>/CeO<sub>2</sub> composites was extensively investigated by Pintar and co-workers [146]. Copper clusters located on {100} and {110} planes—preferentially exposed on ceria nanorods—exhibit a normalized activity ca. 20% higher compared to {111} planes of polyhedra (Figure 15). In terms of conversion performance, the 4.0 wt.% CuO<sub>x</sub>/Ceria-nanorods exhibited a half-conversion temperature (T<sub>50</sub>) of about 430 °C compared to 440 °C and 470 °C of nanopolyhedra and nanocubes, respectively. On the basis of a thorough characterization study, it was disclosed that the oxygen mobility and the regeneration of active Cu phase are easier on ceria nanorods, which in turn, facilitates the deN<sub>2</sub>O activity through oxygen desorption and replenishment of active sites [146]. In a similar manner, CuO<sub>x</sub> supported on CeO<sub>2</sub> nanospheres exhibited high deN<sub>2</sub>O performance (T<sub>50</sub> = 380 °C, Table 2), ascribed mainly to the high population of CuO<sub>x</sub> clusters on the high surface area CeO<sub>2</sub> nanospheres [205]. These findings clearly demonstrate the significant advances that can be achieved in the deN<sub>2</sub>O process by engineering the size and shape of metal oxide composites.

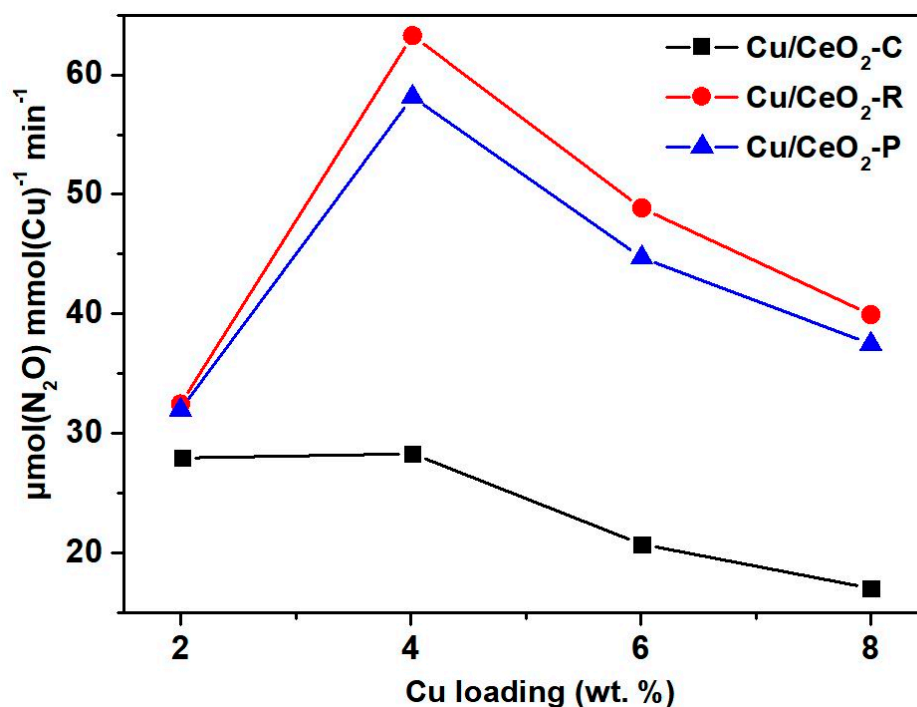


**Figure 15.** The activity of nanoshaped  $\text{CuO}_x/\text{CeO}_2$  catalysts measured at  $T = 375$  °C. Adapted from Reference [146]. Copyright© 2015, American Chemical Society.

### 3.3. Preferential Oxidation of CO (CO-PROX)

The copper-ceria binary oxides are amongst the most widely investigated catalytic systems in the preferential oxidation of carbon monoxide (CO-PROX), a reaction used for the production of highly purified hydrogen and the removal of CO.  $\text{CuO}_x/\text{CeO}_2$  catalysts have gained particular attention in CO-PROX process, due to their superior performance, which is mainly ascribed to the peculiar properties of copper-ceria interface [40].

In the light of the above-mentioned size, shape and electronic/chemical effects, numerous efforts have been put forward towards optimizing the CO-PROX performance. Indicative approaches followed to fine-tune the CO-PROX performance are summarized in Table 3, and further discussed below.

**Table 3.** Indicative studies towards adjusting the CO preferential oxidation performance of CuO<sub>x</sub>/CeO<sub>2</sub> oxides.

Reaction Conditions	Adjusted Parameter (Employed Method)	Optimum System	Maximum CO Conversion	Reference
1.0% CO + 1.0% O <sub>2</sub> + 50.0% H <sub>2</sub> ; WHSV = 60,000 mL g <sup>-1</sup> h <sup>-1</sup>	composition (hydrothermal method)	5.0 wt.% Cu/CeO <sub>2</sub>	99.6% at 130 °C	[250]
1.0% CO + 1.0% O <sub>2</sub> + 50.0% H <sub>2</sub> ; WHSV = 60,000 mL g <sup>-1</sup> h <sup>-1</sup>	composition (co-precipitation method)	30 at.% Cu/CeO <sub>2</sub>	~92% at 143 °C	[251]
1.0% CO + 1.0% O <sub>2</sub> + 10.0% H <sub>2</sub> O + 15.0% CO <sub>2</sub> + 50.0% H <sub>2</sub> ; WHSV = 30,000 mL g <sup>-1</sup> h <sup>-1</sup>	composition (sol-gel precipitation/ chelating-impregnation)	10 wt.% Cu/CeO <sub>2</sub>	~99.5% at 100 °C	[252]
1.0% CO + 1.0% O <sub>2</sub> + 40.0% H <sub>2</sub> ; WHSV = 30,000 mL g <sup>-1</sup> h <sup>-1</sup>	composition (nanocasting method)	7.0 wt.% Cu/CeO <sub>2</sub>	100% at 110 °C	[253]
1.2% CO + 1.2% O <sub>2</sub> + 50.0% H <sub>2</sub> ; WHSV = 20,000 mL g <sup>-1</sup> h <sup>-1</sup>	composition/size (freeze-drying method)	6.0 wt.% Cu/CeO <sub>2</sub> CeO <sub>2</sub> (9.9 nm), CuO (10.7 nm)	100% at 90 °C	[254]
1.0% CO + 1.0% O <sub>2</sub> + 50.0% H <sub>2</sub> ; WHSV = 16,000 mL g <sup>-1</sup> h <sup>-1</sup>	composition/size (solvent-free method, cupric nitrate as a copper precursor)	7.5 wt.% Cu/CeO <sub>2</sub> CeO <sub>2</sub> (16.3 nm)	100% at 120 °C	[255]
1.0% CO + 1.0% O <sub>2</sub> + 50.0% H <sub>2</sub> WHSV = 40,000 mL g <sup>-1</sup> h <sup>-1</sup>	chemical state (ultrasound-aided impregnation)	Cu <sub>0.4</sub> Ce <sub>0.6</sub> O/CNTs	100% at 120 °C	[256]
1.25% CO + 1.25% O <sub>2</sub> + 50.0% H <sub>2</sub> ; WHSV = 20,000 mL g <sup>-1</sup> h <sup>-1</sup>	size (Poly(methyl metacrylate) as a template)	6.0 wt.% Cu/CeO <sub>2</sub> CeO <sub>2</sub> (5.6 nm)	100% at 115 °C	[257]
1.0% CO + 1.0% O <sub>2</sub> + 50.0% H <sub>2</sub> ; WHSV = 36,000 mL g <sup>-1</sup> h <sup>-1</sup>	shape (hydrothermal method)	4.0 wt.% Cu/CeO <sub>2</sub> -octahedra	95% at 140 °C	[258]
1.0% CO + 1.0% O <sub>2</sub> + 50.0% H <sub>2</sub> ; WHSV = 60,000 mL g <sup>-1</sup> h <sup>-1</sup>	shape (hydrothermal method)	5.0 wt.% Cu/CeO <sub>2</sub> -rods/polyhedra	>99.0% at 95/90 °C	[157]
1.0% CO + 1.0% O <sub>2</sub> + 50.0% H <sub>2</sub> ; WHSV = 40,000 mL g <sup>-1</sup> h <sup>-1</sup>	shape (hydrothermal method)	Cu/CeO <sub>2</sub> -spheres CeO <sub>2</sub> /CuO = 5	100% at 95 °C	[116]
1.0% CO + 1.0% O <sub>2</sub> + 50.0% H <sub>2</sub> ; WHSV = 16,000 mL g <sup>-1</sup> h <sup>-1</sup>	shape (alcothermal method)	5.0 wt.% Cu/CeO <sub>2</sub> -spheres	100% at 100 °C	[259]
1.0% CO + 1.0% O <sub>2</sub> + 50.0% H <sub>2</sub> ; WHSV = 40,000 mL g <sup>-1</sup> h <sup>-1</sup>	shape (self-templating method)	Cu/CeO <sub>2</sub> -triple-shelled hollow microspheres	100% at 95 °C	[260]
1.0% CO + 1.0% O <sub>2</sub> + 50.0% H <sub>2</sub> ; WHSV = 120,000 mL g <sup>-1</sup> h <sup>-1</sup>	electronic/chemical state (potassium doping/carbon nanotubes)	Cu/CeO <sub>2</sub> /CNTs (2.5 wt.% Cu, 20 wt.% CeO <sub>2</sub> , alkali/Cu = 0.68)	100% at 175 °C	[261]
1.0% CO + 1.0% O <sub>2</sub> + 50.0% H <sub>2</sub> ; WHSV = 60,000 mL g <sup>-1</sup> h <sup>-1</sup>	pretreatment (with hydrogen)	10 wt.% Cu/CeO <sub>2</sub>	72% at 80 °C	[262]
1.0% CO + 1.0% O <sub>2</sub> + 50.0% H <sub>2</sub> ; WHSV = 60,000 mL g <sup>-1</sup> h <sup>-1</sup>	pretreatment (with 2 M NaOH and etched with an ionic liquid)	10 wt.% Cu/CeO <sub>2</sub>	100% at 150 °C	[263]
1.0% CO + 1.25% O <sub>2</sub> + 50.0% H <sub>2</sub> ; WHSV = 25,000 mL g <sup>-1</sup> h <sup>-1</sup>	pretreatment (with HNO <sub>3</sub> , pH < 4)	7.5 wt.% Cu/CeO <sub>2</sub>	100% at 137 °C	[264]

WHSV: Weight hourly space velocity [=] mL g<sup>-1</sup> h<sup>-1</sup>.

Several copper-ceria catalytic systems of various copper loadings have been synthesized by different methods, with the optimum Cu loading varying between 5 and 10 wt.% [250,252–254,265]. A further increase in Cu content from 10 to 15 wt.% has been reported to reduce the catalytic activity, due to the large  $\text{CuO}_x$  agglomerates on the catalyst surface [252]. It was revealed, by means of both ex situ and in situ characterization studies, that the desired CO oxidation process is related to partially reduced  $\text{Cu}^+$  species, whereas, highly reduced copper species not strongly associated with  $\text{CeO}_2$  favor the undesired  $\text{H}_2$  oxidation [40,250,265–267]. In view of this fact, extensive research efforts have been put forward to control the two competitive oxidation processes by appropriately adjusting the geometric and electronic interactions between copper and ceria through the above-described fine-tuning approaches.

Regarding the shape effect, different copper-ceria nanostructures (rods, cubes, spheres, octahedra, spindle or multi-shelled morphologies) have been synthesized and studied for the CO-PROX reaction. It was revealed that the shape-controlled synthesis of ceria nanoparticles has a profound influence on the CO-PROX activity and selectivity. In particular, it was found that rod-shaped and polyhedral copper-ceria systems exhibited higher CO conversion performance ( $T_{50} = 68^\circ\text{C}$ ) at low-temperatures, as compared to plates ( $T_{50} = 71^\circ\text{C}$ ) and cubes ( $T_{50} = 89^\circ\text{C}$ ) [157]. The latter was mainly attributed to the smaller  $\text{CuO}_x$  clusters subjected to a strong interaction with the ceria carrier, which, in turn, facilitates the formation of  $\text{Cu}^+$  sites and oxygen vacancies [157]. More importantly, a close relationship between measurable physicochemical parameters, such as the amount of  $\text{Cu}^+$  species and the  $A_{584}/A_{454}$  Raman ratio (related to oxygen vacancies) with the catalytic performance was obtained (Figure 16); rod- and polyhedral-shaped samples exhibited the highest values on  $\text{Cu}^+$  species and oxygen vacancies, demonstrating, also, the optimum CO-PROX performance [157].

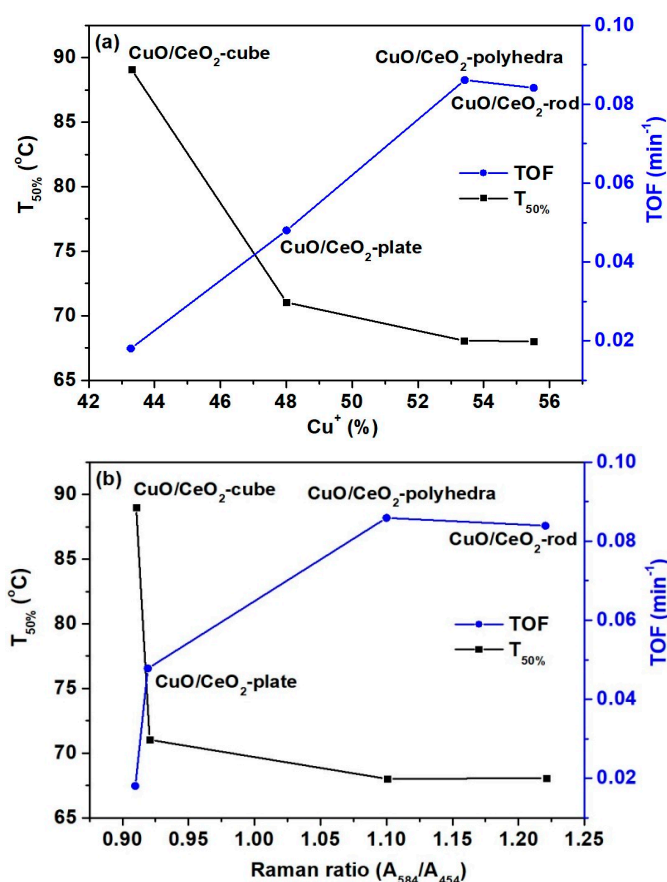


**Figure 16.** (a) TOF (60 °C)/T<sub>50%</sub> values versus  $\text{Cu}^+$  content and (b) TOF (60 °C)/T<sub>50%</sub> values versus  $A_{584}/A_{454}$  ratios for CuO/CeO<sub>2</sub> catalysts with different morphologies. Adapted from Reference [157]. Copyright© 2016, Royal Society of Chemistry.

In this point, it should be mentioned that in relation to which ceria shape is the most active or selective for the CO-PROX process, inconclusive results are acquired, due to the different reaction conditions applied (see Table 3) in conjunction to the complexity of CO-PROX process, which is affected to a different extent by the various interrelated parameters (e.g., reducibility, metal dispersion, oxygen vacancies, oxidation state, metal-support interactions). Under this perspective, it was reported that copper-ceria nanocubes exhibited higher CO<sub>2</sub> selectivity than copper-ceria nanorods or nanospheres, due to the difficulty of nanocubes to fully reduce the copper oxide species under CO-PROX conditions [133,268], while, at the same time, exhibiting lower CO conversion than nanorods [268] and nanospheres [133]. In a similar manner, CuO<sub>x</sub>/CeO<sub>2</sub> spheres and spindles, exposing {111} and {002} facets, showed the highest CO conversion ( $T_{50} = 69$  and  $74$  °C, respectively), as well as a wide temperature window for total CO conversion ( $95$ – $195$  °C for spheres and  $115$ – $215$  °C for spindles), in comparison with octahedrons, cubes and rods [116]. Interestingly, in different shaped ceria nanostructures, a close relationship is found between the concentration of oxygen vacancies and the amount of reduced copper species (Figure 17), clearly revealing the key role of exposed facets towards adjusting the catalytic performance. These findings were further substantiated by DFT calculations (Figure 18), showing the high population of oxygen vacancies at the intersection of {111} and {002} facets in opposition to CeO<sub>2</sub> {111} surface [116].

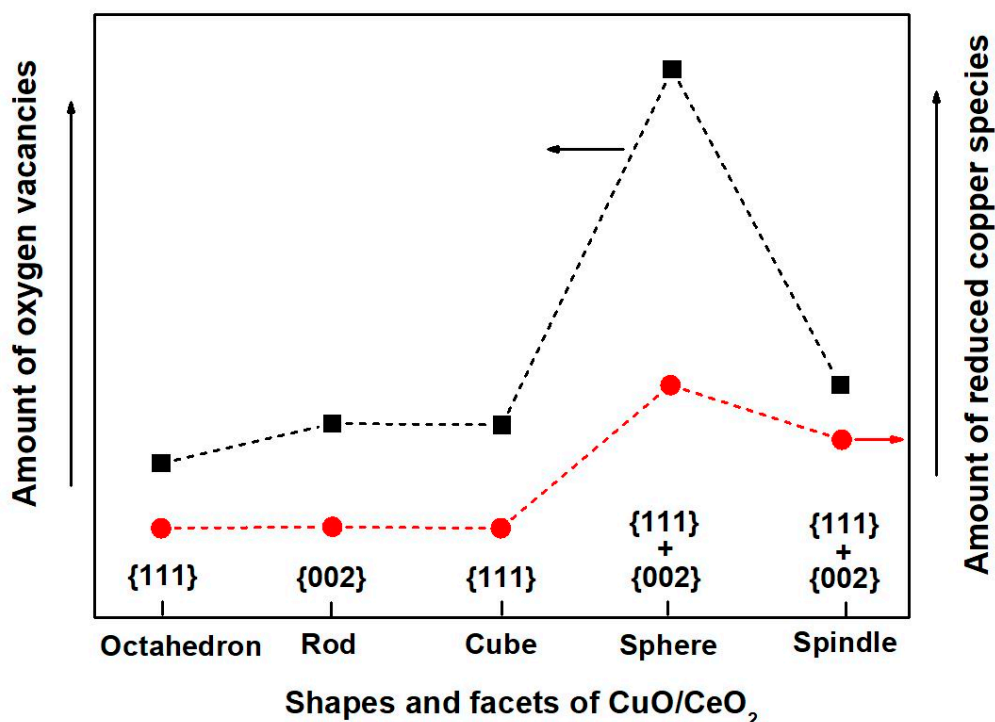


**Figure 17.** Plots of the number of oxygen vacancies and reduced copper species for the CuO/CeO<sub>2</sub> catalysts with different support shapes. Adapted from Reference [116]. Copyright© 2018, Elsevier.

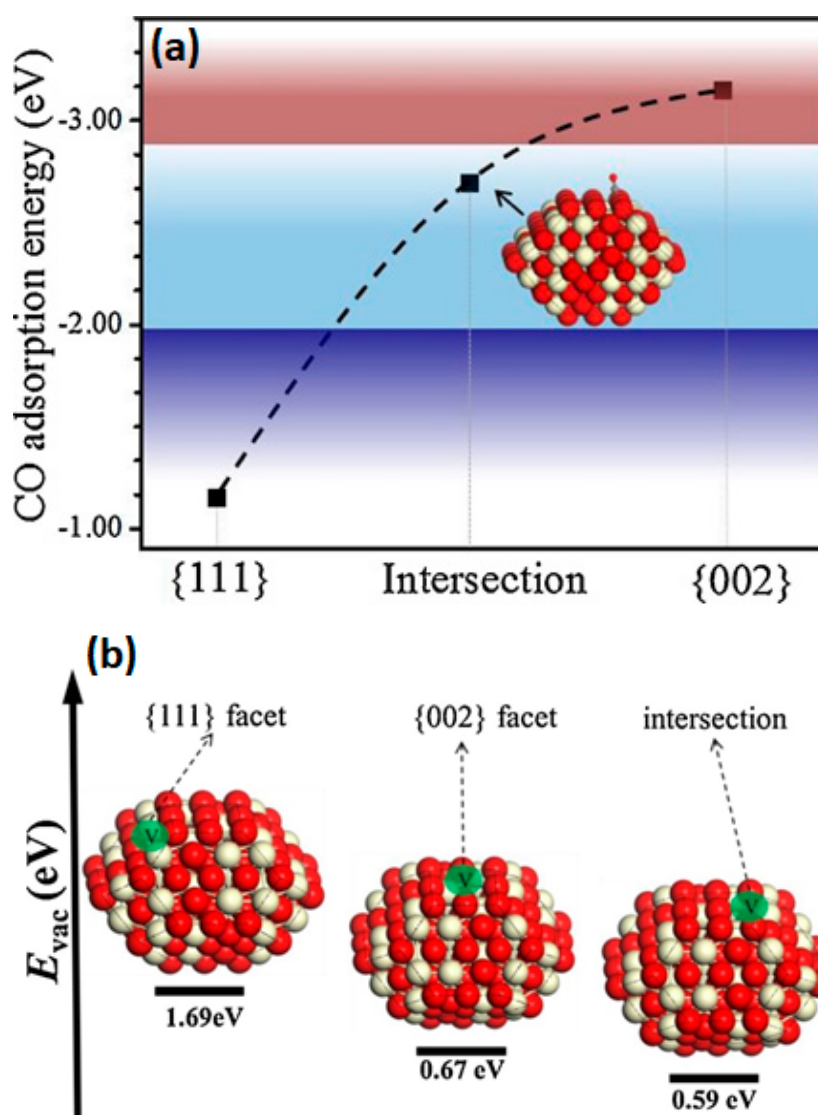


**Figure 18.** (a) DFT-calculated adsorption energy for molecularly adsorbed CO on {111}, {002} facets and their intersection sites of a Ce<sub>60</sub>O<sub>120</sub> cluster obtained, (b) Models of the optimized geometries of Ce<sub>60</sub>O<sub>119</sub> with an oxygen vacancy in the highlighted positions: {111}, {002} facets and their intersection, and values of oxygen vacancy formation energy ( $E_{vac}$ ) below models. (Color code: O in red, Ce in grey, oxygen vacancy in the highlighted circle labeled “V”). Reproduced with permission from Reference [116]. Copyright© 2018, Elsevier.

In an attempt to optimize the CO-PROX performance through size and shape engineering single- and multi-shelled copper-ceria hollow microspheres were synthesized [260,269]. By tuning the number of shells, the catalytic activity was notably improved, with the triple-shelled structure (Figure 19) exhibiting the highest activity and selectivity (100% CO conversion and 91% CO<sub>2</sub> selectivity at 95 °C), as well as a wide temperature window for complete CO conversion (95–195 °C) [260]. The increase in the number of shells enhances the electronic and geometric interaction between copper and ceria, offering a high population of exposed active sites and an increased space inside the catalyst which facilitates reactants accessibility [260].

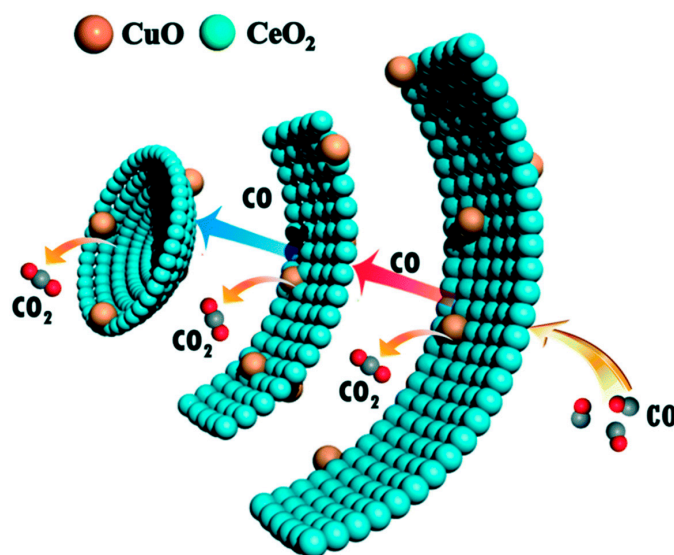


**Figure 19.** Schematic diagrams for CO-PROX over the  $\text{CuO}_x/\text{CeO}_2$  hollow microsphere catalysts with triple shells. Reproduced with permission from Reference [260]. Copyright© 2019, Royal Society of Chemistry.

Taking into account the pivotal role of nanoparticles crystallite size/shape and their consequent effect on metal-support interactions, different preparation routes have been investigated for the synthesis of copper-ceria composites, such as the hydrothermal method, the template-assisted method, the solid-state preparation method, sol-gel, co-precipitation, freeze-drying, deposition-precipitation, etc. [250,251,253–255,257,262,270]. For instance, template-assisted synthesis resulted in small ceria crystallite sizes (ca. 5.6 nm), and thus, in a high population of copper-ceria interfacial sites with implications in Cu oxidation state and CO-PROX activity [257]. Moreover, the precursor compounds or the template agent used during the synthesis procedure can affect the pore size and volume or the reducibility of the materials [255,271]. Interestingly, ethanol washing during the preparation of  $\text{CuO}_x/\text{CeO}_2$  oxides leads to decreased particle sizes, as it affects the dehydration process between precursors particles, resulting in decreased adsorbed water and improved dispersion [272]. Very recently, a novel ultrasound-assisted precipitation method was employed to adjust the defective structure of  $\text{CeO}_2$  and in turn, the CO-RPOX activity [273]. By means of characterization techniques and theoretical calculations, it was shown that only two-electron defects on ceria surface (i.e., defects adsorbing oxygen to form peroxides instead of superoxide species which are formed on one-electron defects) were responsible for the formation of  $\text{Cu}^+$  and  $\text{Ce}^{3+}$  species, which were intimately involved in the CO adsorption and oxygen activation processes [273]. In particular, the adsorption of  $\text{O}_2$  on two-electron defects resulted in peroxides formation, followed by Cu ions incorporation towards the development of Cu-O-Ce structure. Meanwhile, the two additional electrons in the two-electron defects facilitate the electronic re-dispersion in Cu-O-Ce structure, leading to the creation of  $\text{Cu}^+$  (CO adsorption sites) and  $\text{Ce}^{3+}$  (oxygen activation sites).

Another approach in the direction of catalysts functionalization that has attracted considerable attention in recent years is the preparation of inverse catalytic systems. In particular, the co-existence of  $\text{Cu}^+$  and  $\text{Cu}^{2+}$  ions was observed in star-shaped inverse  $\text{CeO}_2/\text{CuO}_x$  catalysts which exhibited high catalytic activity [274]. Moreover, the alteration of Ce/Cu molar ratio and/or the pH value in the inverse  $\text{CeO}_2/\text{CuO}_x$  catalysts notably affects the morphology and the particle size, which in turn, favor the contact interface between ceria and copper, and thus, the CO oxidation at the expense of  $\text{H}_2$  oxidation in PROX process [44]. In addition, a multi-step synthetic approach has been applied for a high concentration of oxygen vacancies to be successfully anchored at the interfaces of the inverse  $\text{CeO}_2/\text{CuO}_x$  system, leading to outstanding CO-PROX activity (~100% CO conversion at a wide temperature window 120–210 °C) and adequate stability [275].

The doping effect on the CO-PROX performance has also been studied in the inverse copper-ceria catalysts [276,277]. It was reported that doping ceria with transition metals (e.g., Fe, Co, Ni) induces changes in the ceria lattice and in the formation of oxygen vacancies [276]. The doping element affects the reducibility of the  $\text{CeO}_2/\text{CuO}_x$  catalysts, while promoting the formation of  $\text{Ce}^{3+}$  ions and oxygen vacancies, with the NiO-doped  $\text{CeO}_2/\text{CuO}_x$  catalyst exhibiting the highest activity ( $T_{50} = 68^\circ\text{C}$ ) and the widest temperature window for total CO conversion ( $115\text{--}155^\circ\text{C}$ ) [276]. In the inverse copper-ceria catalysts, it has also been found that the presence of Zn improves the CO-PROX performance, as it has the ability to hinder the CuO reduction to highly reduced copper sites which provide the active sites for the  $\text{H}_2$  oxidation [277].

By applying appropriate pretreatment protocols, the CO-PROX performance may also be greatly affected. In particular, the pretreatment of copper-ceria catalysts in an oxidative or reductive atmosphere affects the amount and dispersion of the active species, and consequently, the catalytic performance [262]. The pretreatment with hydrogen led to a breakage of the  $\text{Cu}\text{--}[\text{O}_x]\text{--}\text{Ce}$  structure, which resulted in enhanced catalytic performance, indicating the significance of the highly dispersed  $\text{CuO}_x$  clusters in the CO-PROX process [262]. Furthermore, the pretreatment in an acidic or a basic environment affects the interaction between the two oxide phases. For instance, the pretreatment of ceria spheres in a basic solvent (2M NaOH), followed by etching in an ionic liquid for the acquisition of ceria nanocubes, resulted in the best catalytic activity at temperatures lower than  $150^\circ\text{C}$ , due to the strong interaction between the highly dispersed  $\text{CuO}_x$  clusters and ceria support [263]. An acidic treatment with nitric acid in nanorod-shaped  $\text{CuO}_x/\text{CeO}_2$  catalysts has also been performed by Avgouropoulos and co-workers [264]. It was found that a highly acidic environment ( $\text{pH} < 4$ ) led to an enrichment of catalysts surface in  $\text{Cu}^+$  species and to high concentrations of oxygen vacancies and  $\text{Ce}^{3+}$  species, while facilitating the formation of surface hydroxyls that are considered responsible for controlling the interfacial interactions in the copper-ceria binary system [264]. All the above-mentioned characteristics in conjunction with the better copper dispersion and the improved reducibility of the highly acidic catalysts resulted in enhanced catalytic performance ( $T_{50} \approx 84^\circ\text{C}$ ) [264]. The same group has also investigated the pretreatment effect of employing ammonia solutions in copper-ceria nanorods [278]. It was revealed that the textural and structural properties of the modified catalysts remained almost unaffected after treatment, whereas, increasing the  $\text{Cu}:\text{NH}_3$  ratio to 1:4 resulted in higher reducibility and gave rise to  $\text{Cu}^+$  and surface lattice oxygen species, leading, thus, to improved catalytic performance [278]. As shown in Figure 20, close relationships between the half-conversion temperature ( $T_{50}$ ) and the main Raman peak shift or the concentration of  $\text{Ce}^{3+}$  and oxygen vacancies were observed [278].

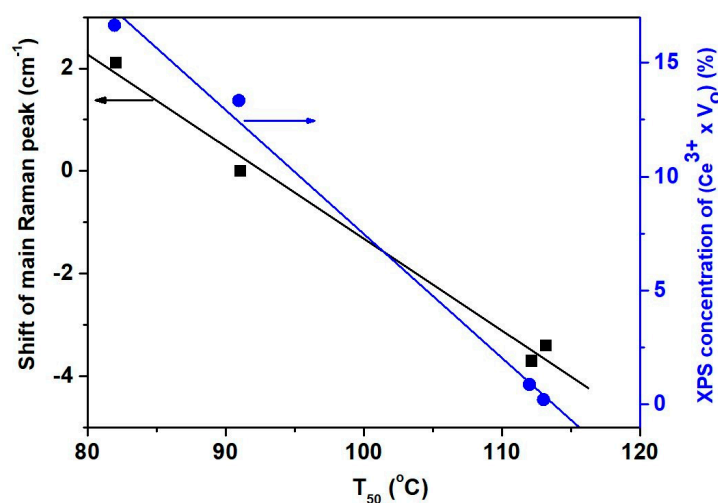


**Figure 20.**  $T_{50}$  vs. (i) shift of the main peak ( $\text{F}_{2g}$  Raman vibration mode) of fluorite  $\text{CeO}_2$  and (ii) surface concentration of  $\text{Ce}^{3+}$  and oxygen vacancies determined via XPS analysis. Adapted from Reference [278]. Copyright© 2018, John Wiley and Sons.

Another adjusted parameter that can exert a profound influence on the catalytic performance is the electronic promotion mainly induced by alkali modifiers, as it may affect the chemisorption ability of active sites, as well as the copper-ceria interactions. In that context, it was found that the presence of  $K^+$  ions in  $CuO_x/CeO_2$  catalysts has a beneficial effect on CO-PROX process in the presence of both  $CO_2$  and  $H_2O$ , since a proper  $K^+$  content was proved to alleviate the  $CO_2$  and  $H_2O$  adsorption on the reaction sites and thus, enhancing the catalytic performance [279]. Potassium has also been found to stabilize  $Cu^+$  active species by affecting Cu-Ce interactions [280].

An additional engineering approach towards enhancing the CO-PROX reactivity of  $CuO_x/CeO_2$  oxides involves the employment of chemical substances of specific architecture and textural properties, such as the carbon-based materials (rGO, CNTs, etc.). These materials favor the dispersion of copper and ceria, while affecting the reducibility and the population of oxygen vacancies, thus, resulting in enhanced catalytic performance at low-temperatures [256,281–284]. As for example, the introduction of rGO resulted in abundant  $Ce^{3+}$  species and oxygen vacancies, offering high catalytic activity at temperatures below 135 °C and good resistance to  $CO_2$  and  $H_2O$  [283].

Interestingly, by combining electronic (alkali promotion) and chemical modification (carbon nanotubes), highly active multifunctional composites can be obtained. In copper-ceria catalysts supported on carbon nanotubes (CNTs) with a specific alkali/Cu atomic ratio, i.e., 0.68, the nature of the alkali metal (Li, Na, K, Cs) has been shown to affect the dispersion of ceria over CNTs and the copper-ceria interaction [261]. K-promoted  $CuO_x/CeO_2$  oxides combined with CNTs exhibited high catalytic activity ( $T_{50} \approx 109$  °C as compared to 175 °C of un-promoted catalyst), attributed to the K-induced modification on redox/electronic properties [261].

#### 3.4. Water-Gas Shift Reaction (WGSR)

The water-gas shift reaction (WGSR) plays a key role in the production of pure hydrogen, through the chemical equilibrium:  $CO + H_2O \leftrightarrow CO_2 + H_2$ . Among the different catalytic systems, copper-ceria oxides have gained particular attention, due to their low cost and adequate catalytic performance. Moreover, significant efforts have been put forward towards optimizing the low-temperature WGS activity by means of the above discussed methodologies. Regarding  $CuO_x/CeO_2$  catalyzed WGSR, two main reaction mechanisms have been proposed, namely, the redox and the associative mechanism. The first one involves the oxidation of adsorbed CO by oxygen originated by  $H_2O$  dissociation. The second one involves the reaction of CO with surface hydroxyl groups towards the formation and subsequent decomposition of various intermediate species, such as formates [161,285].

A thorough study concerning the nature of active species and the role of copper-ceria interface for the low-temperature WGSR has been recently performed by Chen et al. [285]. It was revealed that the activity of copper-ceria catalysts is intrinsically related with the  $Cu^+$  species present at the interfacial perimeter, with the CO molecule being adsorbed on the  $Cu^+$  sites, while water being dissociatively activated on the oxygen vacancies of ceria [285,286]. In a similar manner, Flytzani-Stephanopoulos and co-workers [287] have earlier shown that strongly bound Cu-[O<sub>x</sub>]-Ce species, probably associated with oxygen vacancies of ceria, are the active species for the low-temperature WGSR, whereas, the weakly bound copper oxide clusters and  $CuO_x$  nanoparticles act as spectators.

Although the distinct role of copper and ceria and their interaction is not well determined, it is generally accepted that the activation of  $H_2O$ , linked to copper-ceria interface and oxygen vacancies, is the rate-determining step [285]. Therefore, particular attention has been paid to modulate the interfacial reactivity via the above discussed adjusting approaches. Indicative studies towards modulating the WGSR performance are summarized in Table 4, and further discussed below.

**Table 4.** Indicative studies towards adjusting the WGS performance of CuO-CeO<sub>2</sub> oxides.

Reaction Conditions	Adjusted Parameter (Employed Method)	Optimum System	Maximum CO Conversion	Reference
10.0% CO + 12.0% CO <sub>2</sub> + 60.0% H <sub>2</sub> ; vapor:gas = 1:1; WHSV = 3000 mL g <sup>-1</sup> h <sup>-1</sup>	size/structure (precipitation)	20 wt.% Cu/CeO <sub>2</sub>	91.7% at 200 °C	[206,207]
2.0% CO + 10.0% H <sub>2</sub> O; WHSV = 42,000 mL g <sup>-1</sup> h <sup>-1</sup>	size/structure (bulk-nano interfaces by aerosol-spray method)	inverse CeO <sub>2</sub> /Cu CeO <sub>2</sub> (2–3 nm)	100% at 350 °C	[288]
1.0% CO + 3.0% H <sub>2</sub> O; WHSV = 200,000 mL g <sup>-1</sup> h <sup>-1</sup>	shape (microemulsion method)	5.0 wt.% Cu/CeO <sub>2</sub> -nanospheres	64% at 350 °C	[136]
10.0% CO + 5.0% CO <sub>2</sub> + 10.0% H <sub>2</sub> O + 7.5% H <sub>2</sub> ; WHSV = 60,000 mL g <sup>-1</sup> h <sup>-1</sup>	shape (precipitation method)	Cu/CeO <sub>2</sub> -nanoparticles	49% at 400 °C	[119]
3.5% CO + 3.5% CO <sub>2</sub> + 25.0% H <sub>2</sub> + 29.0% H <sub>2</sub> O; GHSV = 6000 h <sup>-1</sup>	shape (hydrothermal method)	10 wt.% Cu/CeO <sub>2</sub> -octahedrons	91.3% at 300 °C	[159]
10.0% CO + 5.0% CO <sub>2</sub> + 5.0% H <sub>2</sub> ; vapor:gas = 1:1; GHSV = 6000 h <sup>-1</sup>	electronic/chemical state (doping with cobalt by nanocasting)	Cu-Co-CeO <sub>2</sub> (weight ratio of Cu:Co:Ce = 1:2:7)	95% at 300 °C	[289]
10.0% CO + 12.0% CO <sub>2</sub> + 60.0% H <sub>2</sub> ; vapor:gas = 1:1; WHSV = 2337 mL g <sup>-1</sup> h <sup>-1</sup>	electronic/chemical state (doping with yttrium by co-precipitation)	Y-doped Cu/CeO <sub>2</sub> 25 wt.% CuO, 2 wt.% Y <sub>2</sub> O <sub>3</sub>	93.4% at 250 °C	[209]
15.0% CO + 6.0% CO <sub>2</sub> + 55.0% H <sub>2</sub> ; vapor:gas = 1:1; GHSV = 4500 h <sup>-1</sup>	pretreatment (with 20 CO <sub>2</sub> /2H <sub>2</sub> followed by calcination in O <sub>2</sub> )	10 wt.% Cu/CeO <sub>2</sub>	86% at 350 °C	[290]

WHSV: Weight hourly space velocity [=] mL g<sup>-1</sup> h<sup>-1</sup>. GHSV: Gas hourly space velocity [=] h<sup>-1</sup>.

The preparation method can affect various characteristics, such as the specific surface area, the total pore volume, the dispersion of the active phase or the crystallite size [206,291]. For instance, copper-ceria catalyst prepared by a hard template method showed higher WGS activity as compared to the one prepared by co-precipitation (62 vs. 54% CO conversion at 450 °C), due to its larger surface area and higher CuO<sub>x</sub> dispersion, while they both exhibited a similar amount of acidic surface sites [291]. Among CuO<sub>x</sub>/CeO<sub>2</sub> catalysts synthesized by different precipitation methods, the catalysts prepared by stepwise precipitation showed the highest CO conversion, due to their higher reducibility and oxygen defects [208]. Precipitation was also found to give catalysts with higher WGS activity, namely, 91.7% CO conversion at 200 °C, in comparison with the hydrothermal (82%) or sol-gel methods (64.5%), due to their abundance in oxygen vacancies, associated with the small CuO<sub>x</sub> crystals and large pore volume [206].

The precipitating agent used could also exert a significant impact on the physicochemical properties of CuO<sub>x</sub>/CeO<sub>2</sub> catalysts, with the great implication in the catalytic behavior [207,292]. By employing ammonia water instead of ammonium and potassium carbonate, the WGS activity is notably enhanced (91.7% CO conversion at 200 °C in contrast to 78.3% and 46.2%, respectively), due to the better dispersion of copper species and the stronger copper-ceria interactions [207]. Moreover, the copper precursor compound (nitrate or ammonium ions) and the preparation temperature can notably affect the WGS activity [292].

Recently, it was found that the dispersion of differently formed copper structures (particles, clusters, layers) on ceria of rod-like morphology is dependent on copper loading, with low copper loadings (1–15 mol.%) exhibiting monolayers and/or bilayers of copper, while a further increase in copper loading up to 28 mol.% results in faceted copper particles and multi-layers of copper [286]. At copper loadings up to 15 mol.%, a linear relationship between the CO conversion and the copper content was observed (Figure 21), indicating that the number of the active interfacial sites (Cu<sup>+</sup>-V<sub>o</sub>-Ce<sup>3+</sup>) is significantly increased along with Cu content up to 15 mol.% [286].

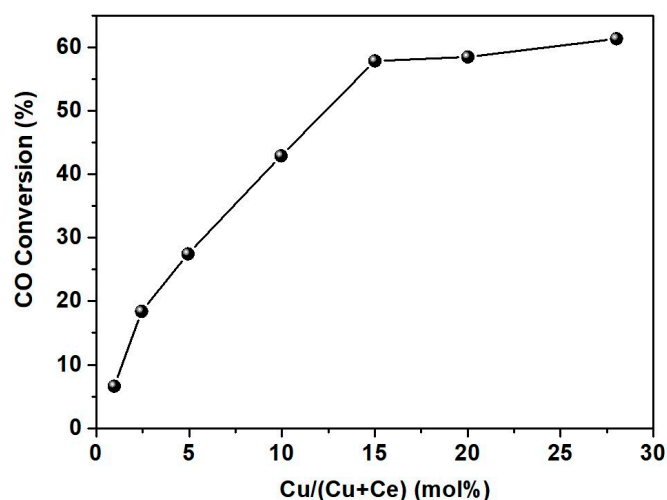


**Figure 21.** Low-temperature WGS reaction over the Cu/CeO<sub>2</sub> catalysts. CO conversion as a function of the copper content in the respect catalysts. Reaction conditions: 1.0 vol.% CO/3.0 vol.% H<sub>2</sub>O/He, 40,000 h<sup>-1</sup>, 200 °C. Adapted from Reference [286]. Copyright© 2019, Elsevier.

The morphological features of both copper and ceria counterparts notably affect the WGS activity. In a comprehensive study by Zhang et al. [293], it was reported that Cu cubes exhibit high WGS activity in contrast to Cu octahedra with the Cu–Cu suboxide (Cu<sub>x</sub>O, x ≥ 10) interface of Cu(100) surface being the active sites. In a similar manner, it was shown that ceria nanoshapes (rods, cubes, octahedra) exhibit different behavior during interaction with CO and H<sub>2</sub>O, due to their diverse defect chemistry [294]. Upon CO exposure, ceria nanocubes, exposing {100} planes, favor the formation of oxygen defects at the expense of the existing anti-Frenkel defects, while in nanorods and nanooctahedra (exposing mainly {111} planes) both types of defects are formed [294]. By combining Raman and FTIR results, it was revealed that H<sub>2</sub>-reduced ceria rods and octahedra could be further reduced in

CO, resulting in the formation of both defects. In contrast, cubes cannot be further reduced by CO; thus, oxygen is available to form carbonates and bicarbonates by converting Frenkel defects to oxygen vacancies [294]. These findings clearly revealed the key role of both copper and ceria nanoshape on the defect chemistry of individual counterparts. It should be noted, however, that in the binary copper-ceria system, where multifaceted interactions are taking place, the relationships between shape effects and catalytic activity can be rather complex, leading to inconsistent conclusions [119,136,159].

Very recently, Yan et al. [288] reported on a novel structural design approach towards optimizing the WGS activity of  $\text{CuO}_x/\text{CeO}_2$  system. In particular, inverse copper-ceria catalysts of high efficiency were developed through the fabrication of highly stable bulk-nano interfaces under reaction conditions. Nano-sized ceria particles (2–3 nm) were stabilized on bulk copper resulting in abundant ceria-copper interfaces [288]. This inverse catalyst showed outstanding WGS conversion ( $T_{100} = 350\text{ }^\circ\text{C}$ ), due to the high amount of interfacial sites and the strong copper-ceria interaction, which facilitated the dissociation of water and the oxidation of CO [288].

The doping approach has also been employed to enhance the WGS activity of  $\text{CuO}_x/\text{CeO}_2$  system [209,295]. For instance, copper-ceria catalysts doped with 2 wt.% yttrium have shown excellent WGS activity and high thermal stability, as yttrium favored the oxygen vacancy formation on ceria [209]. Recently, Wang et al. [295] performed DFT calculations in order to theoretically investigate the alkali effect on the WGS activity of Cu(111) and Cu(110) surfaces. It was found that potassium enhances the WGS activity as it favors the dissociation of  $\text{H}_2\text{O}$  and induces stronger promotion on the (111) surface. With regard to other alkali metals (Na, Rb, Cs), the promoting effect on the dissociation of water differentiates with their electronegativities which induce changes in the work function, i.e., the lower the work function, the stronger the promoting effect of the alkali [295].

Finally, the WGS activity and the sintering resistance of the  $\text{CuO}_x/\text{CeO}_2$  catalysts can be further enhanced by improving the metal-support interactions through appropriate pretreatment protocols [290,296]. As for example, the treatment of  $\text{CuO}_x/\text{CeO}_2$  catalyst in a gas mixture of  $20\text{CO}_2/2\text{H}_2$  led to highly active catalysts, due to the electron enrichment of copper atoms via electronic metal-support interactions [290]. Moreover, ceria pretreatment in different atmosphere (air, vacuum or  $\text{H}_2$ ) affected the WGS performance of  $\text{CuO}_x/\text{CeO}_2$  catalysts, with the  $\text{H}_2$ -pretreated samples exhibiting the highest conversion performance, due to the strong synergism between the two oxide phases, the small  $\text{CuO}_x$  particle size, and the high concentration in oxygen vacancies [296].

### 3.5. $\text{CO}_2$ Hydrogenation

The hydrogenation of carbon dioxide to value-added chemicals, such as methanol, has received considerable attention, in terms of environmental protection and sustainable energy. The significant role of copper-ceria interfacial sites in the  $\text{CO}_2$  hydrogenation process has been confirmed by both theoretical and experimental studies [40,297,298]. In particular, metal-oxide interface plays a key role in  $\text{CO}_2$  hydrogenation process, as it could provide the active sites for reactants adsorption, while these interfacial sites may stabilize the key intermediates [299]. In view of this fact, copper-ceria catalysts have shown higher selectivity in methanol than their zirconia-supported counterparts, as the copper-ceria interface favored the dispersion of copper and the oxygen vacancy formation, while the interaction between copper and ceria led to a decrease in copper particle size [300]. The interfaces between the defective  $\text{CeO}_{2-x}$  and the highly dispersed  $\text{Cu}^+/\text{Cu}^0$  species are considered the active sites for methanol synthesis in the case of  $\text{CuO}_x/\text{CeO}_2$  system [301]. Furthermore, the different metal-support interactions between the two catalysts resulted in different reaction intermediates, namely, carbonates for the  $\text{CuO}_x/\text{CeO}_2$  catalysts and bicarbonates for the zirconia-supported ones, thus, resulting in different selectivity, with the copper-zirconia composites being highly selective in CO [300].

In view of the above aspects, the fine-tuning of the metal-support interface could lead to highly active and selective catalysts. Indicative studies towards adjusting the  $\text{CO}_2$  conversion to methanol under similar reaction conditions are summarized in Table 5, and further discussed below.

**Table 5.** Indicative studies towards adjusting the CO<sub>2</sub> conversion to methanol of CuO<sub>x</sub>/CeO<sub>2</sub> oxides.

Reaction Conditions	Adjusted Parameter (Employed Method)	Optimum System	CO <sub>2</sub> Conversion (Methanol Rate or Selectivity) at 260 °C	Reference
CO <sub>2</sub> :H <sub>2</sub> = 1:3; P = 3.0 MPa; GHSV = 1200 h <sup>-1</sup>	electronic/chemical state (doping with zinc and dispersion in SBA-15 by incipient wetness impregnation)	Cu <sub>0.5</sub> Zn <sub>0.4</sub> Ce <sub>0.1</sub> /SBA-15	6.5% (33.6 mg g <sup>-1</sup> h <sup>-1</sup> )	[302]
CO <sub>2</sub> :H <sub>2</sub> = 1:3; P = 3.0 MPa; WHSV = 14,400 mL g <sup>-1</sup> h <sup>-1</sup>	electronic/chemical state (doping with alumina by co-precipitation)	60 wt.% Cu/AlCeO	17.0% (11.9 mmol g <sup>-1</sup> h <sup>-1</sup> )	[303]
CO <sub>2</sub> :H <sub>2</sub> = 1:3; P = 3.0 MPa; GHSV = 6000 h <sup>-1</sup>	electronic/chemical state/shape (doping with Ni-Cu by impregnation)	CuNi <sub>2</sub> /CeO <sub>2</sub> -nanotubes Ni/(Cu+Ni) = 2/3	17.8% (18.1 mmol g <sup>-1</sup> h <sup>-1</sup> )	[304]
CO <sub>2</sub> :H <sub>2</sub> = 1:3; P = 3.0 MPa; GHSV = 6000 h <sup>-1</sup>	electronic/chemical state/shape (doping with Ni-Cu by impregnation)	CuNi <sub>2</sub> /CeO <sub>2</sub> -nanorods 10 wt.% Cu and Ni	18.35% (73.33%)	[305]
CO <sub>2</sub> :H <sub>2</sub> = 1:3; P = 2.0 MPa; WHSV = 3000 mL g <sup>-1</sup> h <sup>-1</sup>	shape (hydrothermal method)	5.0 wt.% Cu/CeO <sub>2</sub> -nanorods	2.5% (71.0%)	[131]

WHSV: Weight hourly space velocity [=] mL g<sup>-1</sup> h<sup>-1</sup>; GHSV: Gas hourly space velocity [=] h<sup>-1</sup>.

The activity and selectivity of the  $\text{CuO}_x/\text{CeO}_2$  catalysts for methanol synthesis are greatly affected by the support morphology. Copper-ceria nanorods exposing {100} and {110} crystal planes exhibited the highest methanol yield (Table 5) as compared to nanocubes and nanoparticles, due to the strong interaction between the two oxide phases and the high copper dispersion [131]. Copper-ceria nanorods were also found to be more active than nanocubes, while exhibiting similar conversion performance with the nanoparticles, for carbonate (diethyl) hydrogenation [147].

In a similar manner,  $\text{CuO}_x/\text{CeO}_2$  catalysts led, mainly, to the production of CO at atmospheric pressures through the RWGS reaction, with the nanorod-shaped catalyst exhibiting higher  $\text{CO}_2$  conversion (~50% at 450 °C) as compared to nanospheres (~40% at 450 °C), revealing the structure dependence of the RWGS [137]. The active intermediates are preferably formed on the {110} ceria exposed surface of the rod-like morphology, resulting in high catalytic performance [137].

Copper-ceria nanorods of various copper loadings were also investigated in the hydrogenation of carbonate to methanol, with the catalysts of ca. 20 wt.% Cu content exhibiting superior catalytic performance [306]. The copper content can significantly affect the mole fraction of  $\text{Ce}^{3+}$  and  $\text{Cu}^+$  species (Figure 22), and in turn, the methanol yield [306].

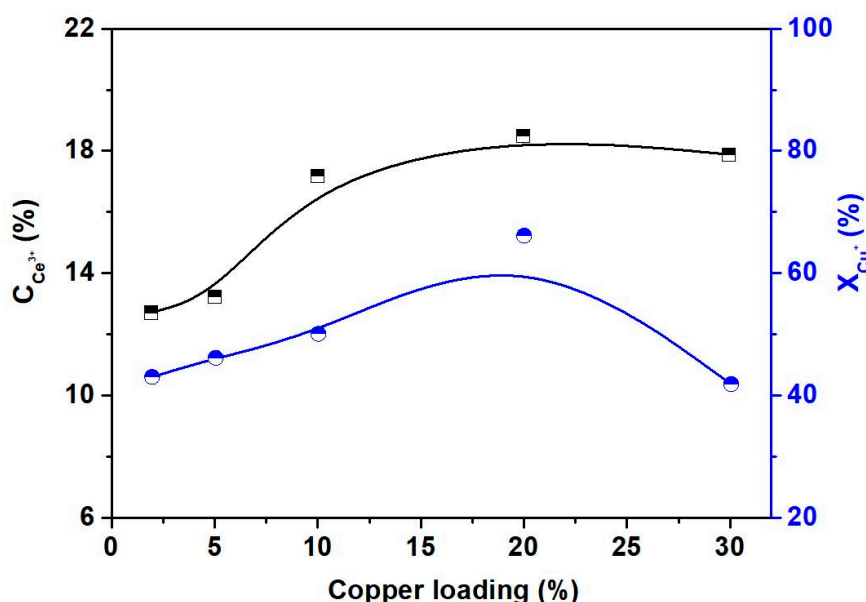


**Figure 22.** Mole ratio of  $\text{Ce}^{3+}$  and  $\text{Cu}^+$  over the reduced  $\text{Cu}/\text{CeO}_2$  catalysts as a function of Cu content. Adapted from Reference [306]. Copyright© 2018, John Wiley and Sons.

In addition, a space-confined synthetic approach was applied for the synthesis of highly dispersed copper-ceria catalysts for RWGS, offering 100% CO selectivity at 300 °C and ambient pressure [307]. The enhanced catalytic performance was ascribed to the abundance in interfaces formed among the highly dispersed copper nanoparticles and the  $\text{Ce}^{3+}$  species, thus, favoring  $\text{H}_2$  spillover [307].

The controlled synthesis of multicomponent systems could also be an effective approach for highly active and selective hydrogenation catalysts (e.g., [302–305,308]). For instance, the ternary composite consisting of Cu, ZnO,  $\text{CeO}_x$ , supported on SBA-15 exhibited high catalytic activity for methanol synthesis (Table 5), due to the peculiar synergistic effects between the different counterparts [302]. Copper was considered to be the active site for hydrogen activation, while ZnO and  $\text{CeO}_x$  oxides facilitated the  $\text{CO}_2$  adsorption and hydrogen spillover on the interfacial sites [302]. In a similar manner, the introduction of alumina to ceria carrier ( $\text{Cu}/\text{AlCe}$ ) led to highly active composites (Table 5), mainly ascribed to the high copper dispersion [303]. Interestingly, highly active and selective  $\text{CO}_2$  hydrogenation catalysts can be obtained by co-adjusting the composition, structure and shape, in line with the fine-tuning methodology herein proposed (Figures 2 and 3). In this perspective, bimetallic

composites (Cu-Ni) incorporated into ceria nanoparticles of specific morphology (e.g., nanotubes, nanorods) could lead to highly active composites for the CO<sub>2</sub> hydrogenation to methanol (Table 5). The enhanced catalytic performance of Cu-Ni/CeO<sub>2</sub> nanoshaped catalysts was mainly interpreted on the basis of the synergistic interaction between Cu and Ni as well as of that between the ceria carrier and Cu-Ni alloy [304,305]. Similarly, the bimetallic Cu-Fe/CeO<sub>2</sub> catalyst has shown enhanced stability in the high-temperature RWGS due mainly to the fact that iron oxide clusters (FeO<sub>x</sub>) highly dispersed over ceria act as textural promoters [308]. Finally, copper nanocrystals encapsulated in Zr-based MOFs demonstrated high activity and selectivity for CO<sub>2</sub> hydrogenation to methanol, outperforming the benchmark Cu/ZnO/Al<sub>2</sub>O<sub>3</sub> catalyst [197].

#### 4. Outlook and Challenges

In the present review, the copper-ceria binary system has been employed as a reference system to reveal the different approaches that can be followed to modulate the local surface chemistry, and in turn, the catalytic performance of metal oxides (MOs), by means of size, shape and electronic/chemical functionalization. More importantly, the fine-tuning of the above-mentioned parameters can affect not only the reactivity of metal sites in its own right, but also the interfacial activity (e.g., through the formation of oxygen vacancies, facilitation of redox interplay between the different counterparts, etc.) offering a synergistic contribution towards the development of NMs-free highly active and selective composites for several energy and environmental applications.

For instance, the employment of appropriate synthetic routes, such as the hydrothermal method, leads to the development of nanoparticles with specific morphologies, exposing distinct crystal facets of different coordination environments, with great implications in catalysis. Moreover, particles size/shape engineering strongly affects the interfacial reactivity through both geometric and electronic interactions, offering metal oxide systems with the desired properties. In addition, special pretreatment protocols or activation procedures can notably affect the metal dispersion and the population of oxygen defects, with great consequences in the catalytic efficiency. In view of the above, the fine tuning of metal oxides by combining bulk and nano effects or by adjusting the coordination environment could lead to highly efficient catalysts.

Besides the modulation of local surface chemistry by means of size and shape engineering, the electronic/chemical modification (e.g., alkali promotion, incorporation of rGO or g-C<sub>3</sub>N<sub>4</sub>, employment of MOFs) can be adopted as an additional functionalization tool to regulate the electronic environment and the oxygen exchange kinetics of MOs.

In view of the above aspects, highly active composites, with a comparable or even better performance than that of NMs, have been developed for various processes, such as CO oxidation, N<sub>2</sub>O decomposition, preferential oxidation of CO, among others. As for example, the combination of precipitation method with alkali promotion can lead to highly active and oxygen-tolerant CuO<sub>x</sub>/CeO<sub>2</sub> catalysts for N<sub>2</sub>O decomposition. On the other hand, the modulation of ceria support morphology (nanorods) by the hydrothermal method resulted in CuO<sub>x</sub>/CeO<sub>2</sub> composites with superior CO oxidation performance, even better to that of Pt-based catalysts. More importantly, the co-adjustment of different parameters (e.g., the shape of individual counterparts along with the electronic state of metal entities) could lead not only to distinct reactivity of each counterpart, but also to different synergistic interactions, offering mixed metal oxides of unique features. Hence, metal oxides appropriately adjusted by means of suitable synthetic and electronic/chemical modification routes could provide the materials platform for real-life energy and environmental applications.

Another approach towards the fine-tuning of metal oxides could be the employment of computational studies (e.g., DFT calculations) prior to the synthesis of the catalysts, providing, thus, the required feedback that would lead to the focused functionalization of specific parameters. This combinatorial theoretical and experimental approach could result in specific composites with predefined characteristics, while it would save precious time during experimental trials.

Last, but not least, the conclusions drawn from the present survey can provide the design principles for the development of low-loading NMs-based catalysts, paving the way for the decrease of noble metals content in energy and environmental applications in which their use is inevitable. In any case, the fundamental understanding of structure-property relationships is a prerequisite factor towards the rational design of efficient and inexpensive catalytic composites.

**Author Contributions:** M.L. contributed to paper writing; M.K. contributed to the conception, design and writing of the paper; All authors contributed to the discussion, read and approved the final version of the manuscript. All authors have read and agreed to the published version of the manuscript.

**Funding:** This research has been co-financed by the European Union and Greek national funds through the Operational Program Competitiveness, Entrepreneurship and Innovation, under the call RESEARCH-CREATE-INNOVATE (project code: T1EDK-00094).

**Acknowledgments:** The authors would like to express their sincere gratitude to the anonymous reviewers for their constructive remarks that greatly contributed to improving the content and the scientific impact of this review article. The authors also would like to thank the editors for their efforts during the review process.

**Conflicts of Interest:** The authors declare no conflict of interest.

## References

1. Yao, X.; Tang, C.; Gao, F.; Dong, L. Research progress on the catalytic elimination of atmospheric molecular contaminants over supported metal-oxide catalysts. *Catal. Sci. Technol.* **2014**, *4*, 2814–2829. [[CrossRef](#)]
2. Melchionna, M.; Fornasiero, P. The role of ceria-based nanostructured materials in energy applications. *Mater. Today* **2014**, *17*, 349–357. [[CrossRef](#)]
3. Fang, Y.; Guo, Y. Copper-based non-precious metal heterogeneous catalysts for environmental remediation. *Chin. J. Catal.* **2018**, *39*, 566–582. [[CrossRef](#)]
4. Yuan, C.; Wu, H.B.; Xie, Y.; Lou, X.W. Mixed Transition-Metal Oxides: Design, Synthesis, and Energy-Related Applications. *Angew. Chem. Int. Ed.* **2014**, *53*, 1488–1504. [[CrossRef](#)]
5. Montini, T.; Melchionna, M.; Monai, M.; Fornasiero, P. Fundamentals and Catalytic Applications of CeO<sub>2</sub>-Based Materials. *Chem. Rev.* **2016**, *116*, 5987–6041. [[CrossRef](#)] [[PubMed](#)]
6. Wu, K.; Sun, L.-D.; Yan, C.-H. Recent Progress in Well-Controlled Synthesis of Ceria-Based Nanocatalysts towards Enhanced Catalytic Performance. *Adv. Energy Mater.* **2016**, *6*, 1600501. [[CrossRef](#)]
7. Rodriguez, J.A.; Liu, P.; Graciani, J.; Senanayake, S.D.; Grinter, D.C.; Stacchiola, D.; Hrbek, J.; Fernández-Sanz, J. Inverse Oxide/Metal Catalysts in Fundamental Studies and Practical Applications: A Perspective of Recent Developments. *J. Phys. Chem. Lett.* **2016**, *7*, 2627–2639. [[CrossRef](#)] [[PubMed](#)]
8. Spezzati, G.; Benavidez, A.D.; DeLaRiva, A.T.; Su, Y.; Hofmann, J.P.; Asahina, S.; Olivier, E.J.; Neethling, J.H.; Miller, J.T.; Datye, A.K.; et al. CO oxidation by Pd supported on CeO<sub>2</sub> (100) and CeO<sub>2</sub> (111) facets. *Appl. Catal. B Environ.* **2019**, *243*, 36–46. [[CrossRef](#)]
9. Morfin, F.; Nguyen, T.-S.; Rousset, J.-L.; Piccolo, L. Synergy between hydrogen and ceria in Pt-catalyzed CO oxidation: An investigation on Pt–CeO<sub>2</sub> catalysts synthesized by solution combustion. *Appl. Catal. B Environ.* **2016**, *197*, 2–13. [[CrossRef](#)]
10. Gatla, S.; Aubert, D.; Flaud, V.; Grosjean, R.; Lunkenbein, T.; Mathon, O.; Pascarelli, S.; Kaper, H. Facile synthesis of high-surface area platinum-doped ceria for low temperature CO oxidation. *Catal. Today* **2019**, *333*, 105–112. [[CrossRef](#)]
11. Gatla, S.; Aubert, D.; Agostini, G.; Mathon, O.; Pascarelli, S.; Lunkenbein, T.; Willinger, M.G.; Kaper, H. Room-Temperature CO Oxidation Catalyst: Low-Temperature Metal-Support Interaction between Platinum Nanoparticles and Nanosized Ceria. *ACS Catal.* **2016**, *6*, 6151–6155. [[CrossRef](#)]
12. Parres-Esclapez, S.; Such-Basañez, I.; Illán-Gómez, M.J.; Salinas-Martínez de Lecea, C.; Bueno-López, A. Study by isotopic gases and in situ spectroscopies (DRIFTS, XPS and Raman) of the N<sub>2</sub>O decomposition mechanism on Rh/CeO<sub>2</sub> and Rh/γ-Al<sub>2</sub>O<sub>3</sub> catalysts. *J. Catal.* **2010**, *276*, 390–401. [[CrossRef](#)]
13. Zhu, H.; Li, Y.; Zheng, X. In-situ DRIFTS study of CeO<sub>2</sub> supported Rh catalysts for N<sub>2</sub>O decomposition. *Appl. Catal. A Gen.* **2019**, *571*, 89–95. [[CrossRef](#)]
14. Zheng, J.; Meyer, S.; Köhler, K. Abatement of nitrous oxide by ruthenium catalysts: Influence of the support. *Appl. Catal. A Gen.* **2015**, *505*, 44–51. [[CrossRef](#)]

15. Pachatouridou, E.; Papista, E.; Iliopoulou, E.F.; Delimitis, A.; Goula, G.; Yentekakis, I.V.; Marnellos, G.E.; Konsolakis, M. Nitrous oxide decomposition over Al<sub>2</sub>O<sub>3</sub> supported noble metals (Pt, Pd, Ir): Effect of metal loading and feed composition. *J. Environ. Chem. Eng.* **2015**, *3*, 815–821. [[CrossRef](#)]
16. Pachatouridou, E.; Papista, E.; Delimitis, A.; Vasiliades, M.A.; Efstathiou, A.M.; Amiridis, M.D.; Alexeev, O.S.; Bloom, D.; Marnellos, G.E.; Konsolakis, M.; et al. N<sub>2</sub>O decomposition over ceria-promoted Ir/Al<sub>2</sub>O<sub>3</sub> catalysts: The role of ceria. *Appl. Catal. B Environ.* **2016**, *187*, 259–268. [[CrossRef](#)]
17. Carabineiro, S.A.C.; Papista, E.; Marnellos, G.E.; Tavares, P.B.; Maldonado-Hódar, F.J.; Konsolakis, M. Catalytic decomposition of N<sub>2</sub>O on inorganic oxides: Effect of doping with Au nanoparticles. *Mol. Catal.* **2017**, *436*, 78–89. [[CrossRef](#)]
18. Vecchiotti, J.; Bonivardi, A.; Xu, W.; Stacchiola, D.; Delgado, J.J.; Calatayud, M.; Collins, S.E. Understanding the Role of Oxygen Vacancies in the Water Gas Shift Reaction on Ceria-Supported Platinum Catalysts. *ACS Catal.* **2014**, *4*, 2088–2096. [[CrossRef](#)]
19. Pierre, D.; Deng, W.; Flytzani-Stephanopoulos, M. The Importance of Strongly Bound Pt-CeO<sub>x</sub> Species for the Water-gas Shift Reaction: Catalyst Activity and Stability Evaluation. *Top. Catal.* **2007**, *46*, 363–373. [[CrossRef](#)]
20. Mei, Z.; Li, Y.; Fan, M.; Zhao, L.; Zhao, J. Effect of the interactions between Pt species and ceria on Pt/ceria catalysts for water gas shift: The XPS studies. *Chem. Eng. J.* **2015**, *259*, 293–302. [[CrossRef](#)]
21. Ting, K.W.; Toyao, T.; Siddiki, S.M.A.H.; Shimizu, K.-I. Low-Temperature Hydrogenation of CO<sub>2</sub> to Methanol over Heterogeneous TiO<sub>2</sub>-Supported Re Catalysts. *ACS Catal.* **2019**, *9*, 3685–3693. [[CrossRef](#)]
22. Wang, F.; He, S.; Chen, H.; Wang, B.; Zheng, L.; Wei, M.; Evans, D.G.; Duan, X. Active Site Dependent Reaction Mechanism over Ru/CeO<sub>2</sub> Catalyst toward CO<sub>2</sub> Methanation. *J. Am. Chem. Soc.* **2016**, *138*, 6298–6305. [[CrossRef](#)] [[PubMed](#)]
23. Sakpal, T.; Lefferts, L. Structure-dependent activity of CeO<sub>2</sub> supported Ru catalysts for CO<sub>2</sub> methanation. *J. Catal.* **2018**, *367*, 171–180. [[CrossRef](#)]
24. Vourros, A.; Garagounis, I.; Kyriakou, V.; Carabineiro, S.A.C.; Maldonado-Hódar, F.J.; Marnellos, G.E.; Konsolakis, M. Carbon dioxide hydrogenation over supported Au nanoparticles: Effect of the support. *J. CO<sub>2</sub> Util.* **2017**, *19*, 247–256. [[CrossRef](#)]
25. Kyriakou, V.; Vourros, A.; Garagounis, I.; Carabineiro, S.A.C.; Maldonado-Hódar, F.J.; Marnellos, G.E.; Konsolakis, M. Highly active and stable TiO<sub>2</sub>-supported Au nanoparticles for CO<sub>2</sub> reduction. *Catal. Commun.* **2017**, *98*, 52–56. [[CrossRef](#)]
26. Zhou, Y.; Wang, Z.; Liu, C. Perspective on CO oxidation over Pd-based catalysts. *Catal. Sci. Technol.* **2015**, *5*, 69–81. [[CrossRef](#)]
27. Carter, J.H.; Hutchings, G.J. Recent Advances in the Gold-Catalysed Low-Temperature Water–Gas Shift Reaction. *Catalysts* **2018**, *8*, 627. [[CrossRef](#)]
28. Konsolakis, M.; Carabineiro, S.A.C.; Marnellos, G.E.; Asad, M.F.; Soares, O.S.G.P.; Pereira, M.F.R.; Órfão, J.J.M.; Figueiredo, J.L. Effect of cobalt loading on the solid state properties and ethyl acetate oxidation performance of cobalt-cerium mixed oxides. *J. Colloid Interface Sci.* **2017**, *496*, 141–149. [[CrossRef](#)]
29. Konsolakis, M.; Carabineiro, S.A.C.; Marnellos, G.E.; Asad, M.F.; Soares, O.S.G.P.; Pereira, M.F.R.; Órfão, J.J.M.; Figueiredo, J.L. Volatile organic compounds abatement over copper-based catalysts: Effect of support. *Inorganica Chim. Acta* **2017**, *455*, 473–482. [[CrossRef](#)]
30. Konsolakis, M.; Carabineiro, S.A.C.; Tavares, P.B.; Figueiredo, J.L. Redox properties and VOC oxidation activity of Cu catalysts supported on Ce<sub>1-x</sub>Sm<sub>x</sub>O<sub>δ</sub> mixed oxides. *J. Hazard. Mater.* **2013**, *261*, 512–521. [[CrossRef](#)]
31. Konsolakis, M.; Ioakeimidis, Z. Surface/structure functionalization of copper-based catalysts by metal-support and/or metal-metal interactions. *Appl. Surf. Sci.* **2014**, *320*, 244–255. [[CrossRef](#)]
32. Konsolakis, M.; Ioakimidis, Z.; Kraia, T.; Marnellos, G.E. Hydrogen Production by Ethanol Steam Reforming (ESR) over CeO<sub>2</sub> Supported Transition Metal (Fe, Co, Ni, Cu) Catalysts: Insight into the Structure-Activity Relationship. *Catalysts* **2016**, *6*, 39. [[CrossRef](#)]
33. Konsolakis, M.; Sgourakis, M.; Carabineiro, S.A.C. Surface and redox properties of cobalt-ceria binary oxides: On the effect of Co content and pretreatment conditions. *Appl. Surf. Sci.* **2015**, *341*, 48–54. [[CrossRef](#)]
34. Kraia, T.; Kakkidis, N.; Konsolakis, M.; Marnellos, G.E. Hydrogen production by H<sub>2</sub>S decomposition over ceria supported transition metal (Co, Ni, Fe and Cu) catalysts. *Int. J. Hydrogen Energy* **2019**, *44*, 9753–9762. [[CrossRef](#)]

35. Lykaki, M.; Papista, E.; Kaklidis, N.; Carabineiro, S.A.C.; Konsolakis, M. Ceria Nanoparticles' Morphological Effects on the N<sub>2</sub>O Decomposition Performance of Co<sub>3</sub>O<sub>4</sub>/CeO<sub>2</sub> Mixed Oxides. *Catalysts* **2019**, *9*, 233. [[CrossRef](#)]
36. Lykaki, M.; Stefa, S.; Carabineiro, S.A.C.; Pandis, P.K.; Stathopoulos, V.N.; Konsolakis, M. Facet-Dependent Reactivity of Fe<sub>2</sub>O<sub>3</sub>/CeO<sub>2</sub> Nanocomposites: Effect of Ceria Morphology on CO Oxidation. *Catalysts* **2019**, *9*, 371. [[CrossRef](#)]
37. Aneggi, E.; Boaro, M.; Colussi, S.; de Leitenburg, C.; Trovarelli, A. Chapter 289—Ceria-Based Materials in Catalysis: Historical Perspective and Future Trends. *Handb. Phys. Chem. Rare Earths* **2016**, *50*, 209–242. [[CrossRef](#)]
38. Tang, W.-X.; Gao, P.-X. Nanostructured cerium oxide: preparation, characterization, and application in energy and environmental catalysis. *MRS Commun.* **2016**, *6*, 311–329. [[CrossRef](#)]
39. Su, X.; Yang, X.; Zhao, B.; Huang, Y. Designing of highly selective and high-temperature durable RWGS heterogeneous catalysts: recent advances and the future directions. *J. Energy Chem.* **2017**, *26*, 854–867. [[CrossRef](#)]
40. Konsolakis, M. The role of Copper–Ceria interactions in catalysis science: Recent theoretical and experimental advances. *Appl. Catal. B Environ.* **2016**, *198*, 49–66. [[CrossRef](#)]
41. Carabineiro, S.A.C.; Chen, X.; Konsolakis, M.; Psarras, A.C.; Tavares, P.B.; Órfão, J.J.M.; Pereira, M.F.R.; Figueiredo, J.L. Catalytic oxidation of toluene on Ce-Co and La-Co mixed oxides synthesized by exotemplating and evaporation methods. *Catal. Today* **2015**, *244*, 161–171. [[CrossRef](#)]
42. Carabineiro, S.A.C.; Konsolakis, M.; Marnellos, G.E.N.; Asad, M.F.; Soares, O.S.G.P.; Tavares, P.B.; Pereira, M.F.R.; De Melo Órfão, J.J.; Figueiredo, J.L. Ethyl Acetate Abatement on Copper Catalysts Supported on Ceria Doped with Rare Earth Oxides. *Molecules* **2016**, *21*, 644. [[CrossRef](#)]
43. Díez-Ramírez, J.; Sánchez, P.; Kyriakou, V.; Zafeiratos, S.; Marnellos, G.E.; Konsolakis, M.; Dorado, F. Effect of support nature on the cobalt-catalyzed CO<sub>2</sub> hydrogenation. *J. CO<sub>2</sub> Util.* **2017**, *21*, 562–571. [[CrossRef](#)]
44. Zeng, S.; Zhang, W.; Guo, S.; Su, H. Inverse rod-like CeO<sub>2</sub> supported on CuO prepared by hydrothermal method for preferential oxidation of carbon monoxide. *Catal. Commun.* **2012**, *23*, 62–66. [[CrossRef](#)]
45. Rodriguez, J.A.; Liu, P.; Hrbek, J.; Evans, J.; Pérez, M. Water Gas Shift Reaction on Cu and Au Nanoparticles Supported on CeO<sub>2</sub>(111) and ZnO(0001): Intrinsic Activity and Importance of Support Interactions. *Angew. Chem. Int. Ed.* **2007**, *46*, 1329–1332. [[CrossRef](#)] [[PubMed](#)]
46. Ranga Rao, G.; Mishra, B.G. Structural, redox and catalytic chemistry of ceria based materials. *Bull. Catal. Soc. India* **2003**, *2*, 122–134.
47. Rodriguez, J.A.; Grinter, D.C.; Liu, Z.; Palomino, R.M.; Senanayake, S.D. Ceria-based model catalysts: fundamental studies on the importance of the metal-ceria interface in CO oxidation, the water-gas shift, CO<sub>2</sub> hydrogenation, and methane and alcohol reforming. *Chem. Soc. Rev.* **2017**, *46*, 1824–1841. [[CrossRef](#)]
48. Zhang, D.; Du, X.; Shi, L.; Gao, R. Shape-controlled synthesis and catalytic application of ceria nanomaterials. *Dalton Trans.* **2012**, *41*, 14455–14475. [[CrossRef](#)]
49. Dong, L.; Yao, X.; Chen, Y. Interactions among supported copper-based catalyst components and their effects on performance: A review. *Chin. J. Catal.* **2013**, *34*, 851–864. [[CrossRef](#)]
50. Pacchioni, G. Electronic interactions and charge transfers of metal atoms and clusters on oxide surfaces. *Phys. Chem. Chem. Phys.* **2013**, *15*, 1737–1757. [[CrossRef](#)]
51. Zhou, Y.; Li, Y.; Shen, W. Shape Engineering of Oxide Nanoparticles for Heterogeneous Catalysis. *Chem. Asian J.* **2016**, *11*, 1470–1488. [[CrossRef](#)] [[PubMed](#)]
52. Cargnello, M.; Doan-Nguyen, V.V.T.; Gordon, T.R.; Diaz, R.E.; Stach, E.A.; Gorte, R.J.; Fornasiero, P.; Murray, C.B. Control of Metal Nanocrystal Size Reveals Metal-Support Interface Role for Ceria Catalysts. *Science* **2013**, *341*, 771–773. [[CrossRef](#)] [[PubMed](#)]
53. Mistry, H.; Behafarid, F.; Reske, R.; Varela, A.S.; Strasser, P.; Roldan Cuenya, B. Tuning Catalytic Selectivity at the Mesoscale via Interparticle Interactions. *ACS Catal.* **2016**, *6*, 1075–1080. [[CrossRef](#)]
54. Ahmadi, M.; Mistry, H.; Roldan Cuenya, B. Tailoring the Catalytic Properties of Metal Nanoparticles via Support Interactions. *J. Phys. Chem. Lett.* **2016**, *7*, 3519–3533. [[CrossRef](#)] [[PubMed](#)]
55. Hermes, E.D.; Jenness, G.R.; Schmidt, J.R. Decoupling the electronic, geometric and interfacial contributions to support effects in heterogeneous catalysis. *Mol. Simul.* **2015**, *41*, 123–133. [[CrossRef](#)]
56. Uzunoglu, A.; Zhang, H.; Andreescu, S.; Stanciu, L.A. CeO<sub>2</sub>–MO<sub>x</sub> (M: Zr, Ti, Cu) mixed metal oxides with enhanced oxygen storage capacity. *J. Mater. Sci.* **2015**, *50*, 3750–3762. [[CrossRef](#)]

57. Tang, X.; Zhang, B.; Li, Y.; Xu, Y.; Xin, Q.; Shen, W. CuO/CeO<sub>2</sub> catalysts: Redox features and catalytic behaviors. *Appl. Catal. A Gen.* **2005**, *288*, 116–125. [[CrossRef](#)]
58. Lu, Z.; Yang, Z.; He, B.; Castleton, C.; Hermansson, K. Cu-doped ceria: Oxygen vacancy formation made easy. *Chem. Phys. Lett.* **2011**, *510*, 60–66. [[CrossRef](#)]
59. Wang, X.; Rodriguez, J.A.; Hanson, J.C.; Gamarra, D.; Martínez-Arias, A.; Fernández-García, M. Unusual Physical and Chemical Properties of Cu in Ce<sub>1-x</sub>Cu<sub>x</sub>O<sub>2</sub> oxides. *J. Phys. Chem. B* **2005**, *109*, 19595–19603. [[CrossRef](#)]
60. Beckers, J.; Rothenberg, G. Redox properties of doped and supported copper-ceria catalysts. *Dalton Trans.* **2008**, 6573–6578. [[CrossRef](#)]
61. Van Deelen, T.W.; Hernández Mejía, C.; De Jong, K.P. Control of metal-support interactions in heterogeneous catalysts to enhance activity and selectivity. *Nat. Catal.* **2019**, *2*, 955–970. [[CrossRef](#)]
62. Yang, F.; Deng, D.; Pan, X.; Fu, Q.; Bao, X. Understanding nano effects in catalysis. *Natl. Sci. Rev.* **2015**, *2*, 183–201. [[CrossRef](#)]
63. Dinh, C.T.; Nguyen, T.D.; Kleitz, F.; Do, T.O. Chapter 10—Shape-Controlled Synthesis of Metal Oxide Nanocrystals. In *Book Controlled Nanofabrication: Advances and Applications*, 1st ed.; Lui, R.-S., Ed.; Pan Stanford Publishing Pte. Ltd.: Singapore, 2012; pp. 327–367. ISBN 978-981-4316-87-3.
64. Aneggi, E.; Wiaterski, D.; De Leitenburg, C.; Llorca, J.; Trovarelli, A. Shape-Dependent Activity of Ceria in Soot Combustion. *ACS Catal.* **2014**, *4*, 172–181. [[CrossRef](#)]
65. Ta, N.; Liu, J.; Shen, W. Tuning the shape of ceria nanomaterials for catalytic applications. *Chin. J. Catal.* **2013**, *34*, 838–850. [[CrossRef](#)]
66. Li, Y.; Shen, W. Morphology-dependent nanocatalysts: Rod-shaped oxides. *Chem. Soc. Rev.* **2014**, *43*, 1543–1574. [[CrossRef](#)]
67. Zhou, K.; Li, Y. Catalysis Based on Nanocrystals with Well-Defined Facets. *Angew. Chem. Int. Ed.* **2012**, *51*, 602–613. [[CrossRef](#)]
68. Liu, L.; Corma, A. Metal Catalysts for Heterogeneous Catalysis: From Single Atoms to Nanoclusters and Nanoparticles. *Chem. Rev.* **2018**, *118*, 4981–5079. [[CrossRef](#)]
69. Capdevila-Cortada, M.; Vilé, G.; Teschner, D.; Pérez-Ramírez, J.; López, N. Reactivity descriptors for ceria in catalysis. *Appl. Catal. B Environ.* **2016**, *197*, 299–312. [[CrossRef](#)]
70. Cao, S.; Tao, F.; Tang, Y.; Li, Y.; Yu, J. Size- and shape-dependent catalytic performances of oxidation and reduction reactions on nanocatalysts. *Chem. Soc. Rev.* **2016**, *45*, 4747–4765. [[CrossRef](#)]
71. Xu, J.; Harmer, J.; Li, G.; Chapman, T.; Collier, P.; Longworth, S.; Tsang, S.C. Size dependent oxygen buffering capacity of ceria nanocrystals. *Chem. Commun.* **2010**, *46*, 1887–1889. [[CrossRef](#)]
72. Puigdollers, A.R.; Schlexer, P.; Tosoni, S.; Pacchioni, G. Increasing Oxide Reducibility: The Role of Metal/Oxide Interfaces in the Formation of Oxygen Vacancies. *ACS Catal.* **2017**, *7*, 6493–6513. [[CrossRef](#)]
73. Sayle, T.X.T.; Caddeo, F.; Zhang, X.; Sakthivel, T.; Das, S.; Seal, S.; Ptasinska, S.; Sayle, D.C. Structure-Activity Map of Ceria Nanoparticles, Nanocubes, and Mesoporous Architectures. *Chem. Mater.* **2016**, *28*, 7287–7295. [[CrossRef](#)]
74. Roldan Cuenya, B. Synthesis and catalytic properties of metal nanoparticles: Size, shape, support, composition, and oxidation state effects. *Thin Solid Films* **2010**, *518*, 3127–3150. [[CrossRef](#)]
75. Martínez-Arias, A.; Gamarra, D.; Hungria, A.B.; Fernández-García, M.; Munuera, G.; Hornés, A.; Bera, P.; Conesa, J.C.; Cámara, A.L. Characterization of Active Sites/Entities and Redox/Catalytic Correlations in Copper-Ceria-Based Catalysts for Preferential Oxidation of CO in H<sub>2</sub>-Rich Streams. *Catalysts* **2013**, *3*, 378–400. [[CrossRef](#)]
76. Prasad, R.; Rattan, G. Preparation Methods and Applications of CuO-CeO<sub>2</sub> Catalysts: A Short Review. *Bull. Chem. React. Eng. Catal.* **2010**, *5*, 7–30. [[CrossRef](#)]
77. Beckers, J.; Rothenberg, G. Sustainable selective oxidations using ceria-based materials. *Green Chem.* **2010**, *12*, 939–948. [[CrossRef](#)]
78. Philippot, K.; Serp, P. Chapter 1—Concepts in Nanocatalysis. In *Book Nanomaterials in Catalysis*, 1st ed.; Serp, P., Philippot, K., Eds.; Wiley-VCH Verlag GmbH & Co. KGaA.: Weinheim, Germany, 2013; pp. 1–54. [[CrossRef](#)]
79. Che, M.; Bennett, C.O. The Influence of Particle Size on the Catalytic Properties of Supported Metals. *Adv. Catal.* **1989**, *36*, 55–172. [[CrossRef](#)]

80. Hvolbæk, B.; Janssens, T.V.W.; Clausen, B.S.; Falsig, H.; Christensen, C.H.; Nørskov, J.K. Catalytic activity of Au nanoparticles. *Nano Today* **2007**, *2*, 14–18. [[CrossRef](#)]
81. Tao, F.; Dag, S.; Wang, L.-W.; Liu, Z.; Butcher, D.R.; Bluhm, H.; Salmeron, M.; Somorjai, G.A. Break-Up of Stepped Platinum Catalyst Surfaces by High CO Coverage. *Science* **2010**, *327*, 850–853. [[CrossRef](#)]
82. Qiao, Z.-A.; Wu, Z.; Dai, S. Shape-Controlled Ceria-Based Nanostructures for Catalysis Applications. *ChemSusChem* **2013**, *6*, 1821–1833. [[CrossRef](#)]
83. Vinod, C.P. Surface science as a tool for probing nanocatalysis phenomena. *Catal. Today* **2010**, *154*, 113–117. [[CrossRef](#)]
84. Somorjai, G.A.; Li, Y. *Introduction to Surface Chemistry and Catalysis*, 2nd ed.; John Wiley & Sons: Hoboken, NJ, USA, 2010; ISBN 978-0-470-50823-7.
85. Calle-Vallejo, F.; Loffreda, D.; Koper, M.T.M.; Sautet, P. Introducing structural sensitivity into adsorption-energy scaling relations by means of coordination numbers. *Nat. Chem.* **2015**, *7*, 403–410. [[CrossRef](#)] [[PubMed](#)]
86. Brodersen, S.H.; Grønbjerg, U.; Hvolbæk, B.; Schiøtz, J. Understanding the catalytic activity of gold nanoparticles through multi-scale simulations. *J. Catal.* **2011**, *284*, 34–41. [[CrossRef](#)]
87. Hamid, S.B.A.; Schlögl, R. The Impact of Nanoscience in Heterogeneous Catalysis. In *Book Nano-Micro Interface Bridging Micro Nano Worlds*, 2nd ed.; Van de Voorde, M., Werner, M., Fecht, H.-J., Eds.; Wiley-VCH Verlag GmbH & Co. KGaA.: Hoboken, NJ, USA, 2015; Volume 2, pp. 405–430. [[CrossRef](#)]
88. Cleveland, C.L.; Landman, U.; Schaaff, T.G.; Shafiqullin, M.N.; Stephens, P.W.; Whetten, R.L. Structural Evolution of Smaller Gold Nanocrystals: The Truncated Decahedral Motif. *Phys. Rev. Lett.* **1997**, *79*, 1873–1876. [[CrossRef](#)]
89. Chen, M.; Goodman, D.W. Catalytically active gold on ordered titania supports. *Chem. Soc. Rev.* **2008**, *37*, 1860–1870. [[CrossRef](#)]
90. Van Bokhoven, J.A.; Louis, C.; Miller, J.T.; Tromp, M.; Safonova, O.V.; Glatzel, P. Activation of Oxygen on Gold/Alumina Catalysts: In Situ High-Energy-Resolution Fluorescence and Time-Resolved X-ray Spectroscopy. *Angew. Chem. Int. Ed.* **2006**, *45*, 4651–4654. [[CrossRef](#)]
91. Walsh, M.J.; Yoshida, K.; Kuwabara, A.; Pay, M.L.; Gai, P.L.; Boyes, E.D. On the Structural Origin of the Catalytic Properties of Inherently Strained Ultrasmall Decahedral Gold Nanoparticles. *Nano Lett.* **2012**, *12*, 2027–2031. [[CrossRef](#)]
92. Senanayake, S.D.; Rodriguez, J.A.; Stacchiola, D. Electronic Metal-Support Interactions and the Production of Hydrogen Through the Water-Gas Shift Reaction and Ethanol Steam Reforming: Fundamental Studies with Well-Defined Model Catalysts. *Top. Catal.* **2013**, *56*, 1488–1498. [[CrossRef](#)]
93. Hu, P.; Huang, Z.; Amghouz, Z.; Makkee, M.; Xu, F.; Kapteijn, F.; Dikhtiarenko, A.; Chen, Y.; Gu, X.; Tang, X. Electronic Metal-Support Interactions in Single-Atom Catalysts. *Angew. Chem. Int. Ed.* **2014**, *53*, 3418–3421. [[CrossRef](#)]
94. Han, Z.-K.; Zhang, L.; Liu, M.; Ganduglia-Pirovano, M.V.; Gao, Y. The Structure of Oxygen Vacancies in the Near-Surface of Reduced CeO<sub>2</sub> (111) Under Strain. *Front. Chem.* **2019**, *7*, 436. [[CrossRef](#)]
95. Murugan, B.; Ramaswamy, A.V. Defect-Site Promoted Surface Reorganization in Nanocrystalline Ceria for the Low-Temperature Activation of Ethylbenzene. *J. Am. Chem. Soc.* **2007**, *129*, 3062–3063. [[CrossRef](#)] [[PubMed](#)]
96. Campbell, C.T. Catalyst-support interactions: Electronic perturbations. *Nat. Chem.* **2012**, *4*, 597–598. [[CrossRef](#)] [[PubMed](#)]
97. Sun, C.; Li, H.; Chen, L. Nanostructured ceria-based materials: Synthesis, properties, and applications. *Energy Environ. Sci.* **2012**, *5*, 8475–8505. [[CrossRef](#)]
98. Zhou, X.-D.; Huebner, W. Size-induced lattice relaxation in CeO<sub>2</sub> nanoparticles. *Appl. Phys. Lett.* **2001**, *79*, 3512–3514. [[CrossRef](#)]
99. Dutta, P.; Pal, S.; Seehra, M.S.; Shi, Y.; Eyring, E.M.; Ernst, R.D. Concentration of Ce<sup>3+</sup> and Oxygen Vacancies in Cerium Oxide Nanoparticles. *Chem. Mater.* **2006**, *18*, 5144–5146. [[CrossRef](#)]
100. Hailstone, R.K.; DiFrancesco, A.G.; Leong, J.G.; Allston, T.D.; Reed, K.J. A Study of Lattice Expansion in CeO<sub>2</sub> Nanoparticles by Transmission Electron Microscopy. *J. Phys. Chem. C* **2009**, *113*, 15155–15159. [[CrossRef](#)]
101. Migani, A.; Vayssilov, G.N.; Bromley, S.T.; Illas, F.; Neyman, K.M. Dramatic reduction of the oxygen vacancy formation energy in ceria particles: a possible key to their remarkable reactivity at the nanoscale. *J. Mater. Chem.* **2010**, *20*, 10535–10546. [[CrossRef](#)]

102. Bruix, A.; Neyman, K.M. Modeling Ceria-Based Nanomaterials for Catalysis and Related Applications. *Catal. Lett.* **2016**, *146*, 2053–2080. [[CrossRef](#)]
103. Sk, M.A.; Kozlov, S.M.; Lim, K.H.; Migani, A.; Neyman, K.M. Oxygen vacancies in self-assemblies of ceria nanoparticles. *J. Mater. Chem. A* **2014**, *2*, 18329–18338. [[CrossRef](#)]
104. Trovarelli, A.; Llorca, J. Ceria Catalysts at Nanoscale: How Do Crystal Shapes Shape Catalysis? *ACS Catal.* **2017**, *7*, 4716–4735. [[CrossRef](#)]
105. Li, Y.; Liu, Q.; Shen, W. Morphology-dependent nanocatalysis: metal particles. *Dalt. Trans.* **2011**, *40*, 5811–5826. [[CrossRef](#)] [[PubMed](#)]
106. Huang, W.; Gao, Y. Morphology-dependent surface chemistry and catalysis of CeO<sub>2</sub> nanocrystals. *Catal. Sci. Technol.* **2014**, *4*, 3772–3784. [[CrossRef](#)]
107. Datta, S.; Torrente-Murciano, L. Nanostructured faceted ceria as oxidation catalyst. *Curr. Opin. Chem. Eng.* **2018**, *20*, 99–106. [[CrossRef](#)]
108. Munnik, P.; De Jongh, P.E.; De Jong, K.P. Recent Developments in the Synthesis of Supported Catalysts. *Chem. Rev.* **2015**, *115*, 6687–6718. [[CrossRef](#)]
109. Vilé, G.; Colussi, S.; Krumeich, F.; Trovarelli, A.; Pérez-Ramírez, J. Opposite Face Sensitivity of CeO<sub>2</sub> in Hydrogenation and Oxidation Catalysis. *Angew. Chem. Int. Ed.* **2014**, *53*, 12069–12072. [[CrossRef](#)]
110. Yuan, Q.; Duan, H.-H.; Li, L.-L.; Sun, L.-D.; Zhang, Y.-W.; Yan, C.-H. Controlled synthesis and assembly of ceria-based nanomaterials. *J. Colloid Interface Sci.* **2009**, *335*, 151–167. [[CrossRef](#)]
111. Mullins, D.R. The surface chemistry of cerium oxide. *Surf. Sci. Rep.* **2015**, *70*, 42–85. [[CrossRef](#)]
112. Paier, J.; Penschke, C.; Sauer, J. Oxygen Defects and Surface Chemistry of Ceria: Quantum Chemical Studies Compared to Experiment. *Chem. Rev.* **2013**, *113*, 3949–3985. [[CrossRef](#)]
113. Yang, W.; Wang, X.; Song, S.; Zhang, H. Syntheses and Applications of Noble-Metal-free CeO<sub>2</sub>-Based Mixed-Oxide Nanocatalysts. *Chem* **2019**, *5*, 1743–1774. [[CrossRef](#)]
114. Castanet, U.; Feral-Martin, C.; Demourgues, A.; Neale, R.L.; Sayle, D.C.; Caddeo, F.; Flitcroft, J.M.; Caygill, R.; Pointon, B.J.; Molinari, M.; et al. Controlling the {111}/{110} Surface Ratio of Cuboidal Ceria Nanoparticles. *ACS Appl. Mater. Interfaces* **2019**, *11*, 11384–11390. [[CrossRef](#)]
115. Lykaki, M.; Pachatouridou, E.; Carabineiro, S.A.C.; Iliopoulou, E.; Andriopoulou, C.; Kallithrakas-Kontos, N.; Boghosian, S.; Konsolakis, M. Ceria nanoparticles shape effects on the structural defects and surface chemistry: Implications in CO oxidation by Cu/CeO<sub>2</sub> catalysts. *Appl. Catal. B Environ.* **2018**, *230*, 18–28. [[CrossRef](#)]
116. Xie, Y.; Wu, J.; Jing, G.; Zhang, H.; Zeng, S.; Tian, X.; Zou, X.; Wen, J.; Su, H.; Zhong, C.-J.; et al. Structural origin of high catalytic activity for preferential CO oxidation over CuO/CeO<sub>2</sub> nanocatalysts with different shapes. *Appl. Catal. B Environ.* **2018**, *239*, 665–676. [[CrossRef](#)]
117. He, H.; Yang, P.; Li, J.; Shi, R.; Chen, L.; Zhang, A.; Zhu, Y. Controllable synthesis, characterization, and CO oxidation activity of CeO<sub>2</sub> nanostructures with various morphologies. *Ceram. Int.* **2016**, *42*, 7810–7818. [[CrossRef](#)]
118. Chang, H.; Ma, L.; Yang, S.; Li, J.; Chen, L.; Wang, W.; Hao, J. Comparison of preparation methods for ceria catalyst and the effect of surface and bulk sulfates on its activity toward NH<sub>3</sub>-SCR. *J. Hazard. Mater.* **2013**, *262*, 782–788. [[CrossRef](#)] [[PubMed](#)]
119. Gawade, P.; Mirkelamoglu, B.; Ozkan, U.S. The Role of Support Morphology and Impregnation Medium on the Water Gas Shift Activity of Ceria-Supported Copper Catalysts. *J. Phys. Chem. C* **2010**, *114*, 18173–18181. [[CrossRef](#)]
120. Liu, Y.H.; Zuo, J.C.; Ren, X.F.; Yong, L. Synthesis and character of cerium oxide (CeO<sub>2</sub>) nanoparticles by the precipitation method. *Metalurgija* **2014**, *53*, 463–465.
121. Lykaki, M.; Pachatouridou, E.; Iliopoulou, E.; Carabineiro, S.A.C.; Konsolakis, M. Impact of the synthesis parameters on the solid state properties and the CO oxidation performance of ceria nanoparticles. *RSC Adv.* **2017**, *7*, 6160–6169. [[CrossRef](#)]
122. Shang, H.; Zhang, X.; Xu, J.; Han, Y. Effects of preparation methods on the activity of CuO/CeO<sub>2</sub> catalysts for CO oxidation. *Front. Chem. Sci. Eng.* **2017**, *11*, 603–612. [[CrossRef](#)]
123. Zhou, L.; Li, X.; Yao, Z.; Chen, Z.; Hong, M.; Zhu, R.; Liang, Y.; Zhao, J. Transition-Metal Doped Ceria Microspheres with Nanoporous Structures for CO Oxidation. *Sci. Rep.* **2016**, *6*, 23900. [[CrossRef](#)]
124. Wang, W.-W.; Yu, W.-Z.; Du, P.-P.; Xu, H.; Jin, Z.; Si, R.; Ma, C.; Shi, S.; Jia, C.-J.; Yan, C.-H. Crystal Plane Effect of Ceria on Supported Copper Oxide Cluster Catalyst for CO Oxidation: Importance of Metal-Support Interaction. *ACS Catal.* **2017**, *7*, 1313–1329. [[CrossRef](#)]

125. Nakagawa, K.; Ohshima, T.; Tezuka, Y.; Katayama, M.; Katoh, M.; Sugiyama, S. Morphological effects of CeO<sub>2</sub> nanostructures for catalytic soot combustion of CuO/CeO<sub>2</sub>. *Catal. Today* **2015**, *246*, 67–71. [[CrossRef](#)]
126. Chaudhary, S.; Sharma, P.; Kumar, R.; Mehta, S.K. Nanoscale surface designing of Cerium oxide nanoparticles for controlling growth, stability, optical and thermal properties. *Ceram. Int.* **2015**, *41*, 10995–11003. [[CrossRef](#)]
127. Miyazaki, H.; Kato, J.-I.; Sakamoto, N.; Wakiya, N.; Ota, T.; Suzuki, H. Synthesis of CeO<sub>2</sub> nanoparticles by rapid thermal decomposition using microwave heating. *Adv. Appl. Ceram.* **2010**, *109*, 123–127. [[CrossRef](#)]
128. Yang, H.; Huang, C.; Tang, A.; Zhang, X.; Yang, W. Microwave-assisted synthesis of ceria nanoparticles. *Mater. Res. Bull.* **2005**, *40*, 1690–1695. [[CrossRef](#)]
129. Zawadzki, M. Preparation and characterization of ceria nanoparticles by microwave-assisted solvothermal process. *J. Alloys Compd.* **2008**, *454*, 347–351. [[CrossRef](#)]
130. Zhang, Y.-W.; Si, R.; Liao, C.-S.; Yan, C.-H.; Xiao, C.-X.; Kou, Y. Facile Alcohothermal Synthesis, Size-Dependent Ultraviolet Absorption, and Enhanced CO Conversion Activity of Ceria Nanocrystals. *J. Phys. Chem. B* **2003**, *107*, 10159–10167. [[CrossRef](#)]
131. Ouyang, B.; Tan, W.; Liu, B. Morphology effect of nanostructure ceria on the Cu/CeO<sub>2</sub> catalysts for synthesis of methanol from CO<sub>2</sub> hydrogenation. *Catal. Commun.* **2017**, *95*, 36–39. [[CrossRef](#)]
132. Mai, H.-X.; Sun, L.-D.; Zhang, Y.-W.; Si, R.; Feng, W.; Zhang, H.-P.; Liu, H.-C.; Yan, C.-H. Shape-Selective Synthesis and Oxygen Storage Behavior of Ceria Nanopolyhedra, Nanorods, and Nanocubes. *J. Phys. Chem. B* **2005**, *109*, 24380–24385. [[CrossRef](#)]
133. Gamarra, D.; López Cámara, A.; Monte, M.; Rasmussen, S.B.; Chinchilla, L.E.; Hungria, A.B.; Munuera, G.; Gyorffy, N.; Schay, Z.; Cortés Corberán, V.; et al. Preferential oxidation of CO in excess H<sub>2</sub> over CuO/CeO<sub>2</sub> catalysts: Characterization and performance as a function of the exposed face present in the CeO<sub>2</sub> support. *Appl. Catal. B Environ.* **2013**, *130–131*, 224–238. [[CrossRef](#)]
134. Piumetti, M.; Bensaid, S.; Andana, T.; Dosa, M.; Novara, C.; Giorgis, F.; Russo, N.; Fino, D. Nanostructured Ceria-Based Materials: Effect of the Hydrothermal Synthesis Conditions on the Structural Properties and Catalytic Activity. *Catalysts* **2017**, *7*, 174. [[CrossRef](#)]
135. Araiza, D.G.; Gómez-Cortés, A.; Díaz, G. Partial oxidation of methanol over copper supported on nanoshaped ceria for hydrogen production. *Catal. Today* **2017**, *282*, 185–194. [[CrossRef](#)]
136. Yao, S.Y.; Xu, W.Q.; Johnston-Peck, A.C.; Zhao, F.Z.; Liu, Z.Y.; Luo, S.; Senanayake, S.D.; Martínez-Arias, A.; Liu, W.J.; Rodriguez, J.A. Morphological effects of the nanostructured ceria support on the activity and stability of CuO/CeO<sub>2</sub> catalysts for the water-gas shift reaction. *Phys. Chem. Chem. Phys.* **2014**, *16*, 17183–17195. [[CrossRef](#)] [[PubMed](#)]
137. Lin, L.; Yao, S.; Liu, Z.; Zhang, F.; Li, N.; Vovchok, D.; Martínez-Arias, A.; Castañeda, R.; Lin, J.; Senanayake, S.D.; et al. In Situ Characterization of Cu/CeO<sub>2</sub> Nanocatalysts for CO<sub>2</sub> Hydrogenation: Morphological Effects of Nanostructured Ceria on the Catalytic Activity. *J. Phys. Chem. C* **2018**, *122*, 12934–12943. [[CrossRef](#)]
138. Andana, T.; Piumetti, M.; Bensaid, S.; Veyre, L.; Thieuleux, C.; Russo, N.; Fino, D.; Quadrelli, E.A.; Pirone, R. CuO nanoparticles supported by ceria for NO<sub>x</sub>-assisted soot oxidation: insight into catalytic activity and sintering. *Appl. Catal. B Environ.* **2017**, *216*, 41–58. [[CrossRef](#)]
139. Miceli, P.; Bensaid, S.; Russo, N.; Fino, D. Effect of the morphological and surface properties of CeO<sub>2</sub>-based catalysts on the soot oxidation activity. *Chem. Eng. J.* **2015**, *278*, 190–198. [[CrossRef](#)]
140. Liu, J.; Li, Y.; Zhang, J.; He, D. Glycerol carbonylation with CO<sub>2</sub> to glycerol carbonate over CeO<sub>2</sub> catalyst and the influence of CeO<sub>2</sub> preparation methods and reaction parameters. *Appl. Catal. A Gen.* **2016**, *513*, 9–18. [[CrossRef](#)]
141. He, H.-W.; Wu, X.-Q.; Ren, W.; Shi, P.; Yao, X.; Song, Z.-T. Synthesis of crystalline cerium dioxide hydrosol by a sol-gel method. *Ceram. Int.* **2012**, *38S*, S501–S504. [[CrossRef](#)]
142. Phonthammachai, N.; Rumruangwong, M.; Gulari, E.; Jamieson, A.M.; Jitkarnka, S.; Wongkasemjit, S. Synthesis and rheological properties of mesoporous nanocrystalline CeO<sub>2</sub> via sol-gel process. *Colloids Surf. A Physicochem. Eng. Asp.* **2004**, *247*, 61–68. [[CrossRef](#)]
143. Pinjari, D.V.; Pandit, A.B. Room temperature synthesis of crystalline CeO<sub>2</sub> nanopowder: Advantage of sonochemical method over conventional method. *Ultrason. Sonochem.* **2011**, *18*, 1118–1123. [[CrossRef](#)]
144. Yin, L.; Wang, Y.; Pang, G.; Koltypin, Y.; Gedanken, A. Sonochemical Synthesis of Cerium Oxide Nanoparticles—Effect of Additives and Quantum Size Effect. *J. Colloid Interface Sci.* **2002**, *246*, 78–84. [[CrossRef](#)]

145. Roldan Cuenya, B.; Behafarid, F. Nanocatalysis: size- and shape-dependent chemisorption and catalytic reactivity. *Surf. Sci. Rep.* **2015**, *70*, 135–187. [[CrossRef](#)]
146. Zabilskiy, M.; Djinović, P.; Tchernychova, E.; Tkachenko, O.P.; Kustov, L.M.; Pintar, A. Nanoshaped CuO/CeO<sub>2</sub> Materials: Effect of the Exposed Ceria Surfaces on Catalytic Activity in N<sub>2</sub>O Decomposition Reaction. *ACS Catal.* **2015**, *5*, 5357–5365. [[CrossRef](#)]
147. Cui, Y.; Dai, W.-L. Support morphology and crystal plane effect of Cu/CeO<sub>2</sub> nanomaterial on the physicochemical and catalytic properties for carbonate hydrogenation. *Catal. Sci. Technol.* **2016**, *6*, 7752–7762. [[CrossRef](#)]
148. Liu, L.; Yao, Z.; Deng, Y.; Gao, F.; Liu, B.; Dong, L. Morphology and Crystal-Plane Effects of Nanoscale Ceria on the Activity of CuO/CeO<sub>2</sub> for NO Reduction by CO. *ChemCatChem* **2011**, *3*, 978–989. [[CrossRef](#)]
149. López, J.M.; Gilbank, A.L.; García, T.; Solsona, B.; Agouram, S.; Torrente-Murciano, L. The prevalence of surface oxygen vacancies over the mobility of bulk oxygen in nanostructured ceria for the total toluene oxidation. *Appl. Catal. B Environ.* **2015**, *174–175*, 403–412. [[CrossRef](#)]
150. Araiza, D.G.; Gómez-Cortés, A.; Díaz, G. Reactivity of methanol over copper supported on well-shaped CeO<sub>2</sub>: A TPD-DRIFTS study. *Catal. Sci. Technol.* **2017**, *7*, 5224–5235. [[CrossRef](#)]
151. Sudarsanam, P.; Hillary, B.; Amin, M.H.; Rockstroh, N.; Bentrup, U.; Brückner, A.; Bhargava, S.K. Heterostructured Copper-Ceria and Iron-Ceria Nanorods: Role of Morphology, Redox, and Acid Properties in Catalytic Diesel Soot Combustion. *Langmuir* **2018**, *34*, 2663–2673. [[CrossRef](#)]
152. Piumetti, M.; Bensaid, S.; Russo, N.; Fino, D. Nanostructured ceria-based catalysts for soot combustion: Investigations on the surface sensitivity. *Appl. Catal. B Environ.* **2015**, *165*, 742–751. [[CrossRef](#)]
153. Wang, S.; Zhao, L.; Wang, W.; Zhao, Y.; Zhang, G.; Ma, X.; Gong, J. Morphology control of ceria nanocrystals for catalytic conversion of CO<sub>2</sub> with methanol. *Nanoscale* **2013**, *5*, 5582–5588. [[CrossRef](#)]
154. Wu, Z.; Li, M.; Overbury, S.H. On the structure dependence of CO oxidation over CeO<sub>2</sub> nanocrystals with well-defined surface planes. *J. Catal.* **2012**, *285*, 61–73. [[CrossRef](#)]
155. Kovacevic, M.; Mojet, B.L.; Van Ommen, J.G.; Lefferts, L. Effects of Morphology of Cerium Oxide Catalysts for Reverse Water Gas Shift Reaction. *Catal. Lett.* **2016**, *146*, 770–777. [[CrossRef](#)]
156. Piumetti, M.; Andana, T.; Bensaid, S.; Russo, N.; Fino, D.; Pirone, R. Study on the CO Oxidation over Ceria-Based Nanocatalysts. *Nanoscale Res. Lett.* **2016**, *11*, 165. [[CrossRef](#)] [[PubMed](#)]
157. Guo, X.; Zhou, R. A new insight into the morphology effect of ceria on CuO/CeO<sub>2</sub> catalysts for CO selective oxidation in hydrogen-rich gas. *Catal. Sci. Technol.* **2016**, *6*, 3862–3871. [[CrossRef](#)]
158. Mock, S.A.; Sharp, S.E.; Stoner, T.R.; Radetic, M.J.; Zell, E.T.; Wang, R. CeO<sub>2</sub> nanorods-supported transition metal catalysts for CO oxidation. *J. Colloid Interface Sci.* **2016**, *466*, 261–267. [[CrossRef](#)]
159. Ren, Z.; Peng, F.; Li, J.; Liang, X.; Chen, B. Morphology-Dependent Properties of Cu/CeO<sub>2</sub> Catalysts for the Water-Gas Shift Reaction. *Catalysts* **2017**, *7*, 48. [[CrossRef](#)]
160. Li, Y.; Wei, Z.; Gao, F.; Kovarik, L.; Peden, C.H.F.; Wang, Y. Effects of CeO<sub>2</sub> support facets on VO<sub>x</sub>/CeO<sub>2</sub> catalysts in oxidative dehydrogenation of methanol. *J. Catal.* **2014**, *315*, 15–24. [[CrossRef](#)]
161. Mudiyansele, K.; Senanayake, S.D.; Feria, L.; Kundu, S.; Baber, A.E.; Graciani, J.; Vidal, A.B.; Agnoli, S.; Evans, J.; Chang, R.; et al. Importance of the Metal-Oxide Interface in Catalysis: In Situ Studies of the Water-Gas Shift Reaction by Ambient-Pressure X-ray Photoelectron Spectroscopy. *Angew. Chem. Int. Ed.* **2013**, *52*, 5101–5105. [[CrossRef](#)]
162. Mayernick, A.D.; Janik, M.J. Methane Activation and Oxygen Vacancy Formation over CeO<sub>2</sub> and Zr, Pd Substituted CeO<sub>2</sub> Surfaces. *J. Phys. Chem. C* **2008**, *112*, 14955–14964. [[CrossRef](#)]
163. Nolan, M.; Grigoleit, S.; Sayle, D.C.; Parker, S.C.; Watson, G.W. Density functional theory studies of the structure and electronic structure of pure and defective low index surfaces of ceria. *Surf. Sci.* **2005**, *576*, 217–229. [[CrossRef](#)]
164. Nolan, M.; Parker, S.C.; Watson, G.W. The electronic structure of oxygen vacancy defects at the low index surfaces of ceria. *Surf. Sci.* **2005**, *595*, 223–232. [[CrossRef](#)]
165. Sayle, T.X.T.; Parker, S.C.; Sayle, D.C. Oxidising CO to CO<sub>2</sub> using ceria nanoparticles. *Phys. Chem. Chem. Phys.* **2005**, *7*, 2936–2941. [[CrossRef](#)] [[PubMed](#)]
166. Sayle, T.X.T.; Cantoni, M.; Bhatta, U.M.; Parker, S.C.; Hall, S.R.; Möbus, G.; Molinari, M.; Reid, D.; Seal, S.; Sayle, D.C. Strain and Architecture-Tuned Reactivity in Ceria Nanostructures; Enhanced Catalytic Oxidation of CO to CO<sub>2</sub>. *Chem. Mater.* **2012**, *24*, 1811–1821. [[CrossRef](#)]
167. Spencer, N.D.; Schoonmaker, R.C.; Somorjai, G.A. Iron Single Crystals as Ammonia Synthesis Catalysts: Effect of Surface Structure on Catalyst Activity. *J. Catal.* **1982**, *74*, 129–135. [[CrossRef](#)]

168. Xie, S.; Choi, S.-I.; Xia, X.; Xia, Y. Catalysis on faceted noble-metal nanocrystals: both shape and size matter. *Curr. Opin. Chem. Eng.* **2013**, *2*, 142–150. [[CrossRef](#)]
169. Zhai, Y.; Pierre, D.; Si, R.; Deng, W.; Ferrin, P.; Nilekar, A.U.; Peng, G.; Herron, J.A.; Bell, D.C.; Saltsburg, H.; et al. Alkali-Stabilized Pt-OH<sub>x</sub> Species Catalyze Low-Temperature Water-Gas Shift Reactions. *Science* **2010**, *329*, 1633–1636. [[CrossRef](#)] [[PubMed](#)]
170. Stakheev, A.Y.; Kustov, L.M. Effects of the support on the morphology and electronic properties of supported metal clusters: modern concepts and progress in 1990s. *Appl. Catal. A Gen.* **1999**, *188*, 3–35. [[CrossRef](#)]
171. Lee, D.W.; Yoo, B.R. Advanced metal oxide (supported) catalysts: Synthesis and applications. *J. Ind. Eng. Chem.* **2014**, *20*, 3947–3959. [[CrossRef](#)]
172. Yentekakis, I.V.; Konsolakis, M.; Lambert, R.M.; MacLeod, N.; Nalbantian, L. Extraordinarily effective promotion by sodium in emission control catalysis: NO reduction by propene over Na-promoted Pt/ $\gamma$ -Al<sub>2</sub>O<sub>3</sub>. *Appl. Catal. B Environ.* **1999**, *22*, 123–133. [[CrossRef](#)]
173. Konsolakis, M.; Vrontaki, M.; Avgouropoulos, G.; Ioannides, T.; Yentekakis, I.V. Novel doubly-promoted catalysts for the lean NO<sub>x</sub> reduction by H<sub>2</sub> + CO: Pd(K)/Al<sub>2</sub>O<sub>3</sub>-(TiO<sub>2</sub>). *Appl. Catal. B Environ.* **2006**, *68*, 59–67. [[CrossRef](#)]
174. Konsolakis, M.; Aligizou, F.; Goula, G.; Yentekakis, I.V. N<sub>2</sub>O decomposition over doubly-promoted Pt(K)/Al<sub>2</sub>O<sub>3</sub>-(CeO<sub>2</sub>-La<sub>2</sub>O<sub>3</sub>) structured catalysts: On the combined effects of promotion and feed composition. *Chem. Eng. J.* **2013**, *230*, 286–295. [[CrossRef](#)]
175. Janek, J.C.G.; Vayenas, S.; Bebelis, C.; Pliangos, S.; Brosda, D. Tsiprakides: Electrochemical activation of catalysis: promotion, electrochemical promotion, and metal-support interaction. *J. Solid State Electrochem.* **2002**, *7*, 60–61. [[CrossRef](#)]
176. De Lucas-Consuegra, A. New Trends of Alkali Promotion in Heterogeneous Catalysis: Electrochemical Promotion with Alkaline Ionic Conductors. *Catal. Surv. Asia* **2015**, *19*, 25–37. [[CrossRef](#)]
177. Ertl, G.; Knözinger, H.; Weitkamp, J. *Handbook of Heterogeneous Catalysis*; VCH Verlagsgesellschaft mbH: Weinheim, Germany, 1997; ISBN 9783527619474.
178. Stelmachowski, P.; Maniak, G.; Kotarba, A.; Sojka, Z. Strong electronic promotion of Co<sub>3</sub>O<sub>4</sub> towards N<sub>2</sub>O decomposition by surface alkali dopants. *Catal. Commun.* **2009**, *10*, 1062–1065. [[CrossRef](#)]
179. Zasada, F.; Stelmachowski, P.; Maniak, G.; Paul, J.-F.; Kotarba, A.; Sojka, Z. Potassium Promotion of Cobalt Spinel Catalyst for N<sub>2</sub>O Decomposition—Accounted by Work Function Measurements and DFT Modelling. *Catal. Lett.* **2009**, *127*, 126–131. [[CrossRef](#)]
180. Kiskinova, M.P. Chapter 7—Theoretical Approaches to the Description of the Modifier Effects. In *Book Studies in Surface Science and Catalysis—Poisoning and Promotion in Catalysis based on Surface Science Concepts and Experiments*, 1st ed.; Kiskinova, M.P., Delmon, B., Yates, J.T., Eds.; Elsevier Science Publishers B.V.: Amsterdam, The Netherlands, 1991; Volume 70, pp. 285–307. [[CrossRef](#)]
181. Kiskinova, M.P. Chapter 4—Interaction of Atomic Adsorbates, Acting As Promoters Or Poisons With Single Crystal Metal Surfaces. In *Book Studies in Surface Science and Catalysis—Poisoning and Promotion in Catalysis Based on Surface Science Concepts and Experiments*, 1st ed.; Kiskinova, M.P., Delmon, B., Yates, J.T., Eds.; Elsevier Science Publishers B.V.: Amsterdam, The Netherlands, 1991; Volume 70, pp. 19–68. [[CrossRef](#)]
182. Huo, C.-F.; Wu, B.-S.; Gao, P.; Yang, Y.; Li, Y.-W.; Jiao, H. The Mechanism of Potassium Promoter: Enhancing the Stability of Active Surfaces. *Angew. Chem. Int. Ed.* **2011**, *50*, 7403–7406. [[CrossRef](#)]
183. Besenbacher, F.; Chorkendorff, I.; Clausen, B.S.; Hammer, B.; Molenbroek, A.M.; Nørskov, J.K.; Stensgaard, I. Design of a Surface Alloy Catalyst for Steam Reforming. *Science* **1998**, *279*, 1913–1915. [[CrossRef](#)]
184. Lamy, C.; Belgsir, E.M.; Léger, J.-M. Electrocatalytic oxidation of aliphatic alcohols: Application to the direct alcohol fuel cell (DAFC). *J. Appl. Electrochem.* **2001**, *31*, 799–809. [[CrossRef](#)]
185. Liang, Y.N.; Oh, W.-D.; Li, Y.; Hu, X. Nanocarbons as platforms for developing novel catalytic composites: overview and prospects. *Appl. Catal. A Gen.* **2018**, *562*, 94–105. [[CrossRef](#)]
186. Chen, W.; Fan, Z.; Pan, X.; Bao, X. Effect of Confinement in Carbon Nanotubes on the Activity of Fischer-Tropsch Iron Catalyst. *J. Am. Chem. Soc.* **2008**, *130*, 9414–9419. [[CrossRef](#)]
187. Geim, A.K.; Grigorieva, I.V. Van der Waals heterostructures. *Nature* **2013**, *499*, 419–425. [[CrossRef](#)]
188. Fu, Q.; Bao, X. Catalysis on a metal surface with a graphitic cover. *Chin. J. Catal.* **2015**, *36*, 517–519. [[CrossRef](#)]
189. Ania, C.O.; Seredych, M.; Rodriguez-Castellon, E.; Bandoz, T.J. New copper/GO based material as an efficient oxygen reduction catalyst in an alkaline medium: The role of unique Cu/rGO architecture. *Appl. Catal. B Environ.* **2015**, *163*, 424–435. [[CrossRef](#)]

190. Safaei, M.; Foroughi, M.M.; Ebrahimpour, N.; Jahani, S.; Omid, A.; Khatami, M. A review on metal-organic frameworks: Synthesis and applications. *TrAC Trends Anal. Chem.* **2019**, *118*, 401–425. [[CrossRef](#)]
191. Wang, Y.; Yang, Y.; Liu, N.; Wang, Y.; Zhang, X. Sword-like CuO/CeO<sub>2</sub> composites derived from a Ce-BTC metal-organic framework with superior CO oxidation performance. *RSC Adv.* **2018**, *8*, 33096–33102. [[CrossRef](#)]
192. Yang, Q.; Xu, Q.; Jiang, H.-L. Metal-organic frameworks meet metal nanoparticles: synergistic effect for enhanced catalysis. *Chem. Soc. Rev.* **2017**, *46*, 4774–4808. [[CrossRef](#)] [[PubMed](#)]
193. Chen, L.; Chen, H.; Luque, R.; Li, Y. Metal-organic framework encapsulated Pd nanoparticles: towards advanced heterogeneous catalysts. *Chem. Sci.* **2014**, *5*, 3708–3714. [[CrossRef](#)]
194. Chen, L.; Xu, Q. Metal-Organic Framework Composites for Catalysis. *Matter* **2019**, *1*, 57–89. [[CrossRef](#)]
195. Li, P.-Z.; Aranishi, K.; Xu, Q. ZIF-8 immobilized nickel nanoparticles: highly effective catalysts for hydrogen generation from hydrolysis of ammonia borane. *Chem. Commun.* **2012**, *48*, 3173–3175. [[CrossRef](#)]
196. Abdel-Mageed, A.M.; Rungtawevoranit, B.; Parlinska-Wojtan, M.; Pei, X.; Yaghi, O.M.; Jürgen Behm, R. Highly Active and Stable Single-Atom Cu Catalysts Supported by a Metal-Organic Framework. *J. Am. Chem. Soc.* **2019**, *141*, 5201–5210. [[CrossRef](#)]
197. Rungtawevoranit, B.; Baek, J.; Araujo, J.R.; Archanjo, B.S.; Choi, K.M.; Yaghi, O.M.; Somorjai, G.A. Copper Nanocrystals Encapsulated in Zr-based Metal-Organic Frameworks for Highly Selective CO<sub>2</sub> Hydrogenation to Methanol. *Nano Lett.* **2016**, *16*, 7645–7649. [[CrossRef](#)]
198. Ye, J.-Y.; Liu, C.-J. Cu<sub>3</sub>(BTC)<sub>2</sub>: CO oxidation over MOF based catalysts. *Chem. Commun.* **2011**, *47*, 2167–2169. [[CrossRef](#)] [[PubMed](#)]
199. Li, X.; Goh, T.W.; Li, L.; Xiao, C.; Guo, Z.; Zeng, X.C.; Huang, W. Controlling Catalytic Properties of Pd Nanoclusters through Their Chemical Environment at the Atomic Level Using Isoreticular Metal-Organic Frameworks. *ACS Catal.* **2016**, *6*, 3461–3468. [[CrossRef](#)]
200. Lawrence, N.J.; Brewer, J.R.; Wang, L.; Wu, T.-S.; Wells-Kingsbury, J.; Ihrig, M.M.; Wang, G.; Soo, Y.-L.; Mei, W.-N.; Cheung, C.L. Defect Engineering in Cubic Cerium Oxide Nanostructures for Catalytic Oxidation. *Nano Lett.* **2011**, *11*, 2666–2671. [[CrossRef](#)] [[PubMed](#)]
201. Mock, S.A.; Zell, E.T.; Hossain, S.T.; Wang, R. Effect of Reduction Treatment on CO Oxidation with CeO<sub>2</sub> Nanorod-Supported CuO<sub>x</sub> Catalysts. *ChemCatChem* **2018**, *10*, 311–319. [[CrossRef](#)]
202. Lin, B.; Qi, Y.; Wei, K.; Lin, J. Effect of pretreatment on ceria-supported cobalt catalyst for ammonia synthesis. *RSC Adv.* **2014**, *4*, 38093–38102. [[CrossRef](#)]
203. Ren, Y.; Tang, K.; Wei, J.; Yang, H.; Wei, H.; Yang, Y. Pretreatment Effect on Ceria-Supported Gold Nanocatalysts for CO Oxidation: Importance of the Gold–Ceria Interaction. *Energy Technol.* **2018**, *6*, 379–390. [[CrossRef](#)]
204. Gawande, M.B.; Goswami, A.; Felpin, F.-X.; Asefa, T.; Huang, X.; Silva, R.; Zou, X.; Zboril, R.; Varma, R.S. Cu and Cu-Based Nanoparticles: Synthesis and Applications in Catalysis. *Chem. Rev.* **2016**, *116*, 3722–3811. [[CrossRef](#)]
205. Zabilskiy, M.; Djinović, P.; Erjavec, B.; Dražić, G.; Pintar, A. Small CuO clusters on CeO<sub>2</sub> nanospheres as active species for catalytic N<sub>2</sub>O decomposition. *Appl. Catal. B Environ.* **2015**, *163*, 113–122. [[CrossRef](#)]
206. Li, L.; Zhan, Y.; Zheng, Q.; Zheng, Y.; Chen, C.; She, Y.; Lin, X.; Wei, K. Water-Gas Shift Reaction over CuO/CeO<sub>2</sub> Catalysts: Effect of the Thermal Stability and Oxygen Vacancies of CeO<sub>2</sub> Supports Previously Prepared by Different Methods. *Catal. Lett.* **2009**, *130*, 532–540. [[CrossRef](#)]
207. Li, L.; Song, L.; Wang, H.; Chen, C.; She, Y.; Zhan, Y.; Lin, X.; Zheng, Q. Water-gas shift reaction over CuO/CeO<sub>2</sub> catalysts: Effect of CeO<sub>2</sub> supports previously prepared by precipitation with different precipitants. *Int. J. Hydrogen Energy* **2011**, *36*, 8839–8849. [[CrossRef](#)]
208. Li, L.; Song, L.; Chen, C.; Zhang, Y.; Zhan, Y.; Lin, X.; Zheng, Q.; Wang, H.; Ma, H.; Ding, L.; et al. Modified precipitation processes and optimized copper content of CuO-CeO<sub>2</sub> catalysts for water-gas shift reaction. *Int. J. Hydrogen Energy* **2014**, *39*, 19570–19582. [[CrossRef](#)]
209. She, Y.; Li, L.; Zhan, Y.; Lin, X.; Zheng, Q.; Wei, K. Effect of yttrium addition on water-gas shift reaction over CuO/CeO<sub>2</sub> catalysts. *J. Rare Earths* **2009**, *27*, 411–417. [[CrossRef](#)]
210. Dong, F.; Meng, Y.; Han, W.; Zhao, H.; Tang, Z. Morphology effects on surface chemical properties and lattice defects of Cu/CeO<sub>2</sub> catalysts applied for low-temperature CO oxidation. *Sci. Rep.* **2019**, *9*, 12056. [[CrossRef](#)] [[PubMed](#)]

211. Fotopoulos, A.; Arvanitidis, J.; Christofilos, D.; Papaggelis, K.; Kalyva, M.; Triantafyllidis, K.; Niarchos, D.; Boukos, N.; Basina, G.; Tzitzios, V. One Pot Synthesis and Characterization of Ultra Fine CeO<sub>2</sub> and Cu/CeO<sub>2</sub> Nanoparticles. Application for Low Temperature CO Oxidation. *J. Nanosci. Nanotechnol.* **2011**, *11*, 8593–8598. [[CrossRef](#)]
212. Qin, J.; Lu, J.; Cao, M.; Hu, C. Synthesis of porous CuO-CeO<sub>2</sub> nanospheres with an enhanced low-temperature CO oxidation activity. *Nanoscale* **2010**, *2*, 2739–2743. [[CrossRef](#)] [[PubMed](#)]
213. Su, Y.; Dai, L.; Zhang, Q.; Li, Y.; Peng, J.; Wu, R.; Han, W.; Tang, Z.; Wang, Y. Fabrication of Cu-Doped CeO<sub>2</sub> Catalysts with Different Dimension Pore Structures for CO Catalytic Oxidation. *Catal. Surv. Asia* **2016**, *20*, 231–240. [[CrossRef](#)]
214. Zhou, H.; Huang, Z.; Sun, C.; Qin, F.; Xiong, D.; Shen, W.; Xu, H. Catalytic decomposition of N<sub>2</sub>O over Cu<sub>x</sub>Ce<sub>1-x</sub>O<sub>y</sub> mixed oxides. *Appl. Catal. B Environ.* **2012**, *125*, 492–498. [[CrossRef](#)]
215. Lykaki, M.; Papista, E.; Carabineiro, S.A.C.; Tavares, P.B.; Konsolakis, M. Optimization of N<sub>2</sub>O decomposition activity of CuO-CeO<sub>2</sub> mixed oxides by means of synthesis procedure and alkali (Cs) promotion. *Catal. Sci. Technol.* **2018**, *8*, 2312–2322. [[CrossRef](#)]
216. Liu, Z.; He, C.; Chen, B.; Liu, H. CuO-CeO<sub>2</sub> mixed oxide catalyst for the catalytic decomposition of N<sub>2</sub>O in the presence of oxygen. *Catal. Today* **2017**, *297*, 78–83. [[CrossRef](#)]
217. Yang, F.; Graciani, J.; Evans, J.; Liu, P.; Hrbek, J.; Sanz, J.F.; Rodriguez, J.A. CO oxidation on Inverse CeO<sub>x</sub>/Cu(111) Catalysts: High Catalytic Activity and Ceria-Promoted Dissociation of O<sub>2</sub>. *J. Am. Chem. Soc.* **2011**, *133*, 3444–3451. [[CrossRef](#)]
218. Berlowitz, P.J.; Peden, C.H.F.; Wayne Goodman, D. Kinetics of carbon monoxide oxidation on single-crystal palladium, platinum, and iridium. *J. Phys. Chem.* **1988**, *92*, 5213–5221. [[CrossRef](#)]
219. Rodriguez, J.A.; Wayne Goodman, D. High-pressure catalytic reactions over single-crystal metal surfaces. *Surf. Sci. Rep.* **1991**, *14*, 1–107. [[CrossRef](#)]
220. Gamarra, D.; Belver, C.; Fernández-García, M.; Martínez-Arias, A. Selective CO Oxidation in Excess H<sub>2</sub> over Copper-Ceria Catalysts: Identification of Active Entities/Species. *J. Am. Chem. Soc.* **2007**, *129*, 12064–12065. [[CrossRef](#)] [[PubMed](#)]
221. Senanayake, S.D.; Stacchiola, D.; Rodriguez, J.A. Unique Properties of Ceria Nanoparticles Supported on Metals: Novel Inverse Ceria/Copper Catalysts for CO Oxidation and the Water-Gas Shift Reaction. *Acc. Chem. Res.* **2013**, *46*, 1702–1711. [[CrossRef](#)] [[PubMed](#)]
222. Pillai, U.R.; Deevi, S. Room temperature oxidation of carbon monoxide over copper oxide catalyst. *Appl. Catal. B Environ.* **2006**, *64*, 146–151. [[CrossRef](#)]
223. Zhao, D.; Tu, C.-M.; Hu, X.-J.; Zhang, N. Notable in situ surface transformation of Cu<sub>2</sub>O nanomaterials leads to dramatic activity enhancement for CO oxidation. *RSC Adv.* **2017**, *7*, 37596–37603. [[CrossRef](#)]
224. Wang, X.; Liu, C.; Zheng, B.; Jiang, Y.; Zhang, L.; Xie, Z.; Zheng, L. Controlled synthesis of concave Cu<sub>2</sub>O microcrystals enclosed by {hhl} high-index facets and enhanced catalytic activity. *J. Mater. Chem. A* **2013**, *1*, 282–287. [[CrossRef](#)]
225. Zhou, K.; Wang, R.; Xu, B.; Li, Y. Synthesis, characterization and catalytic properties of CuO nanocrystals with various shapes. *Nanotechnology* **2006**, *17*, 3939–3943. [[CrossRef](#)]
226. Huang, H.; Zhang, L.; Wu, K.; Yu, Q.; Chen, R.; Yang, H.; Peng, X.; Ye, Z. Hetero-metal cation control of CuO nanostructures and their high catalytic performance for CO oxidation. *Nanoscale* **2012**, *4*, 7832–7841. [[CrossRef](#)]
227. Jia, A.-P.; Jiang, S.-Y.; Lu, J.-Q.; Luo, M.-F. Study of Catalytic Activity at the CuO–CeO<sub>2</sub> Interface for CO Oxidation. *J. Phys. Chem. C* **2010**, *114*, 21605–21610. [[CrossRef](#)]
228. Vayssilov, G.N.; Lykhach, Y.; Migani, A.; Staudt, T.; Petrova, G.P.; Tsud, N.; Skála, T.; Bruix, A.; Illas, F.; Prince, K.C.; et al. Support nanostructure boosts oxygen transfer to catalytically active platinum nanoparticles. *Nat. Mater.* **2011**, *10*, 310–315. [[CrossRef](#)] [[PubMed](#)]
229. Hossain, S.T.; Almesned, Y.; Zhang, K.; Zell, E.T.; Bernard, D.T.; Balaz, S.; Wang, R. Support structure effect on CO oxidation: A comparative study on SiO<sub>2</sub> nanospheres and CeO<sub>2</sub> nanorods supported CuO<sub>x</sub> catalysts. *Appl. Surf. Sci.* **2018**, *428*, 598–608. [[CrossRef](#)]
230. Yao, S.; Mudiyansele, K.; Xu, W.; Johnston-Peck, A.C.; Hanson, J.C.; Wu, T.; Stacchiola, D.; Rodriguez, J.A.; Zhao, H.; Beyer, K.A.; et al. Unraveling the Dynamic Nature of a CuO/CeO<sub>2</sub> Catalyst for CO Oxidation in Operando: A Combined Study of XANES (Fluorescence) and Drifts. *ACS Catal.* **2014**, *4*, 1650–1661. [[CrossRef](#)]

231. Hossain, S.T.; Azeeva, E.; Zhang, K.; Zell, E.T.; Bernard, D.T.; Balaz, S.; Wang, R. A comparative study of CO oxidation over Cu-O-Ce solid solutions and CuO/CeO<sub>2</sub> nanorods catalysts. *Appl. Surf. Sci.* **2018**, *455*, 132–143. [[CrossRef](#)]
232. Qi, L.; Yu, Q.; Dai, Y.; Tang, C.; Liu, L.; Zhang, H.; Gao, F.; Dong, L.; Chen, Y. Influence of cerium precursors on the structure and reducibility of mesoporous CuO-CeO<sub>2</sub> catalysts for CO oxidation. *Appl. Catal. B Environ.* **2012**, *119–120*, 308–320. [[CrossRef](#)]
233. Sun, S.; Mao, D.; Yu, J.; Yang, Z.; Lu, G.; Ma, Z. Low-temperature CO oxidation on CuO/CeO<sub>2</sub> catalysts: the significant effect of copper precursor and calcination temperature. *Catal. Sci. Technol.* **2015**, *5*, 3166–3181. [[CrossRef](#)]
234. Kappis, K.; Papadopoulos, C.; Papavasiliou, J.; Vakros, J.; Georgiou, Y.; Deligiannakis, Y.; Avgouropoulos, G. Tuning the Catalytic Properties of Copper-Promoted Nanoceria via a Hydrothermal Method. *Catalysts* **2019**, *9*, 138. [[CrossRef](#)]
235. Papadopoulos, C.; Kappis, K.; Papavasiliou, J.; Vakros, J.; Kuśmierz, M.; Gac, W.; Georgiou, Y.; Deligiannakis, Y.; Avgouropoulos, G. Copper-promoted ceria catalysts for CO oxidation reaction. *Catal. Today* **2019**, in press. [[CrossRef](#)]
236. Elias, J.S.; Risch, M.; Giordano, L.; Mansour, A.N.; Shao-Horn, Y. Structure, Bonding, and Catalytic Activity of Monodisperse, Transition-Metal-Substituted CeO<sub>2</sub> Nanoparticles. *J. Am. Chem. Soc.* **2014**, *136*, 17193–17200. [[CrossRef](#)]
237. Li, Y.; Cai, Y.; Xing, X.; Chen, N.; Deng, D.; Wang, Y. Catalytic activity for CO oxidation of Cu-CeO<sub>2</sub> composite nanoparticles synthesized by a hydrothermal method. *Anal. Methods* **2015**, *7*, 3238–3245. [[CrossRef](#)]
238. Ma, J.; Jin, G.; Gao, J.; Li, Y.; Dong, L.; Huang, M.; Huang, Q.; Li, B. Catalytic effect of two-phase intergrowth and coexistence CuO-CeO<sub>2</sub>. *J. Mater. Chem. A* **2015**, *3*, 24358–24370. [[CrossRef](#)]
239. Zhao, F.; Gong, M.; Zhang, G.; Li, J. Effect of the loading content of CuO on the activity and structure of CuO/Ce-Mn-O catalysts for CO oxidation. *J. Rare Earths* **2015**, *33*, 604–610. [[CrossRef](#)]
240. Lin, R.; Luo, M.-F.; Zhong, Y.-J.; Yan, Z.-L.; Liu, G.-Y.; Liu, W.-P. Comparative study of CuO/Ce<sub>0.7</sub>Sn<sub>0.3</sub>O<sub>2</sub>, CuO/CeO<sub>2</sub> and CuO/SnO<sub>2</sub> catalysts for low-temperature CO oxidation. *Appl. Catal. A Gen.* **2003**, *255*, 331–336. [[CrossRef](#)]
241. Zhang, X.-M.; Tian, P.; Tu, W.; Zhang, Z.; Xu, J.; Han, Y.-F. Tuning the Dynamic Interfacial Structure of Copper-Ceria Catalysts by Indium Oxide during CO Oxidation. *ACS Catal.* **2018**, *8*, 5261–5275. [[CrossRef](#)]
242. Li, W.; Shen, X.; Zeng, R.; Chen, J.; Xiao, W.; Ding, S.; Chen, C.; Zhang, R.; Zhang, N. Constructing copper-ceria nanosheets with high concentration of interfacial active sites for enhanced performance in CO oxidation. *Appl. Surf. Sci.* **2019**, *492*, 818–825. [[CrossRef](#)]
243. Song, X.-Z.; Su, Q.-F.; Li, S.-J.; Liu, S.-H.; Zhang, N.; Meng, Y.-L.; Chen, X.; Tan, Z. Triple-shelled CuO/CeO<sub>2</sub> hollow nanospheres derived from metal-organic frameworks as highly efficient catalysts for CO oxidation. *New J. Chem.* **2019**, *43*, 16096–16102. [[CrossRef](#)]
244. Liu, H.-H.; Wang, Y.; Jia, A.-P.; Wang, S.-Y.; Luo, M.-F.; Lu, J.-Q. Oxygen vacancy promoted CO oxidation over Pt/CeO<sub>2</sub> catalysts: A reaction at Pt-CeO<sub>2</sub> interface. *Appl. Surf. Sci.* **2014**, *314*, 725–734. [[CrossRef](#)]
245. Meng, L.; Jia, A.-P.; Lu, J.-Q.; Luo, L.-F.; Huang, W.-X.; Luo, M.-F. Synergetic Effects of PdO Species on CO Oxidation over PdO-CeO<sub>2</sub> Catalysts. *J. Phys. Chem. C* **2011**, *115*, 19789–19796. [[CrossRef](#)]
246. Konsolakis, M. Recent Advances on Nitrous Oxide (N<sub>2</sub>O) Decomposition over Non-Noble-Metal Oxide Catalysts: Catalytic Performance, Mechanistic Considerations, and Surface Chemistry Aspects. *ACS Catal.* **2015**, *5*, 6397–6421. [[CrossRef](#)]
247. Konsolakis, M.; Carabineiro, S.A.C.; Papista, E.; Marnellos, G.E.; Tavares, P.B.; Agostinho Moreira, J.; Romaguera-Barcelay, Y.; Figueiredo, J.L. Effect of preparation method on the solid state properties and the deN<sub>2</sub>O performance of CuO-CeO<sub>2</sub> oxides. *Catal. Sci. Technol.* **2015**, *5*, 3714–3727. [[CrossRef](#)]
248. Zabilskiy, M.; Erjavec, B.; Djinić, P.; Pintar, A. Ordered mesoporous CuO-CeO<sub>2</sub> mixed oxides as an effective catalyst for N<sub>2</sub>O decomposition. *Chem. Eng. J.* **2014**, *254*, 153–162. [[CrossRef](#)]
249. Parres-Esclapez, S.; Illán-Gómez, M.J.; De Lecea, C.S.M.; Bueno-López, A. On the importance of the catalyst redox properties in the N<sub>2</sub>O decomposition over alumina and ceria supported Rh, Pd and Pt. *Appl. Catal. B Environ.* **2010**, *96*, 370–378. [[CrossRef](#)]
250. Zhu, P.; Li, J.; Zuo, S.; Zhou, R. Preferential oxidation properties of CO in excess hydrogen over CuO-CeO<sub>2</sub> catalyst prepared by hydrothermal method. *Appl. Surf. Sci.* **2008**, *255*, 2903–2909. [[CrossRef](#)]

251. Du, P.-P.; Wang, W.-W.; Jia, C.-J.; Song, Q.-S.; Huang, Y.-Y.; Si, R. Effect of strongly bound copper species in copper-ceria catalyst for preferential oxidation of carbon monoxide. *Appl. Catal. A Gen.* **2016**, *518*, 87–101. [[CrossRef](#)]
252. Wu, Z.; Zhu, H.; Qin, Z.; Wang, H.; Ding, J.; Huang, L.; Wang, J. CO preferential oxidation in H<sub>2</sub>-rich stream over a CuO/CeO<sub>2</sub> catalyst with high H<sub>2</sub>O and CO<sub>2</sub> tolerance. *Fuel* **2013**, *104*, 41–45. [[CrossRef](#)]
253. Jampa, S.; Wangkawee, K.; Tantisriyanurak, S.; Changpradit, J.; Jamieson, A.M.; Chaisuwan, T.; Luengnaruemitchai, A.; Wongkasemjit, S. High performance and stability of copper loading on mesoporous ceria catalyst for preferential oxidation of CO in presence of excess of hydrogen. *Int. J. Hydrogen Energy* **2017**, *42*, 5537–5548. [[CrossRef](#)]
254. Arango-Díaz, A.; Moretti, E.; Talon, A.; Storaro, L.; Lenarda, M.; Núñez, P.; Marrero-Jerez, J.; Jiménez-Jiménez, J.; Jiménez-López, A.; Rodríguez-Castellón, E. Preferential CO oxidation (CO-PROX) catalyzed by CuO supported on nanocrystalline CeO<sub>2</sub> prepared by a freeze-drying method. *Appl. Catal. A Gen.* **2014**, *477*, 54–63. [[CrossRef](#)]
255. Wang, J.; Pu, H.; Wan, G.; Chen, K.; Lu, J.; Lei, Y.; Zhong, L.; He, S.; Han, C.; Luo, Y. Promoted the reduction of Cu<sup>2+</sup> to enhance CuO–CeO<sub>2</sub> catalysts for CO preferential oxidation in H<sub>2</sub>-rich streams: Effects of preparation methods and copper precursors. *Int. J. Hydrogen Energy* **2017**, *42*, 21955–21968. [[CrossRef](#)]
256. Shi, L.; Zhang, G.; Wang, Y. Tailoring catalytic performance of carbon nanotubes confined CuO–CeO<sub>2</sub> catalysts for CO preferential oxidation. *Int. J. Hydrogen Energy* **2018**, *43*, 18211–18219. [[CrossRef](#)]
257. Cecilia, J.A.; Arango-Díaz, A.; Marrero-Jerez, J.; Núñez, P.; Moretti, E.; Storaro, L.; Rodríguez-Castellón, E. Catalytic Behaviour of CuO–CeO<sub>2</sub> Systems Prepared by Different Synthetic Methodologies in the CO-PROX Reaction under CO<sub>2</sub>-H<sub>2</sub>O Feed Stream. *Catalysts* **2017**, *7*, 160. [[CrossRef](#)]
258. Han, J.; Kim, H.J.; Yoon, S.; Lee, H. Shape effect of ceria in Cu/ceria catalysts for preferential CO oxidation. *J. Mol. Catal. A Chem.* **2011**, *335*, 82–88. [[CrossRef](#)]
259. Zou, Q.; Zhao, Y.; Jin, X.; Fang, J.; Li, D.; Li, K.; Lu, J.; Luo, Y. Ceria-nano supported copper oxide catalysts for CO preferential oxidation: Importance of oxygen species and metal-support interaction. *Appl. Surf. Sci.* **2019**, *494*, 1166–1176. [[CrossRef](#)]
260. Yu, X.; Wu, J.; Zhang, A.; Xue, L.; Wang, Q.; Tian, X.; Shan, S.; Zhong, C.-J.; Zeng, S. Hollow copper-ceria microspheres with single and multiple shells for preferential CO oxidation. *CrystEngComm* **2019**, *21*, 3619–3626. [[CrossRef](#)]
261. Dongil, A.B.; Bachiller-Baeza, B.; Castillejos, E.; Escalona, N.; Guerrero-Ruiz, A.; Rodríguez-Ramos, I. Promoter effect of alkalis on CuO/CeO<sub>2</sub>/carbon nanotubes systems for the PROX reaction. *Catal. Today* **2018**, *301*, 141–146. [[CrossRef](#)]
262. Wang, W.-W.; Du, P.-P.; Zou, S.-H.; He, H.-Y.; Wang, R.-X.; Jin, Z.; Shi, S.; Huang, Y.-Y.; Si, R.; Song, Q.-S.; et al. Highly Dispersed Copper Oxide Clusters as Active Species in Copper-Ceria Catalyst for Preferential Oxidation of Carbon Monoxide. *ACS Catal.* **2015**, *5*, 2088–2099. [[CrossRef](#)]
263. Gong, X.; Liu, B.; Kang, B.; Xu, G.; Wang, Q.; Jia, C.; Zhang, J. Boosting Cu–Ce interaction in Cu<sub>x</sub>O/CeO<sub>2</sub> nanocube catalysts for enhanced catalytic performance of preferential oxidation of CO in H<sub>2</sub>-rich gases. *Mol. Catal.* **2017**, *436*, 90–99. [[CrossRef](#)]
264. Papavasiliou, J.; Vakros, J.; Avgouropoulos, G. Impact of acid treatment of CuO–CeO<sub>2</sub> catalysts on the preferential oxidation of CO reaction. *Catal. Commun.* **2018**, *115*, 68–72. [[CrossRef](#)]
265. Borchers, C.; Martin, M.L.; Vorobjeva, G.A.; Morozova, O.S.; Firsova, A.A.; Leonov, A.V.; Kurmaev, E.Z.; Kukhareenko, A.I.; Zhidkov, I.S.; Cholakh, S.O. Cu–CeO<sub>2</sub> nanocomposites: mechanochemical synthesis, physico-chemical properties, CO-PROX activity. *J. Nanopart. Res.* **2016**, *18*, 344. [[CrossRef](#)]
266. Martínez-Arias, A.; Gamarra, D.; Fernández-García, M.; Hornés, A.; Belver, C. Spectroscopic Study on the Nature of Active Entities in Copper-Ceria CO-PROX Catalysts. *Top. Catal.* **2009**, *52*, 1425–1432. [[CrossRef](#)]
267. Lu, J.; Wang, J.; Zou, Q.; He, D.; Zhang, L.; Xu, Z.; He, S.; Luo, Y. Unravelling the Nature of the Active Species as well as the Doping Effect over Cu/Ce-Based Catalyst for Carbon Monoxide Preferential Oxidation. *ACS Catal.* **2019**, *9*, 2177–2195. [[CrossRef](#)]
268. Monte, M.; Gamarra, D.; López Cámara, A.; Rasmussen, S.B.; Gyorffy, N.; Schay, Z.; Martínez-Arias, A.; Conesa, J.C. Preferential oxidation of CO in excess H<sub>2</sub> over CuO/CeO<sub>2</sub> catalysts: Performance as a function of the copper coverage and exposed face present in the CeO<sub>2</sub> support. *Catal. Today* **2014**, *229*, 104–113. [[CrossRef](#)]

269. Li, W.; Hu, Y.; Jiang, H.; Yang, S.; Li, C. Facile synthesis of multi-shelled hollow Cu–CeO<sub>2</sub> microspheres with promoted catalytic performance for preferential oxidation of CO. *Mater. Chem. Phys.* **2019**, *226*, 158–168. [[CrossRef](#)]
270. Firsova, A.A.; Morozova, O.S.; Vorob'eva, G.A.; Leonov, A.V.; Kukharenko, A.I.; Cholakh, S.O.; Kurmaev, E.Z.; Korchak, V.N. Mechanochemical Activation of Cu–CeO<sub>2</sub> Mixture as a Promising Technique for the Solid-State Synthesis of Catalysts for the Selective Oxidation of CO in the Presence of H<sub>2</sub>. *Kinet. Catal.* **2018**, *59*, 160–173. [[CrossRef](#)]
271. Yen, H.; Seo, Y.; Kaliaguine, S.; Kleitz, F. Tailored Mesostructured Copper/Ceria Catalysts with Enhanced Performance for Preferential Oxidation of CO at Low Temperature. *Angew. Chem. Int. Ed.* **2012**, *51*, 12032–12035. [[CrossRef](#)] [[PubMed](#)]
272. Liu, Z.; Chen, J.; Zhou, R.; Zheng, X. Influence of Ethanol Washing in Precursor on CuO–CeO<sub>2</sub> Catalysts in Preferential Oxidation of CO in Excess Hydrogen. *Catal. Lett.* **2008**, *123*, 102–106. [[CrossRef](#)]
273. Xia, Y.; Lao, J.; Ye, J.; Cheng, D.-G.; Chen, F.; Zhan, X. Role of Two-Electron Defects on the CeO<sub>2</sub> Surface in CO Preferential Oxidation over CuO/CeO<sub>2</sub> Catalysts. *ACS Sustain. Chem. Eng.* **2019**, *7*, 18421–18433. [[CrossRef](#)]
274. Xie, Y.; Yin, Y.; Zeng, S.; Gao, M.; Su, H. Coexistence of Cu<sup>+</sup> and Cu<sup>2+</sup> in star-shaped CeO<sub>2</sub>/Cu<sub>x</sub>O catalyst for preferential CO oxidation. *Catal. Commun.* **2017**, *99*, 110–114. [[CrossRef](#)]
275. Chen, S.; Li, L.; Hu, W.; Huang, X.; Li, Q.; Xu, Y.; Zuo, Y.; Li, G. Anchoring High-Concentration Oxygen Vacancies at Interfaces of CeO<sub>2-x</sub>/Cu toward Enhanced Activity for Preferential CO Oxidation. *ACS Appl. Mater. Interfaces* **2015**, *7*, 22999–23007. [[CrossRef](#)]
276. Zhang, L.; Chen, T.; Zeng, S.; Su, H. Effect of doping elements on oxygen vacancies and lattice oxygen in CeO<sub>2</sub>-CuO catalysts. *J. Environ. Chem. Eng.* **2016**, *4*, 2785–2794. [[CrossRef](#)]
277. López Cámara, C.A.; Cortés Corberán, V.; Barrio, L.; Zhou, G.; Si, R.; Hanson, J.C.; Monte, M.; Conesa, J.C.; Rodríguez, J.A.; Martínez-Arias, A. Improving the CO-PROX Performance of Inverse CeO<sub>2</sub>/CuO Catalysts: Doping of the CuO Component with Zn. *J. Phys. Chem. C* **2014**, *118*, 9030–9041. [[CrossRef](#)]
278. Papavasiliou, J.; Rawski, M.; Vakros, J.; Avgouropoulos, G. A Novel Post-Synthesis Modification of CuO–CeO<sub>2</sub> Catalysts: Effect on Their Activity for Selective CO Oxidation. *ChemCatChem* **2018**, *10*, 2096–2106. [[CrossRef](#)]
279. Liu, Z.; Zhou, R.; Zheng, X. Influence of residual K<sup>+</sup> on the catalytic performance of CuO–CeO<sub>2</sub> catalysts in preferential oxidation of CO in excess hydrogen. *Int. J. Hydrogen Energy* **2008**, *33*, 791–796. [[CrossRef](#)]
280. Dongil, A.B.; Bachiller-Baeza, B.; Castillejos, E.; Escalona, N.; Guerrero-Ruiz, A.; Rodríguez-Ramos, I. The promoter effect of potassium in CuO/CeO<sub>2</sub> systems supported on carbon nanotubes and graphene for the CO-PROX reaction. *Catal. Sci. Technol.* **2016**, *6*, 6118–6127. [[CrossRef](#)]
281. Ding, J.; Li, L.; Li, H.; Chen, S.; Fang, S.; Feng, T.; Li, G. Optimum Preferential Oxidation Performance of CeO<sub>2</sub>-CuO<sub>x</sub>-RGO Composites through Interfacial Regulation. *ACS Appl. Mater. Interfaces* **2018**, *10*, 7935–7945. [[CrossRef](#)] [[PubMed](#)]
282. Zhang, H.; Xu, C.; Ding, J.; Su, H.; Zeng, S. RGO/MWCNTs/Cu<sub>x</sub>O–CeO<sub>2</sub> ternary nanocomposites for preferential CO oxidation in hydrogen-rich streams. *Appl. Surf. Sci.* **2017**, *426*, 50–55. [[CrossRef](#)]
283. Xu, C.; Zeng, S.; Zhang, H.; Xie, Y.; Zhang, A.; Jing, G.; Su, H. Facile hydrothermal procedure to synthesize sheet-on-sheet reduced graphene oxide (RGO)/Cu<sub>x</sub>O–CeO<sub>2</sub> nanocomposites for preferential oxidation of carbon monoxide. *Int. J. Hydrogen Energy* **2017**, *42*, 14133–14143. [[CrossRef](#)]
284. Wang, Q.; Zhang, H.; Wu, J.; Tuya, N.; Zhao, Y.; Liu, S.; Dong, Y.; Li, P.; Xu, Y.; Zeng, S. Experimental and computational studies on copper-cerium catalysts supported on nitrogen-doped porous carbon for preferential oxidation of CO. *Catal. Sci. Technol.* **2019**, *9*, 3023–3035. [[CrossRef](#)]
285. Chen, A.; Yu, X.; Zhou, Y.; Miao, S.; Li, Y.; Kuld, S.; Sehested, J.; Liu, J.; Aoki, T.; Hong, S.; et al. Structure of the catalytically active copper–ceria interfacial perimeter. *Nat. Catal.* **2019**, *2*, 334–341. [[CrossRef](#)]
286. Ning, J.; Zhou, Y.; Chen, A.; Li, Y.; Miao, S.; Shen, W. Dispersion of copper on ceria for the low-temperature water-gas shift reaction. *Catal. Today* **2019**, in press. [[CrossRef](#)]
287. Si, R.; Raitano, J.; Yi, N.; Zhang, L.; Chan, S.-W.; Flytzani-Stephanopoulos, M. Structure sensitivity of the low-temperature water-gas shift reaction on Cu–CeO<sub>2</sub> catalysts. *Catal. Today* **2012**, *180*, 68–80. [[CrossRef](#)]
288. Yan, H.; Yang, C.; Shao, W.-P.; Cai, L.-H.; Wang, W.-W.; Jin, Z.; Jia, C.-J. Construction of stabilized bulk-nano interfaces for highly promoted inverse CeO<sub>2</sub>/Cu catalyst. *Nat. Commun.* **2019**, *10*, 3470. [[CrossRef](#)]
289. Wang, X.; Mi, J.; Lin, Z.; Lin, Y.; Jiang, L.; Cao, Y. Efficient fabrication of mesoporous active Cu–Co–CeO<sub>2</sub> catalysts for water-gas shift. *Mater. Lett.* **2016**, *162*, 214–217. [[CrossRef](#)]

290. Wang, X.; Liu, Y.; Peng, X.; Lin, B.; Cao, Y.; Jiang, L. Sacrificial Adsorbate Strategy Achieved Strong Metal-Support Interaction of Stable Cu Nanocatalysts. *ACS Appl. Energy Mater.* **2018**, *1*, 1408–1414. [[CrossRef](#)]
291. Djinović, P.; Batista, J.; Levec, J.; Pintar, A. Comparison of water-gas shift reaction activity and long-term stability of nanostructured CuO-CeO<sub>2</sub> catalysts prepared by hard template and co-precipitation methods. *Appl. Catal. A Gen.* **2009**, *364*, 156–165. [[CrossRef](#)]
292. Chen, C.; Zhan, Y.; Li, D.; Zhang, Y.; Lin, X.; Jiang, L.; Zheng, Q. Preparation of CuO/CeO<sub>2</sub> Catalyst with Enhanced Catalytic Performance for Water-Gas Shift Reaction in Hydrogen Production. *Energy Technol.* **2018**, *6*, 1096–1103. [[CrossRef](#)]
293. Zhang, Z.; Wang, S.-S.; Song, R.; Cao, T.; Luo, L.; Chen, X.; Gao, Y.; Lu, J.; Li, W.-X.; Huang, W. The most active Cu facet for low-temperature water gas shift reaction. *Nat. Commun.* **2017**, *8*, 488. [[CrossRef](#)] [[PubMed](#)]
294. Agarwal, S.; Zhu, X.; Hensen, E.J.M.; Mojet, B.L.; Lefferts, L. Surface-Dependence of Defect Chemistry of Nanostructured Ceria. *J. Phys. Chem. C* **2015**, *119*, 12423–12433. [[CrossRef](#)]
295. Wang, Y.-X.; Wang, G.-C. A Systematic Theoretical Study of Water Gas Shift Reaction on Cu(111) and Cu(110): Potassium Effect. *ACS Catal.* **2019**, *9*, 2261–2274. [[CrossRef](#)]
296. Chen, C.; Zhan, Y.; Zhou, J.; Li, D.; Zhang, Y.; Lin, X.; Jiang, L.; Zheng, Q. Cu/CeO<sub>2</sub> Catalyst for Water-Gas Shift Reaction: Effect of CeO<sub>2</sub> Pretreatment. *ChemPhysChem* **2018**, *19*, 1448–1455. [[CrossRef](#)]
297. Graciani, J.; Mudiyansele, K.; Xu, F.; Baber, A.E.; Evans, J.; Senanayake, S.D.; Stacchiola, D.J.; Liu, P.; Hrbek, J.; Fernández Sanz, J.; et al. Highly active copper-ceria and copper-ceria-titania catalysts for methanol synthesis from CO<sub>2</sub>. *Science* **2014**, *345*, 546–550. [[CrossRef](#)]
298. Rodriguez, J.A.; Liu, P.; Stacchiola, D.J.; Senanayake, S.D.; White, M.G.; Chen, J.G. Hydrogenation of CO<sub>2</sub> to Methanol: Importance of Metal-Oxide and Metal-Carbide Interfaces in the Activation of CO<sub>2</sub>. *ACS Catal.* **2015**, *5*, 6696–6706. [[CrossRef](#)]
299. Kattel, S.; Liu, P.; Chen, J.G. Tuning Selectivity of CO<sub>2</sub> Hydrogenation Reactions at the Metal/Oxide Interface. *J. Am. Chem. Soc.* **2017**, *139*, 9739–9754. [[CrossRef](#)]
300. Wang, W.; Qu, Z.; Song, L.; Fu, Q. CO<sub>2</sub> hydrogenation to methanol over Cu/CeO<sub>2</sub> and Cu/ZrO<sub>2</sub> catalysts: Tuning methanol selectivity via metal-support interaction. *J. Energy Chem.* **2020**, *40*, 22–30. [[CrossRef](#)]
301. Van de Water, L.G.A.; Wilkinson, S.K.; Smith, R.A.P.; Watson, M.J. Understanding methanol synthesis from CO/H<sub>2</sub> feeds over Cu/CeO<sub>2</sub> catalysts. *J. Catal.* **2018**, *364*, 57–68. [[CrossRef](#)]
302. Hu, X.; Zhao, C.; Guan, Q.; Hu, X.; Li, W.; Chen, J. Selective hydrogenation of CO<sub>2</sub> over a Ce promoted Cu-based catalyst confined by SBA-15. *Inorg. Chem. Front.* **2019**, *6*, 1799–1812. [[CrossRef](#)]
303. Li, S.; Guo, L.; Ishihara, T. Hydrogenation of CO<sub>2</sub> to methanol over Cu/AlCeO catalyst. *Catal. Today* **2020**, *339*, 352–361. [[CrossRef](#)]
304. Tan, Q.; Shi, Z.; Wu, D. CO<sub>2</sub> Hydrogenation to Methanol over a Highly Active Cu-Ni/CeO<sub>2</sub>-Nanotube Catalyst. *Ind. Eng. Chem. Res.* **2018**, *57*, 10148–10158. [[CrossRef](#)]
305. Tan, Q.; Shi, Z.; Wu, D. CO<sub>2</sub> hydrogenation over differently morphological CeO<sub>2</sub>-supported Cu-Ni catalysts. *Int. J. Energy Res.* **2019**, *43*, 5392–5404. [[CrossRef](#)]
306. Li, H.; Cui, Y.; Liu, Q.; Dai, W.-L. Insight into the Synergism between Copper Species and Surface Defects Influenced by Copper Content over Copper/Ceria Catalysts for the Hydrogenation of Carbonate. *ChemCatChem* **2018**, *10*, 619–624. [[CrossRef](#)]
307. Yang, S.-C.; Pang, S.H.; Sulmonetti, T.P.; Su, W.-N.; Lee, J.-F.; Hwang, B.-J.; Jones, C.W. Synergy between Ceria Oxygen Vacancies and Cu Nanoparticles Facilitates the Catalytic Conversion of CO<sub>2</sub> to CO under Mild Conditions. *ACS Catal.* **2018**, *8*, 12056–12066. [[CrossRef](#)]
308. Lin, L.; Yao, S.; Rui, N.; Han, L.; Zhang, F.; Gerlak, C.A.; Liu, Z.; Cen, J.; Song, L.; Senanayake, S.D.; et al. Conversion of CO<sub>2</sub> on a highly active and stable Cu/FeO<sub>x</sub>/CeO<sub>2</sub> catalyst: tuning catalytic performance by oxide-oxide interactions. *Catal. Sci. Technol.* **2019**, *9*, 3735–3742. [[CrossRef](#)]

